НАУКОВІ ВІСТІ КПІ

Міжнародний науково-технічний журнал

№ 4 (141) 2025

Започаткований у вересні 1997 року

У номері:

Адреса редакції:
КПІ ім. Ігоря Сікорського
просп. Берестейський, 37
Київ, 03056, Україна

Тел. (+38 044) 204-94-53
E-mail: n.visti@kpi.ua
https://scinews.kpi.ua

Засновник – Національний технічний університет України
"Київський політехнічний інститут імені Ігоря Сікорського"

Внесений до реєстру суб'єктів у сфері медіа з присвоєнням ідентифікатора медіа R30-02405
(рішення Національної ради з питань телебачення і радіомовлення № 1794 від 21.12.2023)

Згідно з наказами МОН України № 1643 від 28.12.2019, № 409 від 17.03.2020 та № 392 від 05.04.2023 журнал включено до категорії «Б» Переліку наукових фахових видань України з технічних наук (спеціальності – F1 Прикладна математика, F2 Інженерія програмного забезпечення, F3 Комп'ютерні науки, F7 Комп'ютерна інженерія, F4 Системний аналіз та наука про дані, G9 Прикладна механіка, G8 Матеріалознавство, G11 машинобудування (за спеціалізаціями), G12 Авіаційна та ракетно-космічна техніка, G3 Електрична інженерія, G4 Енерговиробництво (за спеціалізацією), G1 Хімічні технології та інженерія, G5 Електроніка, електронні комунікації, приладобудування та радіотехніка, G7 Автоматизація, комп'ютерно-інтегровані технології та робототехніка)

Рекомендовано Вченою радою Національного технічного університету України
"Київський політехнічний інститут імені Ігоря Сікорського", протокол № 12 від 15.12.2025 р.

Національний технічний університет України
"Київський політехнічний інститут імені Ігоря Сікорського"
Свідоцтво про державну реєстрацію: серія ДК № 5354 від 25.05.2017 р., просп. Берестейський, 37, Київ, 03056

Підп. до друку 22.12.2025. Формат 60×84$^{1}/_{8}$. Папір офс. Гарнітура UkrainianTimesET.
Спосіб друку – електрографічний. Ум. друк. арк. 7,35. Обл.-вид. арк. 5,75. Наклад 30 пр.

Видавництво "Політехніка" КПІ ім. Ігоря Сікорського
вул. Політехнічна, 14, корп. 15, Київ, 03056
тел. (044) 204-81-78

KPI SCIENCE NEWS

International research journal

No 4 (141) 2025

Founded in September, 1997

In the issue:

Editorial office:
Igor Sikorsky Kyiv Polytechnic Institute,
ave. Beresteyskyi, 37,
Kyiv, 03056, Ukraine

E-mail: n.visti@kpi.ua
https://scinews.kpi.ua

Founder – National Technical University of Ukraine "Igor Sikorsky Kyiv Polytechnic Institute"

Entered into the register of subjects in the field of media with the assignment of media identifier R30-02405 (decision of the National Council on Television and Radio Broadcasting of Ukraine No. 1794 dated 21.12.2023).

According to the orders of MES of Ukraine from 12.28.2019 no. 1643, from 03.17.2020 no. 409, and from 04.05.2023 no. 392 the journal is included in the «B» category of the List of scientific publications of Ukraine on technical sciences (specialities – F1 Applied Mathematics, F2 Software Engineering, F3 Computer Science, F7 Computer Engineering, F4 System Analysis and Data Science, G9 Applied Mechanics, G8 Materials Science, G11 Machinery Engineering (by specializations), G12 Aviation and Aerospace Technologies, G3 Electric Engineering, G4 Energy Production (by specialization), G1 Chemical Technologies and Engineering, G5 Electronics, Electronic Communications, Instrument Making and Radio Engineering, G7 Automation, Computer-Integrated Technologies and Robotics)

Advised by the Academic Council of the National Technical University of Ukraine "Igor Sikorsky Kyiv Polytechnic Institute", protocol No 12 on 15.12.2025.

National Technical University of Ukraine "Igor Sikorsky Kyiv Polytechnic Institute"
Registration Certificate – ДК № 5354 on 25.05.2017, Ave. Beresteiskyi, 37, Kyiv, 03056

Signed for printing on 22.12.2025. Format 60×84 1/8. Text-weight paper. Font UkrainianTimesET. Print. tech. – electrographic. Convent. printed sheets 7,35. Published sheets 5,75. Edition of 30 copies.

Publishing House "Politehnika", Igor Sikorsky Kyiv Polytechnic Institute
Politekhnichna Str., 14, building 15, Kyiv, 03056
Tel.: (044) 204-81-78

ЗМІСТ

Прикладна математика

Системний аналіз та наука про дані

CONTENTS

Applied Mathematics

System Analysis and Data Science

ПРИКЛАДНА МАТЕМАТИКА

DOI: https://doi.org/10.20535/kpisn.2025.4.343114
UDC 519.832.3

Vadim V. Romanuke*
Vinnytsia Institute of Trade and Economics of State University of Trade and Economics, Vinnytsia, Ukraine
*Corresponding author: romanukevadimv@gmail.com

LINEAR-ACCURACY ONE-BULLET SILENT DUEL WITH PROGRESSING-BY-ONE-THIRD SHOOTING MOMENTS

Background. A finite zero-sum game is considered, which models competitive interaction between two subjects. The subject, referred to as the duelist, must take an action (or, metaphorically, shoot the single bullet) during a standardized time span, where the bullet can be shot at only specified time moments. The duelist benefits from shooting as late as possible, but only when the duelist shoots first.

Objective. The objective is to determine optimal behavior of the duelists for a pattern of the duel discrete progression, by which the tension builds up as the duel end approaches and there are more possibilities to shoot.

Methods. Both the duelists act within the same conditions, and so the one-bullet silent duel is symmetric. Therefore, its optimal value is 0 and the duelists have the same optimal strategies. The shooting accuracy is linear being determined by an accuracy proportionality factor.

Results. Depending on the factor, all pure strategy solutions are found for such duels, whose possible-shooting moments comprise a progression pattern. According to this pattern, every next possible-shooting moment is obtained by adding the third of the remaining span to the current moment. The solutions for this pattern are compared to the known solutions for the geometrical-progression pattern and the pattern whose possible-shooting moments progress in a smoother manner.

Conclusions. The proved assertions contribute another specificity of the progressing-by-one-third shooting moments in linear-accuracy one-bullet silent duels to the games of timing. Compared to duels for other duel discrete progression patterns, the specificity consists in that the duel with progressing-by-one-third shooting moments has a constant interval of lower (weaker) shooting accuracies, at which the duelist possesses an optimal pure strategy. This interval is $\left[\frac{4}{5};\frac{6}{5}\right]$ that symmetrically breaks the low-accuracy interval (0; 2).

Keywords: one-bullet silent duel; linear accuracy; matrix game; pure strategy solution; progressing-by-one-third shooting moments.

1. Introduction

A one-bullet silent duel is a timing zero-sum game, in which it is unknown to the player (also referred to as the duelist) whether and when the other duelist has fired its bullet until the end of the duel time span [1, 2]. The span is usually interval [0; 2]. The bullet is a metaphor for an option to make a decision or take an action [3, 4]. In fact, shooting (or firing) a bullet means making a decision or taking an action during interaction between the two duelists (decision-makers, consumers, entrepreneurs, users, etc.) [5, 6]. The duelist may not fire the bullet until the very last (final) moment to shoot, but then it is nonetheless fired at the final moment, because the action must be taken anyway [2, 7, 8]. The duelist is also featured with an accuracy function which is a nondecreasing function of time [1, 9, 10].

To more realistically simulate interaction between the two duelists, discrete silent duels are

Пропозиція для цитування цієї статті: В.В. Романюк, "Безшумна дуель з однією кулею лінійної влучності та прогресуючими на одну третину моментами пострілу", *Наукові вісті КПІ*, № 4, с. 7–19, 2025. doi: 10.20535/kpisn.2025.4.343114

Offer a citation for this article: V.Vadim Romanuke, "Linear-accuracy one-bullet silent duel with progressing-by-one-third shooting moments", *KPI Science News*, No. 4, pp. 7–19, 2025. doi: 10.20535/kpisn.2025.4.343114

considered, in which the duelist can shoot only at specified time moments [1, 3, 4, 11, 12]. The number of such possible shooting moments is finite. The moments of the duel beginning and duel end are included in this number [7, 13, 14]. So, in a discrete duel with possible shooting moments the players' pure strategy sets are

$$X_N = \{x_i\}_{i=1}^{N} = Y_N = \{y_j\}_{j=1}^{N} = T_N = \{t_q\}_{q=1}^{N} \subset [0;1] \quad (1)$$

by

$$t_q < t_{q+1} \quad \forall\, q = \overline{1, N-1} \text{ and } t_1 = 0,\ t_N = 1$$

for $N \in \mathbb{N} \setminus \{1\}$.

It is presumed that both the duelists act within the same conditions, and so the one-bullet silent duel is symmetric. Therefore, its optimal value is 0 and the duelists have the same optimal strategies, although they still can be non-symmetric [3, 11, 13, 15]. The duelist benefits from shooting as late as possible, but only when the duelist shoots first [2, 16, 17]. This is modeled, in particular, by a skew-symmetric payoff matrix [1, 7, 18]

$$\mathbf{K}_N = \left[k_{ij}\right]_{N\times N} = \left[-k_{ji}\right]_{N\times N} = -\mathbf{K}_N^{\mathrm{T}} \quad (2)$$

whose entries

$$k_{ij} = ax_i - ay_j + a^2 x_i y_j \operatorname{sign}\left(y_j - x_i\right) \quad (3)$$

for

$$i = \overline{1, N} \text{ and } j = \overline{1, N} \text{ by } a > 0.$$

The accuracy proportionality factor a defines the duelists' linear accuracy functions [7, 16, 19]

$$p_X(x) = ax, \quad p_Y(y) = ay, \quad (4)$$

through which entry k_{ij} can be generally given as

$$k_{ij} = p_X(x_i) - p_Y\left(y_j\right) + \\ + p_X(x_i)\, p_Y\left(y_j\right) \operatorname{sign}\left(y_j - x_i\right). \quad (5)$$

Hence, the global objective is to find pure strategy solutions of linear-accuracy one-bullet silent duel (LA1BSD)

$$\left\langle X_N, Y_N, \mathbf{K}_N \right\rangle = \left\langle \{x_i\}_{i=1}^{N}, \{y_j\}_{j=1}^{N}, \mathbf{K}_N \right\rangle \quad (6)$$

by (1)–(3).

LA1BSD (6) is called progressive if the density of the duelist's pure strategies between $t_1 = 0$ and $t_N = 1$ progressively grows (in accordance with a definite pattern) as the duelist approaches to the duel end $t_N = 1$ [1, 7, 9, 10, 12, 13]. The duel's shooting-moment progression is quite natural because the tension builds up as the duel end approaches, and thus the duelist must have more possibilities to shoot [6, 11, 20, 21]. A particular interest of applying LA1BSDs exists in advertising, where competitiveness and waiting to attract and harvest more audience data are modeled [22, 23].

2. Known results

The first particular case of the progressive LA1BSD was considered in [15], where

$$t_q = \sum_{l=1}^{q-1} 2^{-l} = \frac{2^{q-1} - 1}{2^{q-1}} \quad (7)$$

for $q = \overline{2, N-1}$ and pure strategy solutions had been obtained for any $a \geq 1$, and specific conditions had been found for $a \in (0;1)$ such, at which the duel has a pure strategy solution. Thus, situation

$$\{x_2, y_2\} = \left\{\frac{1}{2}, \frac{1}{2}\right\} \quad (8)$$

is single optimal in duel (6) by (1)–(3), (7), and $a > 1$ for $N \in \mathbb{N} \setminus \{1, 2\}$. Situation (8) is non-optimal by $a \in (0;1)$ However, situation (8) remains single optimal by $a = 1$ for $N \in \mathbb{N} \setminus \{1, 2, 3\}$. The duel by $a = 1$ for $N = 3$ has four optimal situations (8),

$$\{x_3, y_3\} = \{1, 1\}, \quad (9)$$

$$\{x_3, y_2\} = \left\{1, \frac{1}{2}\right\}, \quad (10)$$

$$\{x_2, y_3\} = \left\{\frac{1}{2}, 1\right\}. \quad (11)$$

Situation

$$\{x_2, y_2\} = \{1, 1\} \quad (12)$$

is single optimal by any $a > 0$ in the most trivial case, when $N = 2$ (and thus the duelist can shoot only either at the duel beginning or duel end, which annuls the progressiveness). Situation (9) is the single solution to 3×3 duels by $a \in (0;1)$. For the general case of $N = 2$ article [15] proves that only one $n \in \{\overline{3, N-1}\}$ exists such that situation

$$\{x_n, y_n\} = \left\{\frac{2^{n-1} - 1}{2^{n-1}}, \frac{2^{n-1} - 1}{2^{n-1}}\right\} \quad (13)$$

is optimal by

$$a \in \left[\frac{1}{2^{n-1} - 1}; \frac{2^{n-2}}{\left(2^{n-1} - 1\right) \cdot \left(2^{n-2} - 1\right)}\right] \subset (0;1) \quad (14)$$

and situation

$$\{x_N, y_N\} = \{1, 1\} \tag{15}$$

is optimal by

$$a \in \left(0; \frac{1}{2^{N-2}-1}\right] \subset (0; 1) \tag{16}$$

for $N \in \mathbb{N} \setminus \{1, 2, 3\}$. If

$$a = \frac{1}{2^{N-2}-1} \tag{17}$$

then situations (15),

$$\{x_{N-1}, y_{N-1}\} = \left\{\frac{2^{N-2}-1}{2^{N-2}}, \frac{2^{N-2}-1}{2^{N-2}}\right\}, \tag{18}$$

$$\{x_{N-1}, y_N\} = \left\{\frac{2^{N-2}-1}{2^{N-2}}, 1\right\}, \tag{19}$$

$$\{x_N, y_{N-1}\} = \left\{1, \frac{2^{N-2}-1}{2^{N-2}}\right\} \tag{20}$$

are optimal; apart from situations (15), (18)–(20), there are no other pure strategy solutions in the duel by (17). If

$$a \in \left(0; \frac{1}{2^{N-2}-1}\right) \tag{21}$$

then optimal situation (15) is the single one. If

$$a \neq \frac{1}{2^{N-2}-1} \tag{22}$$

and (14) holds, optimal situation (13) is the single one. Finally, if neither (14) nor (16) holds, then the duel does not have a pure strategy solution.

The second particular case of the progressive LA1BSD was considered in [13], where

$$t_q = \sum_{n=1}^{q-1} \frac{1}{n(n+1)} = \frac{q-1}{q} \tag{23}$$

for $q = \overline{2, N-1}$.

This case was motivated by that the density of the duelist's pure strategies between $t_1 = 0$ and $t_N = 1$ grows too quickly if the geometrical progression by (7) is used. Progression (23) is smoother providing a sort of compactification of shooting moments. Meanwhile, article [13] proves that the solutions in the progressive LA1BSD (6) by (1)–(3), (23) for $N = 3$ are the same as the solutions in the progressive LA1BSD (6) by (1)–(3), (7) for $N = 3$. Besides, the progressive LA1BSD (6) by (1)–(3), (23) for $N \in \mathbb{N} \setminus \{1, 2, 3\}$ and a ≥ 1 has the single optimal situation (8), which coincides with the solution in the case of (7). Another coincidence is that in the case of (23) situation (8) is non-optimal by $a \in (0; 1)$ for $N \in \mathbb{N} \setminus \{1, 2\}$. The remaining results for (23) were proved [13] for $a \in (0; 1)$ and $N \in \mathbb{N} \setminus \{1, 2, 3\}$. Situation

$$\{x_3, y_3\} = \left\{\frac{2}{3}, \frac{2}{3}\right\} \tag{24}$$

is optimal only if $a = \frac{1}{2}$. Except for the third and last shooting moments $t_3 = \frac{2}{3}$ and $t_N = 1$, there are no other optimal pure strategies. The 4×4 duel with has four optimal pure strategy situations: situation (24) and situations

$$\{x_4, y_4\} = \{1, 1\}, \tag{25}$$

$$\{x_3, y_4\} = \left\{\frac{2}{3}, 1\right\}, \tag{26}$$

$$\{x_4, y_3\} = \left\{1, \frac{2}{3}\right\}. \tag{27}$$

Finally, situation (15) is single optimal for $N \in \mathbb{N} \setminus \{1, 2, 3, 4\}$ and

$$a \leqslant \frac{1}{N-2}. \tag{28}$$

In the 4×4 duel with

$$a < \frac{1}{N-2} = \frac{1}{2} \tag{29}$$

situation (15) is single optimal as well.

Despite progression (23) is smoother than progression (7), it still lacks a reasonable last-to-penultimate ratio

$$\frac{t_N}{t_{N-1}} = \frac{1}{t_{N-1}}, \tag{30}$$

which is

$$\frac{1}{t_{N-1}} = \frac{N-1}{N-2} \tag{31}$$

for (23), whereas ratio (30) is

$$\frac{1}{t_{N-1}} = \frac{2^{N-2}}{2^{N-2}-1} \tag{32}$$

for (7). Indeed,

$$\frac{N-1}{N-2} - \frac{2^{N-2}}{2^{N-2}-1} = \frac{N-2+1}{N-2} - \frac{2^{N-2}-1+1}{2^{N-2}-1} =$$

$$= 1 + \frac{1}{N-2} - 1 - \frac{1}{2^{N-2}-1} = \frac{1}{N-2} - \frac{1}{2^{N-2}-1} =$$
$$= \frac{2^{N-2}-1-N+2}{(N-2)\left(2^{N-2}-1\right)} = \frac{2^{N-2}-N+1}{(N-2)\left(2^{N-2}-1\right)} > 0 \quad (33)$$

for $N \in \mathbb{N} \setminus \{1, 2, 3\}$, where difference (33) between last-to-penultimate ratios (31) and (32) is 0 only at $N = 3$. So, in a duel with (23) the duelist gets a huge gap between the penultimate and last moment of possible shooting. Hence, another pattern of possible-shooting-moment progression is to be considered. According to this pattern, every next possible-shooting moment is obtained by adding the third of the remaining span to the current moment:

$$t_q = t_{q-1} + \frac{1 - t_{q-1}}{3} \quad (34)$$

for $q = \overline{2, N-1}$.

Herein, the local objective is to find pure strategy solutions of progressive LA1BSD (6) by (1)–(3), (34) for $N \in \mathbb{N} \setminus \{1, 2\}$.

3. Trivia and convention

Clearly, the most trivial duel size is 3×3. Its possible-shooting-moment progression is trivially a triple

$$T_3 = \{t_1, t_2, t_3\} = \left\{0, \frac{1}{3}, 1\right\}. \quad (35)$$

It is worth noting that the middle of the 3×3 duel time span is as twice as closer to the duel beginning than to the duel end.

Inasmuch as a pure strategy solution of duel (6) corresponds to a saddle point of skew-symmetric matrix (2) with entries (3), only a zero entry of this matrix can be a saddle point [7]. Therefore, a row containing a negative entry does not contain saddle points; neither does the respective column containing the positive entry. Hence, it is conventionally possible to conclude only on saddle points in definite rows of matrix (2), which imply the same conclusions on saddle points in respective columns.

It is rather trivial, but inasmuch as

$$k_{1j} = -ay_j < 0 \quad \forall\, j = \overline{2, N}$$

then the first row of matrix (2) with entries (3) is not an optimal strategy of the first duelist, and thus situation

$$\{x_1, y_1\} = \{0, 0\}$$

is never optimal in the duel. Another trivial remark is that a nonnegative row of matrix (2) with entries (3) contains a saddle point on the main diagonal of the matrix [7]. If a row contains only positive entries, except for the main diagonal entry, all the other $N - 1$ rows of the respective column contain negative entries, and thus this row contains a single saddle point which is the single one in the duel.

To study the duel in an easier way, pattern (34) of possible-shooting-moment progression ought to be represented similarly to (7) and (23), having the right-hand side term that depends only on q.

Theorem 1. Sequence (34) for (1) can be represented as

$$t_q = t_{q-1} + \frac{1 - t_{q-1}}{3} =$$
$$= \sum_{l=1}^{q-1} \frac{2^{l-1}}{3^l} = \frac{3^{q-1} - 2^{q-1}}{3^{q-1}} \quad (36)$$

for $q = \overline{2, N-1}$.

Proof. First, re-write (34) as

$$t_q = \frac{1 + 2t_{q-1}}{3} \quad (37)$$

for $q = \overline{2, N-1}$.

Equality (36), considered without its last term, can be proved by induction. In the base case, $q = 2$ and

$$t_2 = \sum_{l=1}^{1} \frac{2^{l-1}}{3^l} = \frac{1}{3}, \quad (38)$$

which is true by (35). By the inductive hypothesis it is assumed that equality (36), considered without its last term, holds for any $q = k$:

$$t_k = \sum_{l=1}^{k-1} \frac{2^{l-1}}{3^l}. \quad (39)$$

By the inductive step, it is about to show that equality (36), considered without its last term, holds for $q = k + 1$:

$$t_{k+1} = \sum_{l=1}^{k} \frac{2^{l-1}}{3^l}. \quad (40)$$

Moment t_{k+1} can be given by using (37):

$$t_{k+1} = \frac{1 + 2t_k}{3} = \frac{1}{3} + \frac{2}{3} \cdot \sum_{l=1}^{k-1} \frac{2^{l-1}}{3^l} =$$

$$= \frac{1}{3} + \sum_{l=1}^{k-1} \frac{2^l}{3^{l+1}} = \frac{2^0}{3^1} + \sum_{l=1}^{k-1} \frac{2^l}{3^{l+1}} = \sum_{j=1}^{k} \frac{2^{j-1}}{3^j}. \quad (41)$$

The last term in (41) coincides with the right-hand side term in (40). This proves equality

$$t_q = \sum_{l=1}^{q-1} \frac{2^{l-1}}{3^l} \quad (42)$$

for $q = \overline{2, N-1}$ by induction with (38) and (39), for the middle term in (36).

Equality

$$\sum_{l=1}^{q-1} \frac{2^{l-1}}{3^l} = \frac{3^{q-1} - 2^{q-1}}{3^{q-1}} \quad (43)$$

for $q = \overline{2, N-1}$ is proved in the same way. In the base case, $q = 2$ and

$$\sum_{l=1}^{1} \frac{2^{l-1}}{3^l} = \frac{1}{3} = \frac{3-2}{3} = \frac{3^{2-1} - 2^{2-1}}{3^{2-1}}, \quad (44)$$

which is true by (38). By the inductive hypothesis it is assumed that equality (43) holds for any $q = k$:

$$\sum_{l=1}^{k-1} \frac{2^{l-1}}{3^l} = \frac{3^{k-1} - 2^{k-1}}{3^{k-1}}. \quad (45)$$

By the inductive step, it is about to show that equality (43) holds for $q = k + 1$:

$$\sum_{l=1}^{k} \frac{2^{l-1}}{3^l} = \frac{3^k - 2^k}{3^k}. \quad (46)$$

The sum in the left-hand side of (46) can be represented as the sum of the right-hand side term in (45) and the k-th summand in the left-hand side of (46):

$$\sum_{l=1}^{k} \frac{2^{l-1}}{3^l} = \sum_{l=1}^{k-1} \frac{2^{l-1}}{3^l} + \frac{2^{k-1}}{3^k} =$$

$$= \frac{3^{k-1} - 2^{k-1}}{3^{k-1}} + \frac{2^{k-1}}{3^k} = \frac{3^k - 3 \cdot 2^{k-1}}{3^k} +$$

$$+ \frac{2^{k-1}}{3^k} = \frac{3^k - 2 \cdot 2^{k-1}}{3^k} = \frac{3^k - 2^k}{3^k}. \quad (47)$$

The last term in (47) coincides with the right-hand side term in (46). This proves equality (43) by induction with (44) and (45). □

4. Three moments to shoot

Is the duel solution the same as for those two patterns of possible-shooting-moment progression, when the duelist has the fewest number of moments to shoot? The answer follows.

Theorem 2. Progressive LA1BSD (6) by (1)-(3), (36) for three moments to shoot ($N = 3$)

$$\langle X_3, Y_3, \mathbf{K}_3 \rangle = \left\langle \left\{0, \frac{1}{3}, 1\right\}, \left\{0, \frac{1}{3}, 1\right\}, \mathbf{K}_3 \right\rangle \quad (48)$$

has a single optimal situation (9) by $a \in (0; 2)$, a single optimal situation

$$\{x_2, y_2\} = \left\{\frac{1}{3}, \frac{1}{3}\right\} \quad (49)$$

by $a > 2$. At $a = 2$ this 4×4 duel has four optimal situations (49),

$$\{x_2, y_3\} = \left\{\frac{1}{3}, 1\right\}, \quad (50)$$

$$\{x_3, y_2\} = \left\{1, \frac{1}{3}\right\}, \quad (51)$$

and (9).

Proof. Upon plugging elements of (35) into (3) for $N = 3$, the respective payoff matrix is

$$\mathbf{K}_3 = \left[k_{ij}\right]_{3\times3} = \begin{bmatrix} 0 & -\frac{a}{3} & -a \\ \frac{a}{3} & 0 & \frac{a}{3}(a-2) \\ a & -\frac{a}{3}(a-2) & 0 \end{bmatrix}. \quad (52)$$

If $a \in (0; 2)$, matrix (52) has a single saddle point (9) due to the last row is positive except for main diagonal entry $k_{33} = 0$. If $a = 2$, the second and third rows are nonnegative, where

$$k_{22} = k_{23} = k_{32} = k_{33} = 0,$$

and matrix (52) has four saddle points: (49)–(51) and (9). If $a > 2$, matrix (52) has a single saddle point (49) due to the second row is positive except for main diagonal entry $k_{22} = 0$. □

Theorem 2 reads the difference between pattern (36) and patterns (7), (23), which lies in different second possible-shooting moments: it is $t_2 = \frac{1}{2}$ being the middle of the duel time span for patterns (7), (23), whereas it is $t_2 = \frac{1}{3}$ being the first third of the duel time

span for pattern (36). Subsequently, duel solutions for pattern (36) differ from those for patterns (7), (23) in the boundary value of accuracy proportionality factor a, at which the solution changes. It is $a = 2$ for pattern (36), whereas it is $a = 1$ for patterns (7), (23). Structurally, however, all the three patterns have similar solutions for progressive 3×3 LA1BSDs: the last possible-shooting moment is the single optimal strategy for the accuracy proportionality factor below the boundary value; the second and last possible-shooting moments are only optimal strategies at the boundary value; the second possible-shooting moment is the single optimal strategy for the accuracy proportionality factor above the boundary value.

5. Second possible-shooting moment optimality

It is natural to conjecture that the boundary value of accuracy proportionality factor $a = 2$ must separate two cases of the duel solution just like value $a = 1$ separates those for patterns (7), (23). So, right below, 4×4 and bigger duels are considered by $a \geq 1$.

Theorem 3. Progressive LA1BSD (6) by (1)-(3), (36) for $N \in \mathbb{N} \setminus \{1, 2, 3\}$ and $a \geq 2$ has the single optimal situation (49)

Proof. Consider the second row of matrix (2), where

$$k_{21} = \frac{a}{3} > 0 \tag{53}$$

and

$$k_{2j} = \frac{a}{3} - ay_j + \frac{a^2}{3} y_j = \frac{a}{3} \cdot \left(1 - 3y_j + ay_j\right). \tag{54}$$

If $a = 2$ then

$$1 - 3y_j + ay_j = 1 - y_j \geqslant 0$$

and (54) is nonnegative:

$$k_{2j} = \frac{a}{3} \cdot \left(1 - 3y_j + ay_j\right) = \frac{2}{3} \cdot \left(1 - y_j\right) \geqslant 0 \quad \forall\ j = \overline{3, N}, \tag{55}$$

where $k_{2N} = 0$ is the second zero entry after k_{22} in the second row. Due to (53) and (55), situation (49) is a saddle point. However,

$$k_{N,N-1} = 2 \cdot 1 - 2 \cdot \frac{3^{N-2} - 2^{N-2}}{3^{N-2}} - 4 \cdot \frac{3^{N-2} - 2^{N-2}}{3^{N-2}} = 2 - 6 \cdot \frac{3^{N-2} - 2^{N-2}}{3^{N-2}} = 2 - 6 + 6 \cdot \frac{2^{N-2}}{3^{N-2}} = -4 + 6 \cdot \frac{2^{N-2}}{3^{N-2}} = 2 \cdot \left(3 \cdot \frac{2^{N-2}}{3^{N-2}} - 2\right) < 0 \tag{56}$$

due to

$$\frac{2^{N-3}}{3^{N-3}} < 1 \text{ and } 3 \cdot \frac{2^{N-2}}{3^{N-2}} < 2 \text{ for } N \in \mathbb{N} \setminus \{1, 2, 3\}.$$

Inequality (56) implies that the last row and last column of matrix (2) do not contain saddle points. So, situation (49) is single optimal by $a = 2$.

If $a > 2$ then it is sufficient to prove that

$$1 - 3y_j + ay_j > 0 \quad \forall\ j = \overline{3, N}. \tag{57}$$

Inequality (57), implying that the second row is positive except for main diagonal entry $k_{22} = 0$, is equivalent to inequality

$$a > \frac{3y_j - 1}{y_j} = 3 - \frac{1}{y_j} \quad \forall\ j = \overline{3, N} \tag{58}$$

by

$$\frac{1}{3} < y_j \leqslant 1 \quad \forall\ j = \overline{3, N}. \tag{59}$$

As (59) is true, then

$$3 > \frac{1}{y_j} \geqslant 1,$$

$$-3 < -\frac{1}{y_j} \leqslant -1,$$

$$0 < 3 - \frac{1}{y_j} \leqslant 2 < a, \tag{60}$$

whence inequality (60) directly implies that inequality (58) holds and situation (49) is single optimal by $a > 2$.

6. Second possible-shooting moment non-optimality

It was proved in [13, 15] that the second possible-shooting moment is not an optimal strategy by $0 < a < 1$ in progressive LA1BSDs (6) by (1)–(3) and $N \in \mathbb{N} \setminus \{1, 2\}$ for patterns (7) and (23). In those duels, noticeably, the second possible-shooting moment is the middle of the duel time span, unlike for pattern (36). See whether the similar property keeps for the LA1BSD with progressing-by-one-third shooting moments by (36), only by $0 < a < 2$ and the second possible-shooting moment being the first third of the duel time span.

Theorem 4. Situation (49) is never optimal in progressive LA1BSD (6) by (1)-(3), (36) for $N \in \mathbb{N} \setminus \{1, 2\}$ **and** $0 < a < 2$**.**

Proof. For $N \in \mathbb{N} \setminus \{1, 2\}$ consider the second row of matrix (2) whose last column entry

$$k_{2N} = \frac{a}{3} - a + \frac{a^2}{3} = \frac{a}{3} \cdot (a - 2) < 0 \qquad (61)$$

by $0 < a < 2$.

Inequality (61) directly implies that the second row of matrix (2) does not contain saddle points by $0 < a < 2$. □

7. Third possible-shooting moment optimality

In a 3×3 duel by $0 < a < 2$ it is optimal to shoot at the very last (third) possible-shooting moment (*Theorem 2*). The last possible-shooting moment is optimal for duelists in LA1BSDs for patterns (7) and (23) as well, but just by $a \in (0; 1)$. See whether the third possible-shooting moment in bigger LA1BSDs can be an optimal strategy for pattern (36).

Theorem 5. Progressive LA1BSD (6) by (1)-(3), (36) for $N \in \mathbb{N} \setminus \{1, 2, 3\}$ **has an optimal pure strategy situation**

$$\{x_3, y_3\} = \left\{\frac{5}{9}, \frac{5}{9}\right\} \qquad (62)$$

by

$$a \in \left[\frac{4}{5}; \frac{6}{5}\right] . \qquad (63)$$

Proof. Due to *Theorem 4*, situation (49) is not optimal, so the first two rows of matrix (2) do not contain saddle points. If situation

$$\{x_n, y_n\} = \left\{\frac{3^{n-1} - 2^{n-1}}{3^{n-1}}, \frac{3^{n-1} - 2^{n-1}}{3^{n-1}}\right\} \qquad (64)$$

by $n \in \{\overline{3, N-1}\}$ is optimal, then, in the *n*-th row of matrix (2), inequalities

$$k_{nj} = ax_n - ay_j - a^2 x_n y_j \geqslant 0 \quad \forall\ y_j < x_n \quad (\forall\ j = \overline{1, n-1}) \qquad (65)$$

and

$$k_{nj} = ax_n - ay_j + a^2 x_n y_j \geqslant 0 \quad \forall\ y_j > x_n \quad (\forall\ j = \overline{n+1, N}) \qquad (66)$$

must hold. From inequality (65) it follows that

$$\frac{x_n}{1 + ax_n} \geqslant y_j \quad \forall\ y_j < x_n \quad (\forall\ j = \overline{1, n-1}) \qquad (67)$$

As

$$y_j \leqslant \frac{3^{n-2} - 2^{n-2}}{3^{n-2}} < \frac{3^{n-1} - 2^{n-1}}{3^{n-1}} = x_n \quad \forall\ j = \overline{1, n-1} \qquad (68)$$

then inequality (67) is transformed into

$$\frac{3^{n-1} - 2^{n-1}}{3^{n-1}} \cdot \frac{1}{1 + a \cdot \dfrac{3^{n-1} - 2^{n-1}}{3^{n-1}}} \geqslant \frac{3^{n-2} - 2^{n-2}}{3^{n-2}},$$

$$\frac{3^{n-1} - 2^{n-1}}{3^{n-1} + a \cdot \left(3^{n-1} - 2^{n-1}\right)} \geqslant \frac{3^{n-2} - 2^{n-2}}{3^{n-2}},$$

$$3^{n-1} \cdot 3^{n-2} - 2^{n-1} \cdot 3^{n-2} \geqslant 3^{n-1} \cdot 3^{n-2} - 3^{n-1} \cdot 2^{n-2} + a \cdot \left(3^{n-1} - 2^{n-1}\right)\left(3^{n-2} - 2^{n-2}\right),$$

$$3^{n-1} \cdot 2^{n-2} - 2^{n-1} \cdot 3^{n-2} \geqslant a \cdot \left(3^{n-1} - 2^{n-1}\right)\left(3^{n-2} - 2^{n-2}\right),$$

$$3^{n-2} \cdot 2^{n-2} \cdot (3 - 2) \geqslant a \cdot \left(3^{n-1} - 2^{n-1}\right)\left(3^{n-2} - 2^{n-2}\right),$$

$$3^{n-2} \cdot 2^{n-2} \geqslant a \cdot \left(3^{n-1} - 2^{n-1}\right)\left(3^{n-2} - 2^{n-2}\right),$$

whence

$$a \leqslant \frac{3^{n-2} \cdot 2^{n-2}}{\left(3^{n-1} - 2^{n-1}\right)\left(3^{n-2} - 2^{n-2}\right)} . \qquad (69)$$

From inequality (66) it follows that

$$\frac{x_n}{1 - ax_n} \geqslant y_j \quad \forall\ y_j > x_n \quad (\forall\ j = \overline{n+1, N}) . \qquad (70)$$

As

$$1 \geqslant y_j > \frac{3^{n-1} - 2^{n-1}}{3^{n-1}} = x_n \quad \forall\ j = \overline{n+1, N} . \qquad (71)$$

then inequality (70) is transformed into

$$\frac{3^{n-1} - 2^{n-1}}{3^{n-1}} \cdot \frac{1}{1 - a \cdot \dfrac{3^{n-1} - 2^{n-1}}{3^{n-1}}} \geqslant 1,$$

$$\frac{3^{n-1} - 2^{n-1}}{3^{n-1} - a \cdot \left(3^{n-1} - 2^{n-1}\right)} \geqslant 1 . \qquad (72)$$

If

$$3^{n-1} - a \cdot \left(3^{n-1} - 2^{n-1}\right) > 0 , \qquad (73)$$

i.e.

$$a < \frac{3^{n-1}}{3^{n-1}-2^{n-1}}\ , \tag{74}$$

then inequality (72) is written as

$$3^{n-1}-2^{n-1} \geqslant 3^{n-1}-a\cdot\left(3^{n-1}-2^{n-1}\right),$$

whence

$$\frac{2^{n-1}}{3^{n-1}-2^{n-1}} \leqslant a\,. \tag{75}$$

Therefore, situation (64) is optimal if inequality (69) holds along with inequalities (74) and (75). However,

$$\begin{aligned}
&\frac{3^{n-1}}{3^{n-1}-2^{n-1}}-\frac{3^{n-2}\cdot 2^{n-2}}{\left(3^{n-1}-2^{n-1}\right)\left(3^{n-2}-2^{n-2}\right)}= \\
&=\frac{3^{n-1}\cdot 3^{n-2}-3^{n-1}\cdot 2^{n-2}-3^{n-2}\cdot 2^{n-2}}{\left(3^{n-1}-2^{n-1}\right)\left(3^{n-2}-2^{n-2}\right)}= \\
&=\frac{3^{n-1}\cdot 3^{n-2}-4\cdot 3^{n-2}\cdot 2^{n-2}}{\left(3^{n-1}-2^{n-1}\right)\left(3^{n-2}-2^{n-2}\right)}= \\
&=\frac{3^{n-2}\cdot\left(3^{n-1}-2^{n}\right)}{\left(3^{n-1}-2^{n-1}\right)\left(3^{n-2}-2^{n-2}\right)}>0
\end{aligned} \tag{76}$$

due to

$$3^{n-1} > 2^{n} \tag{77}$$

for $n \geqslant 3$.

Indeed, inequality (77) is true for $n = 3$:

$$3^2 = 9 > 8 = 2^3\,.$$

Assume that inequality (77) holds for $n = k$:

$$3^{k-1} > 2^{k}\,. \tag{78}$$

For $n = k + 1$ inequality (77) turns into

$$\begin{aligned}
&3^{k} > 2^{k+1}\,, \\
&3\cdot 3^{k-1} > 2\cdot 2^{k}\,, \\
&\frac{3}{2}\cdot 3^{k-1} > 2^{k}\,,
\end{aligned} \tag{79}$$

whence inequality (79) holds due to inequality (78) holds. Inequality (76) means that

$$\frac{3^{n-2}\cdot 2^{n-2}}{\left(3^{n-1}-2^{n-1}\right)\left(3^{n-2}-2^{n-2}\right)} < \frac{3^{n-1}}{3^{n-1}-2^{n-1}}$$

for $n \geq 3$ and thus it is sufficient to consider only stronger inequality (69), upon which weaker inequality (74) holds. Hence, situation (64) is optimal if inequality (69) holds along with inequality (75), i.e. if

$$a \in \left[\frac{2^{n-1}}{3^{n-1}-2^{n-1}};\ \frac{3^{n-2}\cdot 2^{n-2}}{\left(3^{n-1}-2^{n-1}\right)\left(3^{n-2}-2^{n-2}\right)}\right]. \tag{80}$$

The difference between the right and left endpoints of the interval in membership (80) is:

$$\begin{aligned}
&\frac{3^{n-2}\cdot 2^{n-2}}{\left(3^{n-1}-2^{n-1}\right)\left(3^{n-2}-2^{n-2}\right)}-\frac{2^{n-1}}{3^{n-1}-2^{n-1}}= \\
&=\frac{3^{n-2}\cdot 2^{n-2}-2^{n-1}\cdot 3^{n-2}+2^{n-1}\cdot 2^{n-2}}{\left(3^{n-1}-2^{n-1}\right)\left(3^{n-2}-2^{n-2}\right)}= \\
&=\frac{2^{n-1}\cdot 2^{n-2}+3^{n-2}\cdot 2^{n-2}\cdot(1-2)}{\left(3^{n-1}-2^{n-1}\right)\left(3^{n-2}-2^{n-2}\right)}= \\
&=\frac{2^{n-1}\cdot 2^{n-2}-3^{n-2}\cdot 2^{n-2}}{\left(3^{n-1}-2^{n-1}\right)\left(3^{n-2}-2^{n-2}\right)}= \\
&=\frac{2^{n-2}\cdot\left(2^{n-1}-3^{n-2}\right)}{\left(3^{n-1}-2^{n-1}\right)\left(3^{n-2}-2^{n-2}\right)}\ .
\end{aligned} \tag{81}$$

Fraction (81) is nonnegative only for $n = 3$. Indeed, inequality

$$2^{n-1} > 3^{n-2} \tag{82}$$

holds for $n = 3$ as

$$2^2 = 4 > 3 = 3^1,$$

but for $n = k$ there is inequality

$$2^{n-1} < 3^{n-2} \tag{83}$$

turning into

$$2^3 = 8 < 9 = 3^2\,,$$

and, assuming that for $n = k$ inequality (83) holds as

$$2^{k-1} < 3^{k-2}\,, \tag{84}$$

for $n = k + 1$ inequality (83) turns into

$$\begin{aligned}
&2^{k} < 3^{k-1}, \\
&2\cdot 2^{k-1} < 3\cdot 3^{k-2}, \\
&2^{k-1} < \frac{3}{2}\cdot 3^{k-2}\,,
\end{aligned} \tag{85}$$

whence inequality (85) holds due to inequality (84) holds. For $n = 3$ the interval in membership (80) turns into:

$$\left[\frac{2^2}{3^2-2^2};\frac{3^1\cdot 2^1}{\left(3^2-2^2\right)\left(3^1-2^1\right)}\right]=\left[\frac{4}{5};\frac{6}{5}\right].$$

Therefore, the duel has an optimal pure strategy situation (62) by (63). □

8. Last possible-shooting moment optimality

A corollary from *Theorem 5* is that 4×4 and bigger LA1BSDs by

$$a\in\left(0;\frac{4}{5}\right)\cup\left(\frac{6}{5};2\right) \tag{86}$$

do not have optimal pure strategy situations corresponding to all possible-shooting moments, except for the last one. The optimality of last-moment situation (15) is ascertained below for 5×5 and bigger LA1BSDs.

Theorem 6. In progressive LA1BSD (6) by (1)-(3), (36) for $N\in\mathbb{N}\setminus\{1,2,3,4\}$ **and**

$$a\in\left(0;\frac{2^{N-2}}{3^{N-2}-2^{N-2}}\right] \tag{87}$$

situation (15) is single optimal.

Proof. Situation (15) is optimal only if the last row of matrix (2) is nonnegative. Thus, the last, *N*-th, row of matrix (2) contains a saddle point if inequality

$$\begin{gathered}k_{Nj}=a-ay_j-a^2y_j\geqslant 0\\ \forall\ y_j<1\quad(\forall\ j=\overline{1,N-1})\end{gathered} \tag{88}$$

holds. It is easy to see in (88) that if inequality

$$1-y_{N-1}-ay_{N-1}\geqslant 0 \tag{89}$$

is true, then inequality (88) is true as well. From inequality (89) it follows that

$$\frac{1-y_{N-1}}{y_{N-1}}\geqslant a, \tag{90}$$

$$\frac{1-\dfrac{3^{N-2}-2^{N-2}}{3^{N-2}}}{\dfrac{3^{N-2}-2^{N-2}}{3^{N-2}}}\geqslant a, \tag{91}$$

$$\frac{2^{N-2}}{3^{N-2}-2^{N-2}}\geqslant a, \tag{92}$$

whence (87) implies optimality of situation (15). Meanwhile, inequality

$$\frac{2^{N-2}}{3^{N-2}-2^{N-2}}\leqslant\frac{8}{19}<\frac{4}{5} \tag{93}$$

holds for $N\in\mathbb{N}\setminus\{1,2,3,4\}$. Indeed, from inequality (93) it follows that

$$19\cdot 2^{N-2}\leqslant 8\cdot 3^{N-2}-8\cdot 2^{N-2},$$

$$27\cdot 2^{N-2}\leqslant 8\cdot 3^{N-2},$$

$$3^3\cdot 2^{N-2}\leqslant 2^3\cdot 3^{N-2},$$

whence

$$2^{N-5}\leqslant 3^{N-5}$$

for $N\in\mathbb{N}\setminus\{1,2,3,4\}$.

Inequality (93) implies that

$$\left(0;\frac{2^{N-2}}{3^{N-2}-2^{N-2}}\right]\subseteq\left(0;\frac{8}{19}\right]\subset\left(0;\frac{4}{5}\right) \tag{94}$$

for $N\in\mathbb{N}\setminus\{1,2,3,4\}$.

Membership (94) with the inclusion obeys membership (86), which implies that by (87) situation (15) in 5×5 and bigger LA1BSDs is single optimal. □

Inequality (93) is false for $N=4$ as

$$\frac{2^2}{3^2-2^2}=\frac{4}{5}.$$

This leads to a specificity of 4×4 LA1BSDs by (87).

Theorem 7. In progressive 4×4 **LA1BSD (6) by (1)-(3), (36) for** $N=4$ **and**

$$a\in\left(0;\frac{4}{5}\right) \tag{95}$$

situation (15) is single optimal. The 4×4 **LA1BSD by**

$$a=\frac{4}{5} \tag{96}$$

has four optimal pure strategy situations: (62),

$$\{x_3,y_4\}=\left\{\frac{5}{9},1\right\}, \tag{97}$$

$$\{x_4,y_3\}=\left\{1,\frac{5}{9}\right\}, \tag{98}$$

and (15).

Proof. Situation (15) is single optimal if the last, fourth, row of matrix (2) is positive, except for entry $k_{44}=0$. In *Theorem 6*, it follows from (88)–(92) for $N=4$ that situation (15) is single optimal when

$$\frac{2^{N-2}}{3^{N-2}-2^{N-2}}=\frac{4}{5}>a, \tag{99}$$

i.e. if membership (95) is true. If (96) is true, situation (15) is optimal as well owing to (88)–(92) hold for $N = 4$. In addition, situation (62) is optimal in accordance with *Theorem 5* as membership (63) is also true. This additionally implies optimality of situations (97) and (98).□

9. Non-solvability in pure strategies

Just like the LA1BSDs for patterns (7) and (23), the LA1BSD for pattern (36) is not solved in pure strategies within a subset of values of the accuracy proportionality factor. This is proved by the two following assertions.

Theorem 8. Progressive 4×4 LA1BSD (6) by (1)–(3), (36) for $N = 4$ is not solved in pure strategies by

$$a \in \left(\frac{6}{5}; 2\right). \qquad (100)$$

Proof. The 4×4 LA1BSD is solved in pure strategies by $a \geq 2$ (*Theorem 3*) and by (63) (*Theorem 5*) and by (95) (*Theorem 7*). By the remaining interval in (100), as the corollary from Theorem 5, the 4×4 LA1BSD does not have an optimal pure strategy situation that would contain three possible-shooting moments

$$\{t_1, t_2, t_3\} = \left\{0, \frac{1}{3}, \frac{5}{9}\right\}.$$

The last possible-shooting moment is non-optimal if, as a corollary from (88)–(93) in *Theorem 6* and *Theorem 7*, inequality (92) for $N = 4$ is false, i.e.

$$\frac{4}{5} < a, \qquad (101)$$

which is true by (100). □

Theorem 9. Progressive LA1BSD (6) by (1)-(3), (36) for $N \in \mathbb{N} \setminus \{1, 2, 3, 4\}$ is not solved in pure strategies by

$$a \in \left(\frac{2^{N-2}}{3^{N-2} - 2^{N-2}}; \frac{4}{5}\right) \cup \left(\frac{6}{5}; 2\right). \qquad (102)$$

Proof. Once again, the LA1BSD is solved in pure strategies by $a \geq 2$ (*Theorem 3*) and by (63) (*Theorem 5*) and by (87) (*Theorem 6*). Then, the corollary from *Theorem 5* and the corollary from *Theorem 6*, – particularly, with membership (94) and its inclusions, – is that the LA1BSD does not have optimal pure strategy situations by (102). □

It is easy to see that the subset in (102) of pure-strategy-solution non-existence expands as the duel becomes bigger.

Theorem 10. As the number of possible-shooting moments in progressive LA1BSD (6) by (1)-(3), (36) for $N \in \mathbb{N} \setminus \{1, 2, 3, 4\}$ is increased, the last-moment-optimality interval by (87) shortens.

Proof. This assertion means that

$$\lim_{N \to \infty} \left(0; \frac{2^{N-2}}{3^{N-2} - 2^{N-2}}\right] = \varnothing. \qquad (103)$$

Consider a function

$$f(N) = \frac{2^{N-2}}{3^{N-2} - 2^{N-2}}. \qquad (104)$$

The first derivative of function (104) is

$$\frac{df}{dN} = \frac{(\ln 2) \cdot 2^{N-2} \cdot \left(3^{N-2} - 2^{N-2}\right) - 2^{N-2}}{\left(3^{N-2} - 2^{N-2}\right)^2} \times$$
$$\times \frac{\left((\ln 3) \cdot 3^{N-2} - (\ln 2) \cdot 2^{N-2}\right)}{\left(3^{N-2} - 2^{N-2}\right)^2} =$$
$$= 2^{N-2} \cdot \frac{(\ln 2) \cdot 3^{N-2} - (\ln 2) \cdot 2^{N-2} - (\ln 3)}{\left(3^{N-2} - 2^{N-2}\right)^2} \times$$
$$\times \frac{3^{N-2} + (\ln 2) \cdot 2^{N-2}}{\left(3^{N-2} - 2^{N-2}\right)^2} =$$
$$= 2^{N-2} \cdot 3^{N-2} \cdot \frac{\ln 2 - \ln 3}{\left(3^{N-2} - 2^{N-2}\right)^2} < 0,$$

which means that (104) is a decreasing function of N. That is,

$$\lim_{N \to \infty} f(N) = \lim_{N \to \infty} \frac{2^{N-2}}{3^{N-2} \cdot \left(1 - \left(\frac{2}{3}\right)^{N-2}\right)} = 0,$$

whence (103) is true. □

Thus, as the duel becomes bigger, the non-constant interval in (102) becomes wider, expanding the accuracy subset of pure-strategy-solution non-existence towards

$$\left(0; \frac{4}{5}\right) \cup \left(\frac{6}{5}; 2\right) \qquad (105)$$

for LA1BSDs with five and more possible-shooting moments.

10. Discussion and conclusion

Compared to the LA1BSDs for patterns (7) and (23), the LA1BSD with progressing-by-one-

third shooting moments has a different boundary value of the accuracy proportionality factor, which separates two major cases of the duel solution. The LA1BSD for pattern (36) with four and more possible-shooting moments by $a \geq 2$ has the single optimal situation (49), according to which the duelist must shoot at the second moment being the first third of the duel time span (*Theorem 3*). When there are only three possible-shooting moments, the second moment is single optimal if $a > 2$, the last moment is single optimal if $a \in (0;2)$, the second and last moments are both optimal if $a = 2$ (*Theorem 2*).

When $a \in (0;2)$ and there are three or more possible-shooting moments, the second moment is never optimal for the duelist (*Theorem 4*). This is the case, where LA1BSD with progressing-by-one-third shooting moments significantly differs (in terms of its solution) from the LA1BSDs for patterns (7) and (23). Thus, in LA1BSDs for pattern (36) with four and more possible-shooting moments third moment $t_3 = \frac{5}{9}$ is optimal by (63) (*Theorem 5*), whereas third moment $t_3 = \frac{2}{3}$ is optimal in the LA1BSD for compactified-moments pattern (23) only if $a = \frac{1}{2}$ [13]. In the LA1BSD for geometrical-progression pattern (7) third moment $t_3 = \frac{3}{4}$ is particularly optimal if

$$a \in \left[\frac{1}{3}; \frac{2}{3}\right],$$

although optimality of later possible-shooting moments is also possible [15].

Just like for patterns (7) and (23), the last moment can be optimal in LA1BSDs for pattern (36) with four and more possible-shooting moments by sufficiently low values of the accuracy proportionality factor. The last moment is optimal if (87) is true (*Theorems 6* and *7*), where the length of the interval in (87) exponentially-like shortens as the number of possible-shooting moments (the size of the duel) is increased (*Theorem 10*). This last-moment-optimality interval shortening exists for patterns (7) and (23) as well, whose right endpoints in the interval are

$$\frac{1}{2^{N-2}-1}$$

and

$$\frac{1}{N-2},$$

respectively. Last-moment-optimality solutions of LA1BSDs for patterns (7), (23), and (36) with exactly four possible-shooting moments cannot be seamlessly surveyed. The 4×4 LA1BSD for geometrical-progression pattern (7) is not specifically distinguished from bigger LA1BSDs. Unlike LA1BSDs with the faster converging possible-shooting moments by (7), the duelist in the 4×4 LA1BSD with compactified shooting moments by (23) and $a \in \left(0; \frac{1}{2}\right)$ has the single optimal strategy to shoot at the duel very end. If the accuracy proportionality factor is equal to $\frac{1}{2}$, then the duelist in the 4×4 LA1BSD for pattern (23) possesses two optimal pure strategies $t_3 = \frac{2}{3}$ and $t_4 = 1$. This resembles the optimal behavior of the duelist in the 4×4 LA1BSD for pattern (36) and (96), where it is optimal to shoot at either $t_3 = \frac{5}{9}$ or $t_4 = 1$. If (95) is true, the last moment remains single optimal (*Theorem 7*).

Unlike the LA1BSD for pattern (23), which is not solved in pure strategies if

$$a \in \left(\frac{1}{N-2}; 1\right) \setminus \left\{\frac{1}{2}\right\} \qquad (106)$$

for $N \in \mathbb{N} \setminus \{1, 2, 3\}$ and the interval in (106) approaches to open interval (0;1) as the number of possible-shooting moments is increased, the LA1BSD for pattern (36) does not have a pure strategy solution by (102) (*Theorem 9*), i.e. there is a stable infinite subset of values of the accuracy proportionality factor below the boundary value $a = 2$ such that a pure strategy solution exists – see (63) and *Theorem 5*. This subset, whose length is $\frac{2}{5}$ comprising 20 % of the below-boundary-value interval, changes into interval

$$\left(0; \frac{6}{5}\right] \qquad (107)$$

in a 4×4 LA1BSD for pattern (36) (*Theorems 7* and *8*). Interval (107) comprises 60 % of the below-boundary-value interval (0;2).

The proved assertions contribute another specificity of the progressing-by-one-third shooting moments in LA1BSDs to the games of timing. Compared to LA1BSDs for patterns (7) and (23), the specificity consists in that the LA1BSD for pattern (36) has a constant interval of lower (weaker) shooting accuracies, at which the duelist possesses an optimal pure strategy. This interval is $\left[\frac{4}{5}; \frac{6}{5}\right]$ that symmetrically breaks the low-accuracy interval (0;2).

LA1BSDs with progressing-by-one-third shooting moments can be further studied for some

nonlinearities in the accuracy function. For instance, it can be the quadratic accuracy as a case of the low-accurate duelist [10]. For a case of the high-accurate duelist, it is the square-root accuracy. Besides, the case of a value of the jitter added to progressing-by-one-third shooting moments, apart from the duel beginning and end time moments, can be considered [18].

References

[1] E.N. Barron, Game theory : an introduction (2nd ed.), Wiley, Hoboken, New Jersey, USA, 2013. doi.org/ 10.1002/9781118547168

[2] R.A. Epstein, The theory of gambling and statistical logic (2nd ed.), *Academic Press*, Burlington, Massachusetts, USA, 2013. doi.org/10.1016/C2009-0-20160-7

[3] S. Karlin, The Theory of Infinite Games. Mathematical Methods and Theory in Games, Programming, and Economics, Pergamon, London – Paris, 1959. Available: https://www.abebooks.co.uk/9780486670201/Mathematics-Methods-Theory-Games-Programming-0486670201/plp

[4] T. Radzik, "Results and Problems in Games of Timing. Statistics, Probability and Game Theory", *Lecture Notes – Monograph Series*, 1996, Vol. 30, pp. 269–292. Available: https://projecteuclid.org/ebooks/institute-of-mathematical-statistics-lecture-notes-monograph-series/Statistics-probability-and-game-theory/chapter/Results-and-problems-in-games-of-timing/10.1214/lnms/1215453577.pdf

[5] C. Aliprantis and S. Chakrabarti, *Games and Decision Making*, *Oxford University Press*, Oxford, UK, 2000. Available: https://www.researchgate.net/publication/265763144_Games_and_Decision_Making

[6] S. Alpern and J.V. Howard, "A short solution to the many-player silent duel with arbitrary consolation prize", *European Journal of Operational Research*, 2019, Vol. 273, Iss. 2, pp. 646 –649. Available: https://doi.org/10.1016/j.ejor.2018.08.040

[7] V.V. Romanuke, Theory of Antagonistic Games, New World – 2000, Lviv, 2010.

[8] V.V. Romanuke, "Fast solution of the discrete noiseless duel with the nonlinear scale on the linear accuracy functions", *Herald of Khmelnytskyi national university. Economical sciences*, 2010, Vol. 5, Iss. 4, pp. 61–66. Available: https://lib.khmnu.edu.ua/inf_res/bibliogr/dor/2010/inoz.htm

[9] V.V. Romanuke, "Discrete progressive noiseless duel with skewsymmetric kernel on the finite grid of the unit square with identical nonlinear accuracy functions of the players", *Bulletin of V. Karazin Kharkiv National University. Series "Mathematical Modelling. Information Technology. Automated Control Systems"*, 2010, Vol. 890, Iss. 13, pp. 195–204.

[10] V.V. Romanuke, "Pure strategy saddle point in progressive discrete silent duel with quadratic accuracy functions of the players", *Visnyk of the Lviv University. Series Appl. Math. and Informatics*, 2023, Iss. 31, pp. 75–86. Available: https://doi.org/10.30970/vam.2023.31.11716

[11] J.F. Reinganum, "Chapter 14 – The Timing of Innovation: Research, Development, and Diffusion", In: R. Willig and R. Schmalensee (Eds.), *Handbook of Industrial Organization, Elsevier*, North-Holland, 1989, Vol. 1, pp. 849–908. Available: https://doi.org/10.1016/S1573-448X(89)01017-4

[12] V.V. Romanuke, "Discrete noiseless duel with a skewsymmetric payoff function on the unit square for models of socioeconomic competitive processes with a finite number of pure strategies", *Cybernetics and Systems Analysis*, 2011, Vol. 47, Iss. 5, pp. 818–826. Available: https://doi.org/10.1007/s10559-011-9361-z

[13] V.V. Romanuke, "Pure strategy solutions in progressive discrete silent duel with linear accuracy and compactified shooting moments", *Visnyk of the Lviv University. Series Appl. Math. and Informatics*, 2024, Iss. 32, pp. 15–27. Available: https://doi.org/10.30970/vam.2024.32.12344

[14] B. Viscolani, "Pure-strategy Nash equilibria in an advertising game with interference", *European Journal of Operational Research*, 2012, vol. 216, iss. 3, pp. 605–612. Available: https://doi.org/10.1016/j.ejor.2011.08.002

[15] V.V. Romanuke, "Pure strategy saddle points in the generalized progressive discrete silent duel with identical linear accuracy functions", *Journal of Information and Organizational Sciences*, 2024, Vol. 48, No. 1, pp. 81–98. Available: https://doi.org/10.31341/jios.48.1.4

[16] J.P. Lang and G. Kimeldorf, "Duels with continuous firing", *Management Science*, 1975, Vol. 22, Iss. 4, pp. 470–476. Available: https://www.jstor.org/stable/2630111

[17] R. Laraki *et al.*, "Continuous-time games of timing", *Journal of Economic Theory*, 2005, Vol. 120, Iss. 2, pp. 206–238. Available: https://doi.org/10.1016/j.jet.2004.02.001

[18] V.V. Romanuke, "Pure strategy solutions in the progressive discrete silent duel with identical linear accuracy functions and shooting uniform jitter", *Journal of Mathematics and Applications*, 2024, Vol. 47, pp. 91–108. Available: https://doi.org/10.7862/rf.2024.6

[19] J.-H. Steg, "On identifying subgame-perfect equilibrium outcomes for timing games", *Games and Economic Behavior*, 2022, Vol. 135, pp. 74–78. Available: https://doi.org/10.1016/j.geb.2022.05.012

[20] V.V. Romanuke, “Finite uniform approximation of two-person games defined on a product of staircase-function infinite spaces”, *International Journal of Approximate Reasoning*, 2022, Vol. 145, pp. 139–162. Available: https://doi.org/10.1016/j.ijar.2022.03.005

[21] C. Bobtcheff and T. Mariotti, “Potential competition in preemption games”, *Games and Economic Behavior*, 2012, Vol. 75, Iss. 1, pp. 53–66. Available: https://doi.org/10.1016/j.geb.2011.11.002

[22] J. Huang *et al.*, “Recent developments in dynamic advertising research”, *European Journal of Operational Research*, 2012, Vol. 220, Iss. 3, pp. 591–609. Available: https://doi.org/10.1016/j.ejor.2012.02.031

[23] R. Argenziano and P. Schmidt-Dengler, “Competition, timing of entry and welfare in a preemption game”, *Economics Letters*, 2013, Vol. 120, Iss. 3, pp. 509–512. Available: https://doi.org/10.1016/j.econlet.2013.06.009

В.В. Романюк

БЕЗШУМНА ДУЕЛЬ З ОДНІЄЮ КУЛЕЮ ЛІНІЙНОЇ ВЛУЧНОСТІ ТА ПРОГРЕСУЮЧИМИ НА ОДНУ ТРЕТИНУ МОМЕНТАМИ ПОСТРІЛУ

Проблематика. Розглянуто скінченну гру з нульовою сумою, яка моделює конкуруючу взаємодію між двома суб’єктами. Суб’єкт, якого ще називають дуелянтом, має виконати якусь дію (або, висловлюючись метафорично, здійснити постріл однією кулею) протягом стандартизованого проміжку часу, де куля може бути випущена лише у зазначені моменти часу. Для більш реалістичного симулювання взаємодії між дуелянтами кількість таких моментів можливого пострілу приймають скінченною, внаслідок чого гра (або ж дуель) стає дискретною. Для дуелянта залишається невідомим до кінця дуелі, чи інший дуелянт здійснив постріл і коли він відбувся. Дуелянт може не стріляти аж до самого кінця дуелі, але тоді постріл одначе здійснюється автоматично у цей кінцевий момент часу, оскільки дія має бути виконана у будь-якому випадку. Дуелянт виграє від здійснення пострілу якомога пізніше, але лише тоді, коли він випередить іншого дуелянта.

Мета дослідження. Мета полягає у тому, щоб для деякої моделі дискретної прогресії дуелі визначити оптимальну поведінку дуелянтів, за якої напруга збільшується з наближенням кінця дуелі та з’являється більше можливостей для пострілу.

Методика реалізації. Обидва дуелянти діють за тих самих умов, тому ця безшумна дуель з однією кулею є симетричною. Відтак оптимальне значення гри дорівнює 0, і дуелянти мають однакові оптимальні стратегії. Влучність пострілу є лінійною і визначається коефіцієнтом пропорційності точності.

Результати дослідження. Усі розв’язки у чистих стратегіях для таких дуелей знайдені залежно від цього коефіцієнта, де моменти можливого пострілу складають модель деякої прогресії. Згідно з цією моделлю кожний наступний момент можливого пострілу отримують додаванням третини часового проміжку, що залишається до кінця дуелі. Розв’язки для цієї моделі порівнюються з відомими розв’язками для моделі геометричної прогресії, а також моделі, в якій моменти можливого пострілу прогресують більш помірно.

Висновки. Доведені твердження розкривають ще одну особливість прогресуючих на одну третину моментів пострілу у безшумних дуелях з однією кулею лінійної влучності у класі часових ігор. Якщо порівнювати дуелі з іншими моделями дискретної прогресії, ця особливість полягає у тому, що дуель із прогресуючими на одну третину моментами пострілу має постійний інтервал нижніх (слабших) влучностей, за яких дуеліст має оптимальну чисту стратегію. Цим інтервалом є $\left[\frac{4}{5};\frac{6}{5}\right]$, який симетрично розбиває інтервал (0; 2) слабкої влучності.

Ключові слова: безшумна дуель з однією кулею; лінійна влучність; матрична гра; розв’язок у чистих стратегіях; прогресуючі на одну третину моменти пострілу.

Рекомендована Радою
факультету прикладної математики
КПІ ім. Ігоря Сікорського

Надійшла до редакції
18 серпня 2025 року

Прийнята до публікації
08 грудня 2025 року

DOI: https://doi.org/10.20535/kpisn.2025.4.344350
UDC 519.6; 615.015.8

D.S. Horodetskyi[1*], M.P. Smetiukh[1,2], S.O. Soloviov[1,2]
[1]National Technical University of Ukraine
"Igor Sikorsky Kyiv Polytechnic Institute", Kyiv, Ukraine,
[2]Shupyk National Healthcare University of Ukraine, Kyiv, Ukraine
[*]Corresponding author: dgolodetsky37@gmail.com

DECISION MAKING IN ANTI-CORONAVIRUS DRUG DISCOVERY: MATHEMATICAL MODELLING AND VALUE OF INFORMATION ANALYSIS

Background. The process of preclinical evaluation of antiviral medications typically involves multiple stages, each containing substantial uncertainties. Traditional methods for screening the compounds often lack structured means for optimising the decision-making and calculating the feasibility and risks of transitions between all of the stages. Thus, there appears to be a problem with the inefficient selection of promising antiviral molecules, which subsequently increases the probability of choosing suboptimal research trajectories.
Objective. The paper aims to develop a computational framework for optimising of the transition between stages in preclinical antiviral testing. The system focuses on the integration of decision trees and Markov models in order to include effectiveness, risks and the value of additional information into assessment, supporting an in-depth planning of preclinical research pipelines.
Methods. Experimental data from molecular docking, cytotoxicity CD_{50}, and antiviral activity IC_{50} were used in a multi-stage evaluation system with CTI ≥ 4 being the criterion for progression into further stages. Decision trees provided the explicit rules for advancement of the compounds, while Markov models added context for building sequential strategies under uncertainty and quantified the feasibility of movement to the next stage. Value of information analysis added the assessment of the expected benefit of additional data.
Results. The developed framework consistently produced reliable technical results. The decision used in CTI ≥ 4.0 prediction stage demonstrated a conservative classification pattern, correctly identifying compounds with high therapeutic potential while missing some effective candidates. The Markov model showed steadily increasing state values in docking, cytotoxicity, and antiviral testing phases that confirmed the growth of expected utility. Based on the findings acquired, the most effective solutions were identified for the ongoing investigation into antiviral assays, while the application of value of information analysis indicated that the largest gain occurred after antiviral activity testing, whereas the initial phases serve as filters.
Conclusions. The study showed that both decision trees and Markov models capture different but complementary aspects of the preclinical evaluation process. Decision trees provide an interpretable set of rules that formalise how molecular docking and cytotoxicity measurement influence the progression of compounds, while their limited sensitivity at the CTI threshold highlighted the complexity of predicting the final success of the evaluated compounds. The Markov model simulations showed that the full three-stage pipeline is justified and that progression decisions are influenced by both uncertainty and experimental cost. The value of information analysis clarifies the importance of each stage, helping to emphasise the role of antiviral activity data. These findings support the integration of analytic methods for improving the structure, transparency and efficiency of antiviral preclinical research.
Keywords: coronavirus; drug; preclinical evaluation; decision tree; Markov decision process; value of information.

Introduction

The optimisation of sequential decision-making in preclinical studies of antiviral compounds remains a highly relevant challenge due to the combination of uncertainty, high experimental costs, and limited predictability of candidate efficacy. At each stage of the preclinical pipeline – from in silico screening to cytotoxicity assessment and antiviral activity tests – researchers must make a series of decisions,

Пропозиція для цитування цієї статті: Д.С. Городецький, М.П. Сметюх, С.О. Соловйов, «Прийняття рішень у процесі доклінічної розробки противірусних препаратів проти коронавірусу: математичне моделювання та аналіз цінності інформації», *Наукові вісті КПІ*, № 4, с. 20–30, 2025. doi: https://doi.org/10.20535/kpisn.2025.4.344350

Offer a citation for this article: D.S. Horodetskyi, M.P. Smetiukh, S.O. Soloviov, "Decision making in anti-coronavirus drug discovery: mathematical modelling and value of information analysis", *KPI Science News*, No. 4, pp. 20–30, 2025. doi: https://doi.org/10.20535/kpisn.2025.4.344350

where an inaccurate early-stage choice leads to the loss of time, resources, and potentially promising compounds. This creates the need for systematic approaches capable of increasing the rationality and economic efficiency of the preclinical process.

Despite significant progress in artificial intelligence, current research mainly improves individual steps of drug discovery rather than the full decision-making pipeline. Modern machine learning techniques demonstrate substantial advances in virtual screening, toxicity prediction, and target selection [1]. AI-based integration with organ-on-a-chip platforms and digital twins enhances the accuracy of pharmacokinetic and toxicological modelling [2]. Data-driven design of antiviral peptides using GANs, deep learning and explainable AI demonstrates strong potential for optimising candidate properties [3]. Studies of DHODH inhibitors highlight the complexity of translating promising in vitro results into clinical effects and emphasise the need for step-wise risk assessment [4]. Multi-omics deep learning pipelines accelerate early discovery and facilitate drug repositioning [5]. AI-based prediction of viral mutations supports personalised antiviral strategies and shows the sequential, dynamic nature of decision-making in virology [6]. AI-driven dereplication and classification of natural products further illustrate the need for structured transitions between preclinical stages [7].

However, these advances primarily address predictive accuracy rather than the principled optimisation of decisions across multiple stages. Current research lacks integrated mathematical frameworks that would: formalise transitions between preclinical stages, quantify risks and probabilities of success, incorporate the cost and value of information, and determine when experimental continuation is economically justified. Decision trees and Markov processes are rarely applied specifically to antiviral preclinical pipelines, leaving a methodological gap in modelling sequential choices under uncertainty.

The study aims to develop and evaluate formalised approaches for optimising sequential decision-making in preclinical antiviral research using decision tree models and Markov decision processes. These models are applied to real-world experimental datasets to quantify transition probabilities, estimate costs, and compare the effectiveness of alternative strategies.

The scientific novelty of the work lies in the integration of an interpretable set of rules provided by the decision trees with globally optimal Markov strategies and value of information analysis. Unlike prior studies, in the proposed framework, predictive patterns, uncertainty quantification, experimental costs and utility maximisation are combined into a unified scheme that supports planning throughout the entire preclinical process.

Problem statement

The object of the study is the process of preclinical evaluation of antiviral drugs, while the subject is mathematical methods for optimising sequential decision-making in this process, in particular decision trees and Markov models. The purpose of the work is to develop and test formalised approaches to assessing the effectiveness, risks and feasibility of transitions between stages of preclinical studies based on real experimental data. The end result is the construction and comparative analysis of two algorithmic models – the decision tree and the Markov process – that demonstrate their ability to support rational, data-driven planning for preclinical testing of antiviral candidates.

Materials and methods

The study uses three interrelated methods: decision trees to formalise the process of selecting compounds, Markov models to describe the sequence of experimental steps over time and value of information analysis metrics to quantify the feasibility of doing additional measurements. This combination allows for moving from the description of individual experiments to a systematic approach where each step is considered to be an element of an optimised decision-making process.

Decision trees act as interpreted classification models that reflect the relationship between a set of input parameters (docking parameters, concentration characteristics, toxicity and antiviral activity indicators) and binary output events (e.g., reaching a chemotherapy index threshold). The decision tree is a hierarchical structure, where each inner node corresponds to a condition of the type "sign ≤ threshold", branches to alternative consequences of this condition, and leaf nodes to result classes. The construction of the tree is carried out by sequentially dividing the feature space to minimise the degree of heterogeneity (for example, the Gini index) in the daughter nodes at each stage. As a result, a set of simple logical rules is formed that allows for explicit interpretation of which combinations of docking, CD_{50}, ID_{50}, and exposure.

Markov chains and Markov decision-making processes are used to describe the evolution of a system in discrete states, taking into account the pro-

babilistic nature of transitions between them. In the simplest case, the Markov chain is given by a set of states and a matrix of transient probabilities, where the probability of moving to the next state depends only on the current state, and not on the complete history. In the context of planning the sequence of experiments, this allows us to consider individual stages (docking, assessment of cytotoxicity, testing of antiviral activity, achievement or failure of therapeutic success) as states of the Markov process, and possible actions of the investigator ("to continue" or "stop" the study at a certain stage) as controlling influences that change the distribution of probabilities of further states. In this formulation, the Markov model of decision-making is used, where each state-action pair corresponds not only to the probability of transition, but also to a certain instantaneous reward or cost, and the optimal strategy is determined by solving the Bellman equations for the value function.

Value-of-information analysis metrics are tools for evaluating the extent to which the anticipated utility of decisions can be enhanced through additional data. Conceptually, the value of information is defined as the difference between the expected utility of an optimal policy given the availability of additional information and the expected utility at the baseline level of uncertainty. The Total Value of Perfect Information (EVPI) reflects a hypothetical increment if the results of the experiments were known in advance without errors; partial value of perfect information (EVPPI) characterizes a similar increase for certain groups of parameters (for example, only for cytotoxicity indicators or only for antiviral activity); The expected value of the sample information (EVSI) assesses how much conducting a realistic incremental experiment with a certain value is able to improve decision-making. In combination with the Markov model of the experimental process, these metrics enable a quantitative comparison of various research design variants, determine the stages at which new measurements give the greatest increase in information about CTI, and justify the optimal balance between the costs of the experiment and the probability of obtaining therapeutically significant candidates.

The study used a multi-level methodology combining experimental data on docking, cytotoxicity, and antiviral activity with mathematical dose-response modelling, decision tree construction, and Markov experiment sequence modelling. The main target characteristic is the CTI chemotherapy index, calculated based on CD_{50} and ID_{50} concentrations for each test sample and cell processing regimen.

Baseline data included energy parameters of molecular docking of a series of candidate compounds to the domains of the spike protein of the virus and the main protease, results of cytotoxicity tests on the cell line at two time points (24 and 48 h) and results of tests of antiviral activity in the therapeutic (L) and therapeutic-prophylactic (LP) modes. For the docking, numerical estimates of binding energy (in conventional units of energy) with individual target sites were considered, which are represented as $SP_1 - SP_5$ for the spike protein and $MP_1 - MP_3$ for the main protease. For each compound, a docking parameter vector was obtained, which was further used as an input trait space in decision tree models.

Dose-effect modelling for cytotoxicity and antiviral activity was carried out using a four-parameter sigmoidal model. For each compound, exposure time, and treatment regimen, a set of concentrations was given $\boldsymbol{x}_i$ and the corresponding measured values of relative cell viability (for cytotoxicity) or relative viral activity (for antiviral action), normalised to control in the interval [0; 1]. As a model function, the expression

$$f(x)=\frac{a}{1+e^{(-bx+c)}}+d \qquad (1)$$

where x is the concentration of the compound, $f(x)$ is the expected relative value of the indicator (viability or activity), a, b, c, d are unknown parameters of the curve describing the amplitude of the effect, the steepness of the transition, the shift along the concentration axis and the baseline, respectively. The estimation of the parameters was carried out by the method of least squares by minimising the root mean square error

$$MSE(a,b,c,d)=\frac{1}{N}\sum_{i=1}^{N}(y_i - \\ - f(x_i,a,b,c,d))^2 \qquad (2)$$

where y_i – experimental values of the relative viability of cells or the relative activity of the virus, N is the number of points of the curve. Optimisation was carried out by the numerical method of nonlinear regression with constraints on parameters to avoid unrealistic decisions; in cases where numerical optimisation did not match, stable heuristic initial approximations were used, providing a smooth monotonic curve within the studied concentration range.

Based on the fit of the sigmoidal model, the characteristic concentrations of CD_{50} and ID_{50} were determined. The concentration of CD_{50} was determined as the solution of the equation

$$f_{cyto}(x) = 0.5 \quad (3)$$

that is, the concentration at which the relative viability of cells is 50 % of the control. Similarly, the concentration of ID_{50} was defined as the solution

$$f_{virus}(x) = 0.5 \quad (4)$$

corresponding to a 50 percent level of residual virus activity. For a given four parameters (*a*, *b*, *c*, *d*), the analytical expression for such a concentration was obtained from the equation x^*

$$y_{\text{target}} = \frac{a}{1+e^{(-bx^*+c)}} + d \quad (5)$$

by algebraic transformation:

$$y_{\text{target}} - d = \frac{a}{1+e^{(-bx^*+c)}}, \quad \frac{a}{y_{\text{target}} - d} - 1 = e^{(-bx^*+c)}; \quad (6)$$

$$-bx^* + c = \ln\left(\frac{a}{y_{\text{target}} - d} - 1\right), \quad x^* = \frac{c - \ln\left(\frac{a}{y_{\text{target}} - d} - 1\right)}{b}. \quad (7)$$

In cases where the expression under the logarithm was incorrect (negative or zero) or the parameter *b* was close to zero, the value of CD_{50} or ID_{50} was considered uncertain (no intersection with the level of 50 % in the studied range).

The chemotherapeutic index for each combination "compound – time – treatment regimen" was calculated according to the standard ratio

$$\text{CTI} = \frac{CD_{50}}{ID_{50}} \quad (8)$$

which is interpreted as a safety margin: the larger the CTI, the wider the therapeutic interval between cytotoxic and antiviral concentrations. For further classification analysis, CTI was converted to a binary trait by threshold: the value of $\theta = 4{,}0$ class 1 denoted combinations with CTI ≥ 4, and class 0 – CTI < 4, which made it possible to interpret the problem as a two-class problem of "promising / unpromising" candidates.

To investigate the relationship between the docking profile of compounds, cytotoxicity parameters and the probability of obtaining a high CTI, the decision trees method of the CART (Classification and Regression Trees) type was used. In the first model, the decision tree described the probability of obtaining a determined CD_{50} based on docking indicators. The trait vector included energy parameters of interaction with different regions of the spike protein and the main protease (SP_1 – SP_5, MP_1 – MP_3), as well as a coded timestamp of cell exposure (time_class, where 0 corresponded to 24 hours, 1 to 48 hours). The target variable class_CD_{50} took a value of 1 if CD_{50} was defined for the corresponding compound-time combination, and 0 in the opposite case. Thus, the first model evaluated which docking profiles are associated with the presence of a correct dose-appropriate cytotoxicity curve.

In the second model, the decision tree modeled the dependence of the "connection-time-mode" combination belonging to the CTI class ≥ 4 on the combination of docking characteristics, CD_{50} and ID_{50} parameters, and the treatment regimen. In addition to SP_1 – SP_5, MP_1 – MP_3 and time_class, the numerical values of CD_{50}, ID_{50}, CTI itself, as well as the encoded trait treatment_type_class (0 for mode L and 1 for LP ≥ class_CTI) were added to the trait vector. Both models were built as binary trees with a Gini index division criterion that minimises class heterogeneity in nodes.

Decision trees were trained according to the scheme of dividing the sample into training and test subsamples in the ratio of 70 % / 30 % with a fixed random number generator to ensure reproducibility. In the presence of both classes, a stratified division was carried out to preserve the proportions of the classes in the training and test parts. The depth of the trees was limited to a predetermined maximum to avoid overtraining, and the number of leaf nodes and the structure of the resulting rules were analysed to control the complexity of the model. The text representation of the tree in the form of nested "if" rules was obtained by traversing the structure of the tree, where each inner node specifies a condition of the form "sign ≤ threshold", and the leaf node – belonging to class 0 or 1.

Assessment of the quality of classification models was carried out on test subsamples using a set of standard metrics. Accuracy was defined as the proportion of correctly classified examples:

$$Accuracy = \frac{TP+TN}{TP+TN+FP+FN} \quad (9)$$

where TP (true positives) is the number of true positive classifications, TN (true negatives) is true negative, FP (false positives) is false positive, FN (false negatives) is false negative. Sensitivity (or recall for a positive class) was defined as

$$Sensitivity = \frac{TP}{TP+FN} \quad (10)$$

which reflects the model's ability to detect positive cases. Specificity was calculated as

$$Specificity = \frac{TN}{TN+FP} \quad (11)$$

characterising the ability of the model to correctly cut off negative cases. To assess the balance between sensitivity and accuracy of positive classifications, the F1 measure was used:

$$\text{Precision} = \frac{TP}{TP+FP}, \quad \text{F1} = \frac{2 \cdot \text{Precision} \cdot Sensitivity}{\text{Precision} + Sensitivity}. \quad (12)$$

In the case of probabilistic model outputs (predict_proba), the area under the ROC curve (ROC-AUC) was additionally calculated, which characterises the trade-off between sensitivity and specificity when varying the classification threshold. In cases where all observations belonged to the same class and the ROC curve was incorrectly determined, the ROC-AUC was not interpreted.

Additionally, two complementary procedures were used to analyse the contribution of individual traits. First, standard estimates of the importance of traits in the tree were used based on a decrease in the Gini criterion when splitting according to the corresponding trait. Secondly, the sensitivity analysis of the "drop-one-feature" sensitivity was performed: for each feature, a new decision tree was built without this feature in the feature vector, and then the model metrics were compared with the base variant. A significant degradation of sensitivity or specificity in the exclusion of a certain trait was interpreted as an indicator of its critical importance for decision-making.

To formalise the sequence of decision-making on the continuation or termination of laboratory tests at different stages (docking, assessment of cytotoxicity, testing of antiviral activity), the Markov Decision Process (MDP) was used. The state space described the main stages of the study: post-docking baseline (S_0), post-doc status (S_1), post-antiviral activity (S_2), post-doctrinal status, and two absorption states – success ($S_{success}$, candidate acquisition with CTI ≥ 4) and completion without success (S_{fail}). In each of the non-absorption states, two actions were considered: "stop" – stop further experiments, and "continue" – move to the next stage of the study.

Transitions between states were described by probabilities that were estimated on the basis of empirical frequencies in the population of the compounds studied. For example, the probability of transition from $SP(s'|s,a)_0$ to S_1 under the action "continue" was estimated as the proportion of compounds for which CD_{50} could be determined; the probability of transition from S_1 to S_2 as the proportion of combinations for which CTI was determined; the probability of transition from S_2 to $S_{success}$ as the proportion of cases with CTI ≥ 4 among those who have passed to the stage of antiviral activity tests. The reward system $R(s, a)$ included negative contributions in the form of docking costs, cytotoxicity and antiviral activity tests, as well as a positive reward for achieving a state of $S_{success}$ corresponding to obtaining a promising candidate. To assess the long-term usefulness of action policies, a discount factor $\gamma \in (0;1)$ was used, which takes into account the decrease in the "value" of time-distant results.

The optimal policy that maximizes the expected discounted total reward was determined by the value iteration method. At each iteration, the value of the utility function $\pi^*(s)V(s)$ was updated according to the rule

$$V_{k+1}(s) = \max\left[R(s,a) + \gamma \sum_{s,a} P(s' \mid s,a) V_k(s')\right] \quad (13)$$

until the changes in $V(s)$ for all states become less than the predetermined error. The choice of action in state s was carried out as an argument to the maximum on the right side of the Bellman equation.

Interpretation of the supplementary experiments as sources of information about the probability of success and the associated costs allowed us to integrate the concept of information value analysis into the Markov formulation. The total expected value of perfect information (EVPI) is the difference between the expected utility from having complete, error-free information about the outcome (e.g., CTI for each compound before the experiments were performed) and the expected utility at the current level of uncertainty. The expected value of partial perfect information about a subset of parameters (EVPPI) marks a similar difference, but only for information about a particular block of parameters (for example, only about CD_{50} or only about ID_{50}). The expected value of sample information (EVSI) determines the increase in expected utility obtained by making additional, but not error-free measurements (for example, additional experiments on cytotoxicity

or antiviral activity). In mathematical formulation, these indicators are calculated as the difference between the maximum expected utility according to the refined probability distribution (after taking into account the new data) and the maximum according to the original distribution; within the framework of MDP, it comes down to comparing the values of $V(s)$ under different assumptions about the information state of the system.

Formally, let θ denote the vector of uncertain parameters (e.g., transition probabilities and success rates), d a decision or policy, and $U(d, \theta)$ the total discounted utility under this decision. The baseline expected value at the initial state s_0 is

$$V_{base}(s_0) = \max_{d \in D} E_\theta[U(d,\theta) \mid I_0] \quad (14)$$

where I_0 denotes the current information set. The expected value of perfect information (EVPI) is defined as

$$\text{EVPI} = E_\theta[\max_{d \in D} E_\theta[U(d,\theta) \mid I_0] - V_{base}(s_0). \quad (15)$$

It quantifies the maximum gain in expected utility that could be achieved if θ were known without uncertainty before any decision is made.

For a subset of parameters $\varphi \subset \theta$ (for example, only cytotoxicity or only antiviral activity parameters), the expected value of partial perfect information (EVPPI) is given by

$$EVPPI(\varphi) = E_\varphi \times$$

$$\times[\max_{d \in D} E_\theta[U(d,\theta) \mid I_0]] - V_{base}(s_0). \quad (16)$$

Here, only the subset φ is assumed to be known perfectly, whereas the remaining parameters θ\φ remain uncertain.

The expected value of sample information (EVSI) associated with a realistic additional experiment y is defined as

$$\text{EVSI}(y) = E_y[\max_{d \in D} E_\theta[U(d,\theta) \mid I_0]] -$$

$$- V_{base}(s_0) - C(y) \quad (17)$$

where y denotes the possible outcomes of the new experiment, and $C(y)$ is the cost of collecting this information. Within the MDP formulation used in this work, all three quantities can be evaluated as differences between optimal state values $V(s_0)$ computed under different information scenarios (baseline information, perfect information on θ or φ, and posterior distributions updated by sample data y).

This approach provides a holistic methodological framework: sigmoidal dose-response modelling allows for stable estimates of CD_{50}, ID_{50}, and CTI; decision trees formalise the logic of the selection of compounds according to the profiles of docking, cytotoxicity and antiviral activity; The Markov model with associated information value metrics allows you to assess the feasibility of continuing or stopping experiments at different stages, taking into account costs and the likelihood of achieving chemotherapy success.

The study used a holistic experimental dataset which covered seven test samples (T1 – T7), each having obtained both in silico and in vitro characteristics. The generalised structure of this set is provided in Table 1.

Results of molecular docking to the spike protein and the main protease of the virus are available for each sample and presented in the form of binding energy ranges. In particular, for the spike protein, the minimum and maximum values of the docking energy for a set of domains (SP_1 – SP_5) were taken into account, and for the main protease – the minimum and maxi-

***Table* 1.** Generalised characteristics of the experimental dataset

Test Sample	Min. Docking energy (spike protein), kcal/mol	Max. Docking energy (spike protein), kcal/mol	Min. Docking energy (basic protease), kcal/mol	Max. Docking energy (basic protease), kcal/mol	Summarised CTI in 24 hours	Summarised CTI in 48 hours	Cytotoxicity data (24/48 hours)	Antiviral activity data (L, LP; 24/48 hours)
T1	–6.26	–2.26	–5.68	–4.04	24	16	yes	yes
T2	–6.32	–3.3	–7.34	–4.07	–	4	yes	yes
T3	–5.24	–2.4	–7.12	–4.04	3	2	yes	yes
T4	–5.74	–2.26	–7.34	–4.04	–	–	yes	yes
T5	–4.96	–2.37	–7.34	–4.04	4	3	yes	yes
T6	–6.26	–2.4	–7.34	–4.04	6	6	yes	yes
T7	–5.64	–2.26	–7.34	–4.21	–	–	yes	yes

mum values of the interaction energy with individual functional regions (MP_1 – MP_3). Table 1 shows two aggregate intervals for each test sample: minimum and maximum docking energy for the spike protein and major protease, reflecting the spectrum of possible binding configurations within the docking protocols used.

Results

The results obtained demonstrate a consistent chain of transition from in silico characteristics to integral assessment of the chemotherapeutic index and optimisation of the sequence of experiments. First of all, the analysis of the initial CD_{50}, ID_{50} and CTI values for seven test samples showed significant inter-sample variability: for some of the sample-time-mode combinations, CD_{50} or ID_{50} could not be correctly estimated at all within the studied concentration range (the curve did not cross the 50 % level), while others showed well-defined half-inhibition points and high CTI values. It is important to note that this variability turned out to be structured – it is related to the profile of the docking to the main protease and to the exposure mode, and is not random noise; This is confirmed by the construction of the first decision tree and the Markov model.

In the "docking → cytotoxicity" model, the decision tree gives a compact but meaningful structure (Fig. 1).

The root node separates all observations by the MP_2 parameter, which characterises the binding energy of compounds to one of the functional areas of the main protease. If MP_2 is found to be above the threshold value of approximately – 7.0 kcal/mol (i.e., binding is weaker), the model, without further branching, assigns the corresponding sample-time combination to a class for which CD_{50} is not determined: all cases where the dose-response of cytotoxicity remains flat or monotonically low are concentrated in this leaf node. Instead, for compounds with a more favourable MP_2 value (≤–7.0 kcal/mol), the tree moves on to the second critical parameter – MP_1. For MP_1 values ≤–5.97 kcal/mol, all examples fall into the sheet with the class "has CD_{50}", i.e. a sufficiently strong interaction with two regions of the main protease is a reliable predictor of the presence of correctly defined CD_{50}. In the intermediate zone, where MP_2 still indicates a fairly strong binding, but MP_1 is already closer to the threshold, the model additionally takes into account the incubation time: for 24 h, some of the combinations remain in the class without a defined CD_{50}, while at 48 h the tree leans towards a class with a defined CD_{50}. Thus, exposure time acts as a secondary, modulating factor that can compensate for the insufficient "force" of docking, but only in a narrow sub-range of MP_1 and MP_2 values. On the test sample, this model demonstrates classification performance with all metrics equal to 1.0, indicating that the hierarchical combination of MP_2, MP_1, and incubation time provides deterministic rules for predicting CD_{50} availability. Trait weights and analysis of the exclusion of individual predictors confirm the dominance of MP_2 and MP_1 parameters: they provide the main contribution to the reduction of the Gini index, while the time factor affects the quality of classification much weaker.

The results for the "cytotoxicity → CTI ≥ 4.0" model turned out to be fundamentally different and highlighted the structural features of the existing dataset. Applying the decision tree to an extended trait vector that included docking scores, CD_{50} numerical values, ID_{50}, CTI itself, encoded treatment time and regimen, resulted in a moderately complex tree structure (Fig. 2).

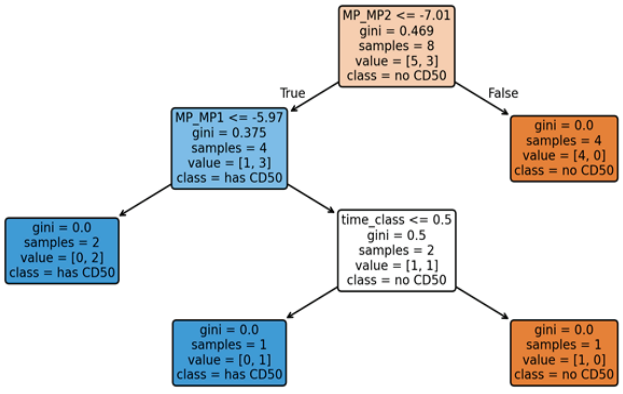

Fig. 1. Decision tree for the transition "docking → cytotoxicity" using the parameters of interaction with the main protease (MP_1, MP_2) and exposure time (24/48 hours) as predictors of the presence of correctly determined CD_{50}

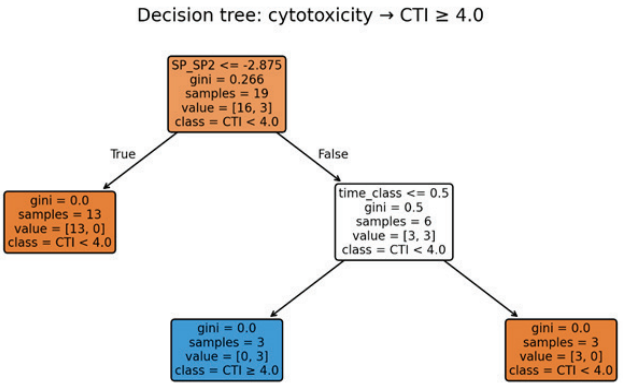

Fig. 2. Decision tree for the transition "cytotoxicity → CTI ≥ 4.0"

Unlike the first model, this tree exhibits branching that attempts to separate compounds achieving CTI ≥ 4.0 from those with lower therapeutic indices. However, the classification performance reflects the challenging nature of this prediction task. The model achieved an overall accuracy of 0.89, indicating that 89 % of test cases were correctly classified. Notably, sensitivity was substantially lower at 0.50, meaning that only half of the compounds that actually achieved CTI ≥ 4.0 were correctly identified by the model. In contrast, perfect specificity at 1.00 indicates that all compounds predicted to have CTI < 4.0 were indeed below this threshold – the model made no false positive predictions. This imbalance between precision and recall is reflected in the F1-score of 0.67, while the ROC-AUC of 0.75 suggests moderate discriminative ability.

This performance pattern reveals an important characteristic of the current model: it adopts a highly conservative strategy and predicts high CTI rarely unless multiple favourable conditions are met. Although this approach does eliminate false optimism, it often results in missed opportunities, as approximately half of promising compounds are not identified. The Markov model of the sequence of experiments made it possible to quantify how expedient it is to continue the study at each stage, taking into account the costs and probability of obtaining at least one candidate with a CTI ≥ 4.0. For states S_0 (after docking), S_1 (after assessment of cytotoxicity), and S_2 (after assessment of antiviral activity), values of the utility function $V(s)$ were calculated, which increase from about 9.7 for S_0 to 22.5 for S_1 and 84.0 for S_2 as shown in Table 2.

***Table* 2.** The value of the utility function $V(s)$ for Markov model states and the optimal policy $\pi^*(s)$

	S_0	S_1	S_2	$S_{success}$	S_{fail}
$V(S_i)$	9.688	22.5	84	0	0
$\pi(S_i)$	continue	continue	continue	stop	stop

Such monotonous growth means that each subsequent block of experiments significantly increases the expected "cost" of the candidate portfolio: at the docking stage, information about the potential of compounds is still very uncertain; obtaining CD_{50} adds an important layer of safety assessment and cuts off clearly toxic variants; completion of antiviral activity tests virtually determines whether a portfolio has a chance of containing at least one drug with an acceptable CTI. The calculated optimal policy of π^*(s) turned out to be unambiguous: for all three non-absorption states, the action "continue experiments" is recommended, while in the absorption states of success or failure – "stop". On the one hand, this is consistent with the high CTI values among the samples that have passed the previous filters: the projected benefit from the complete passage of all stages exceeds the total costs. On the other hand, such a policy indicates that the structure of the experimental program does not currently contain "redundant" stages: each of them significantly changes the expected utility, and therefore makes a non-trivial contribution to reducing uncertainty about CTI.

Interpreting these results in terms of information value shows that the greatest gain in utility is given by the transition from a post-cytotoxicity state to a post-antiviral state. This means that it is the ID_{50} results and the associated CTI values that are key to the final decision on the feasibility of promoting the compound; information about the docking profile and CD_{50} plays mainly the role of a pre-filter. The tree "docking → cytotoxicity" clearly shows that already at the stage of in silico evaluation, a combination of MP_2 and MP_1 parameters can be distinguished, which, with a high probability, leads to the formation of a correct CD_{50} curve. Further, the Markov model demonstrates that, despite the costs, continuing the studies to the stage of antiviral activity is economically justified, since the expected gain from the potential detection of at least one candidate with a high CTI significantly exceeds the alternative of "stopping" in the early stages. At the same time, the moderate performance of the tree "cytotoxicity → CTI ≥ 4.0" (Table 3) signals that in the current dataset, predicting final therapeutic success from intermediate parameters remains challenging. While the model's high specificity ensures that no unpromising compounds are incorrectly advanced, its lower sensitivity indicates that approximately half of actually promising candidates are not recognised by the current decision rules, suggesting that more sophisticated stratification approaches or additional predictive features may be needed to improve early identification of therapeutic candidates.

Numerical evaluation of the information-value metrics within the MDP formulation yielded an expected value of perfect information (EVPI) equal to zero, as well as a zero partial value of perfect information (EVPPI) for the antiviral stage, while the expected value of sample information (EVSI) for an additional antiviral experiment was negative and equal to −10 in the adopted arbitrary utility units. This pattern indicates that, under the current estimates of transition probabilities and reward structure, even hypothetically perfect knowledge of the

***Table* 3.** Comparative metrics of decision tree models and Markov model

Model	Positive class	Accuracy	Sensitivity (Recall)	Specificity	F1-score	ROC-AUC
Docking → CD_{50} (presence of CD_{50} defined)	has CD_{50}	1	1	1	1	1
Cytotoxicity → CTI ≥ 4.0	CTI ≥ 4.0	0.89	0.50	1.00	0.67	0.75

antiviral success probability would not change either the optimal policy or the expected value at the initial state, so that additional information of this type has no incremental decision value. At the same time, the negative EVSI reflects the fact that, in the simplified scenario considered, a realistic extra experiment on antiviral activity does not lead to a sufficient increase in the expected utility to compensate for its cost, implying that resources would be more efficiently allocated to adjusting earlier-stage selection criteria or expanding the candidate set rather than intensifying measurements at the final antiviral stage.

The comparative values of classification metrics for both decision trees, as well as the utility functions of the states of the Markov model, are summarised in Table 3, allow you to quantitatively compare the accuracy of predictive decisions and the expected effectiveness of various strategies for conducting experiments.

Collectively, this indicates that further experimental studies should be directed either to expand the sample set (to include more examples with intermediate and low CTIs) or to clarify dosing regimens and time regimens, where the gap between efficacy and toxicity will be less obvious and, accordingly, will provide a richer structure for building more complex but informative decision trees.

Conclusions

This research shows that decision trees and Markov decision processes are used for complementary aspects in preclinical antiviral research optimisation, and their performance is fundamentally shaped by the structure of the available data. The decision-tree model linking docking parameters to the presence of a well-defined CD_{50} achieved classification success on the test set, with all metrics equal to 1.0. This indicates that strong binding to the main protease, in particular, favourable values of MP_1 and MP_2 combined with incubation time provides deterministic rules for predicting the formation of a stable dose-response curve. While these results imply robust predictive ability within the current dataset, the limited sample size requires validation on larger, more diverse compound libraries in order to confirm generalizability.

In contrast, the tree built for the transition from cytotoxicity parameters to CTI ≥ 4.0 exhibited substantially different performance characteristics. The model achieved 89 % overall accuracy but demonstrated an asymmetric error profile: sensitivity of only 0.50 (correctly identifying half of compounds with CTI ≥ 4.0) combined with specificity of 1.00 (no false positives). This classification strategy ensures that compounds predicted to achieve high CTI are indeed therapeutically promising. Still, it results in missed opportunities, as approximately half of actually promising candidates are not recognised by the current decision rules. The F1-score of 0.67 and ROC-AUC of 0.75 show that the relationship between intermediate experimental parameters and final therapeutic success is more complex than can be captured by simple threshold-based rules with the current feature set and sample size.

The Markov decision process provided a global, quantitatively interpretable view of the same experimental pipeline, explicitly integrating transition probabilities, experimental costs and the probability of achieving at least one candidate with CTI ≥ 4.0. The estimated state values $V(S_0)$, $V(S_1)$ and $V(S_2)$ increased monotonically during the stage "after docking → after cytotoxicity → after antiviral testing", confirming that each successive block of experiments substantially raises the expected utility of the candidate portfolio. The optimal policy consistently recommended the continuation of the preclinical program from docking through cytotoxicity to antiviral assays, and that the stop is required only in the absorbing states of success or failure. Despite the second decision tree performing the imperfect classification, the Markov model still indicated that, under the assumed costs and probabilities of success, the full three-stage pipeline is an economically justified solution and does not contain redundant experimental steps.

The value of information analysis shows how much each stage of the pipeline contributes to reducing uncertainty and improving decision quality. The results suggest that the largest incremental gain in

expected utility appears when the compound moves from the state after cytotoxicity assessment to the state after antiviral activity testing. This highlights the decisive role of ID_{50} and derived CTI values in confirming or rejecting candidates. Information on docking and CD_{50} acts primarily as a preliminary filter that shapes the distribution of outcomes that are observed at later stages. Decision trees are most effective as local, interpretable tools for formalising the cut-off rules based on docking and toxicity profiles at the early stages, whereas the Markov model outperforms them in terms of providing a globally optimal, cost-aware strategy for navigating the entire preclinical pipeline. Together, these results show that further development should focus on expanding and rebalancing the experimental dataset (to enable more informative tree-based models at the CTI level) and on refining Markov and value of information formulations to incorporate richer biological and economic parameters in the optimisation of antiviral preclinical programs.

References

[1] U.E. Ogbonna *et al.*, "Advances in machine learning for optimizing pharmaceutical drug discovery", *Curr. Proteomics*, Vol. 22, no. 2, p. 100015, Apr. 2025. Retrieved from doi: https://doi.org/10.1016/j.curpro.2025.100015

[2] A. Gangwal and A. Lavecchia, "Artificial intelligence in preclinical research: enhancing digital twins and organ-on-chip to reduce animal testing", *Drug Discov. Today*, Vol. 30, no. 5, p. 104360, May 2025. Retrieved from doi: https://doi.org/10.1016/j.drudis.2025.104360

[3] M. Mashhadi Abolghasem Shirazi *et al.*, "Next-generation antiviral peptides: AI-driven design, translational delivery platforms, and future therapeutic directions", *Virus Res.*, Vol. 361, p. 199642, Nov. 2025. Retrieved from doi: https://doi.org/ 10.1016/j.virusres.2025.199642

[4] A. Luganini *et al.*, "DHODH inhibitors: What will it take to get them into the clinic as antivirals?", *Antiviral Res.*, Vol. 236, p. 106099, Apr. 2025. Retrieved from doi: https://doi.org/10.1016/j.antiviral.2025.106099

[5] N. Vora *et al.*, "Artificial intelligence and multi-omics in drug discovery: A deep learning-powered revolution", *Cure Care*, p. 100011, Nov. 2025. Retrieved from doi: https://doi.org/10.1016/j.ccwv.2025.100011

[6] K.O. Oyediran *et al.*, "Artificial intelligence in human immunodeficiency virus mutation prediction and drug design: Advancing personalized treatment and prevention", *Pharm. Sci. Adv.*, Vol. 3, p. 100080, Dec. 2025. Retrieved from doi: https://doi.org/10.1016/j.pscia.2025.100080

[7] A. Gangwal and A. Lavecchia, "Artificial Intelligence in Natural Product Drug Discovery: Current Applications and Future Perspectives", *J. Med. Chem.*, Vol. 68, no. 4, pp. 3948–3969, Feb. 2025. Retrieved from doi: https://doi.org/10.1021/acs.jmedchem.4c01257

Д.С. Городецький, М.П. Сметюх, С.О. Соловйов

ПРИЙНЯТТЯ РІШЕНЬ У ПРОЦЕСІ ДОКЛІНІЧНОЇ РОЗРОБКИ ПРОТИВІРУСНИХ ПРЕПАРАТІВ ПРОТИ КОРОНАВІРУСУ: МАТЕМАТИЧНЕ МОДЕЛЮВАННЯ ТА АНАЛІЗ ЦІННОСТІ ІНФОРМАЦІЇ

Проблематика. Доклінічне оцінювання кандидатів як противірусних препаратів – це багатоетапний процес, який супроводжується значною невизначеністю і потребує формальних інструментів підтримки прийняття рішень. Традиційні підходи до скринінгу сполук зазвичай не містять структурованих методів оптимізації для послідовного вибору, а також оцінювання доцільності й ризиків переходів між етапами. Це призводить до неефективності під час відбору перспективних молекул і підвищує ймовірність вибору субоптимальних дослідницьких траєкторій.

Мета дослідження. Розробити й обґрунтувати формалізований підхід, щоб оптимізувати переходи між етапами доклінічного тестування противірусних препаратів. Цей підхід інтегрує дерева рішень і марковську модель для оцінювання ефективності, ризиків і цінності додаткової інформації, що забезпечить раціональне планування послідовності доклінічних досліджень.

Методика реалізації. Експериментальні дані з молекулярного докінгу, цитотоксичності CD_{50} та антивірусної активності IC_{50} були інтегровані в каскадну систему оцінювання із критерієм переходу XTI ≥ 4. Дерева рішень забезпечили інтерпретовані правила просування сполук, а за допомогою марковської моделі було змодельовано послідовні стратегії в умовах невизначеності та оцінено доцільність переходів між етапами. За допомогою аналізу цінності інформації було оцінено очікувану користь додаткових експериментальних даних.

Результати дослідження. Описаний підхід дав узгоджені технічні результати. Дерево рішень для прогнозування CTI ≥ 4,0 показало консервативний шаблон класифікації, правильно визначаючи сполуки з високим терапевтичним потенціалом, але пропускаючи частину ефективних кандидатів. Марковська модель допомогла оцінити стан системи на етапах докінгу, цитотоксичності й антивірусного тестування, що показало зростання очікуваної корисності. Ґрунтуючись на отриманих результатах, було визначено оптимальні рішення щодо продовження досліджень до антивірусних тестів, тоді як за допомогою аналізу цінності інформації було встановлено, що найбільший приріст очікуваної корисності досягають після тестування антивірусної активності, коли ранні етапи виконують роль фільтрів.

Висновки. Дослідження показує, що дерева рішень і марковські моделі відображають різні, але взаємодоповнювальні аспекти доклінічного оцінювання. Дерева рішень допомагають структурувати правила на ранніх етапах дослідження, показуючи, як етапи докінгу та цитотоксичності впливають на просування сполук. Водночас їх обмежена чутливість підкреслює складність передбачення кінцевого противірусного успіху на основі проміжних показників. Марковський процес дає ширший погляд на послідовність експериментів і демонструє виправданість вибору повного трирівневого дослідження та впливу невизначеності й витрат на рішення щодо прогресії сполук. Результати аналізу цінності інформації уточнюють важливість кожного етапу, підкреслюючи ключову роль даних про антивірусну активність. Разом ці результати показують важливість впровадження методів прийняття рішень для підвищення структури, прозорості та ефективності доклінічних досліджень противірусних препаратів.

Ключові слова: коронавірус; препарат; доклінічне оцінювання; дерево рішень; марковський процес прийняття рішень; цінність інформації.

Рекомендована Радою
факультету прикладної математики
КПІ ім. Ігоря Сікорського

Надійшла до редакції
18 жовтня 2025 року

Прийнята до публікації
15 грудня 2025 року

СИСТЕМНИЙ АНАЛІЗ ТА НАУКА ПРО ДАНІ

DOI: https://doi.org/10.20535/kpisn.2025.4.343202
UDC 004.85.032.26:004.93'1:616(045)

О.О. Зарицький[1*], В.Я. Данилов[1]
[1]КПІ ім. Ігоря Сікорського, Київ, Україна
[*]Відповідальний автор: zaritskiy.alexey@gmail.com

МЕТОД ФРАКТАЛЬНО-КЕРОВАНОЇ РЕГУЛЯРИЗАЦІЇ АВТОЕНКОДЕРІВ ДЛЯ НАПІВКЕРОВАНОГО НАВЧАННЯ В ЗАДАЧАХ КЛАСИФІКАЦІЇ МЕДИЧНИХ ЗОБРАЖЕНЬ

Проблематика. Класифікація медичних зображень за допомогою глибокого навчання є критично важливою задачею, однак її ефективність обмежується дефіцитом розмічених даних, збір яких є дорогим. Методи напівкерованого навчання (НН) вирішують цю проблему, залучаючи нерозмічені дані. Поширені підходи, що ґрунтуються на автоенкодерах (АЕ), використовують реконструкцію як навчальний сигнал. Утім, стандартна мінімізація втрат реконструкції не гарантує, що отриманий латентний простір буде оптимально структурований для вирішення завдання класифікації, оскільки модель може фокусуватися на нерелевантних для діагностики ознаках.
Мета дослідження. Розробка та експериментальна перевірка нового методу регуляризації латентного простору – фрактально-керованої регуляризації (FDR). Мета полягає у покращенні метричних показників класифікації медичних зображень в умовах гострого дефіциту розмічених даних (5 %) за допомогою інтеграції фрактальної розмірності (ФР) як додаткового, апріорного навчального сигналу.
Методика реалізації. Запропонована модель FDR-AE ґрунтується на архітектурі АЕ, доповненій двома повнозв'язними шарами, що приєднані до латентного простору: класифікаційним та регресійним. Регресійний шар навчається прогнозувати ФР вхідного зображення, обчислену заздалегідь методом «box-counting». Загальна функція втрат є комбінацією трьох компонент: втрат класифікації на 5 % розмічених даних і втрат реконструкції та фрактальної регресії на 100 % даних. Ефективність методу перевірено на трьох наборах даних різної модальності (ISIC2024, COVID-19 Radiology, Brain Tumor MRI) порівняно з базовою згортковою мережею Base-CNN і стандартним напівкерованим АЕ SSL-AE.
Результати дослідження. Експерименти показали стабільну перевагу запропонованого методу. На датасеті ISIC2024 модель FDR-AE досягла F1-Score 0.508 для класу «malignant» проти 0.431 у SSL-AE та 0.304 у Base-CNN. На датасеті COVID-19, F1-Score для класу «covid19» склав 0.722 для FDR-AE проти 0.695 для SSL-AE. У 4-класовій задачі Brain Tumor модель FDR-AE продемонструвала покращення F1-Score щодо всіх класів, причому найбільший приріст +0.079 та +0.054, відповідно, спостерігався для класів 0 та 3, що мали найбільшу взаємну статистичну відмінність у ФР.
Висновки. Фрактально-керована регуляризація доводить, що ФР є цінним апріорним сигналом для навчання більш якісних і структурно обґрунтованих представлень у задачах НН. Метод особливо ефективний на простих архітектурах в умовах сильного дефіциту даних. Перспективи подальших досліджень включають використання FDR як методу попереднього навчання (pre-training) або впровадження динамічного коефіцієнта для регресійного компонента функції втрат.
Ключові слова: напівкероване навчання; фрактальна розмірність; автоенкодер; регуляризація латентного простору; медичні зображення; класифікація зображень; box-counting.

Вступ

Автоматизований аналіз медичних зображень на основі глибоких нейронних мереж є важливим напрямом досліджень, оскільки може допомогти у ранній діагностиці патологій. Однією з основних проблем у впровадженні таких систем є дефіцит розмічених даних, отримання й розмітка яких вимагає висококваліфікованих спеціалістів і суттєвих витрат грошей і часу.

Пропозиція для цитування цієї статті: О.О. Зарицький, В.Я. Данилов, "Метод фрактально-керованої регуляризації автоенкодерів для напівкерованого навчання в задачах класифікації медичних зображень", *Наукові вісті КПІ*, № 4, с. 31–39, 2025. doi: https://doi.org/10.20535/kpisn.2025.4.343202

Offer a citation for this article: O.O. Zarytskyi, V.Y. Danilov, "A method for fractal-driven regularization of autoencoders in semi-supervised medical image classification", *KPI Science News*, no. 4, pp. 31–39, 2025. doi: https://doi.org/10.20535/kpisn.2025.4.343202

Для вирішення цієї проблеми активно розвиваються методи НН, що дають можливість використовувати одночасно розмічені й нерозмічені дані для навчання моделей.

Поширеним підходом у НН є використання АЕ, які вивчають корисні ознаки через задачу реконструкції вхідних зображень. Такий підхід довів свою ефективність у таких методах, як Adversarial Autoencoders та Ladder Networks. Утім, стандартна мінімізація втрат реконструкції не гарантує, що латентний простір моделі буде оптимально структурованим для вирішення завдання класифікації. Наше припущення ґрунтується на тому, що його можна покращити, використовуючи апріорні знання про структуру і складність даних, на яких навчається модель.

Постановка задачі

Метою цієї роботи є розробка та експериментальна перевірка нового методу НН – FDR. Ми пропонуємо використовувати ФР як додатковий навчальний сигнал для покращення якості латентного простору в задачах НН. Ефективність методу продемонстровано на трьох медичних датасетах в умовах гострого дефіциту розмічених даних (5 % вибірки), де запропонована модель АЕ із фрактальною регуляризацією FDR-AE порівнюється з базовою керованою моделлю Base-CNN і стандартним напівкерованим AE SSL-AE.

Фрактальна розмірність як класифікаційна ознака у медичних зображеннях

Виділення інформативних ознак, що описують складні біологічні структури, є ключовою проблемою під час аналізу медичних зображень. Фрактальна розмірність – це числовий показник, що оцінює структурну складність і нерегулярність об'єкта. Цей показник широко використовують як ключову ознаку в багатьох медичних дослідженнях, оскільки доведено, що ФР корелює з діагностичними станами [1–5]. Наприклад, у нейроонкології ФР корелює з показником агресивності гліобластом [3], а в мамографії доведено чітку кореляцію між злоякісністю утворення та його ФР [5]. Утім, у більшості досліджень ФР використовують як основну ознаку для аналізу. Відповідно, якщо статистичні розподіли значень ФР суттєво накладаються один на одного, – використання цього показника як основного сигналу для класифікації є неможливим. У цьому дослідженні ми пропонуємо метод використання ФР як сигналу для НН (фрактальна регуляризація латентного простору мережі) і покажемо, що навіть в разі суттєвого накладання статистичних розподілів ця ознака може суттєво покращувати якість моделі.

Вибір та адаптація методу обчислення фрактальної розмірності

Є багато методів обчислення ФР зображень, що адаптовані під різні задачі та структуру самих зображень, зокрема основані на базовому методі box-counting [6–9], морфології об'єкта [10] чи навіть Фур'є-спектра [11–12]. Для цього дослідження було обрано один із найбільш поширених методів визначення ФР: box-counting. Він полягає у накладанні на зображення сіток з різними розмірами комірок r та підрахунку кількості комірок N_r, що містять пікселі вимірюваного об'єкта. Фрактальну розмірність D_{box} вимірюють як нахил прямої графіка залежності N_r від 1/r:

$$D_{box} = \lim_{r \to 0} \frac{\log(N_r)}{\log(\frac{1}{r})}.$$

На практиці вищезгаданий нахил графіка найчастіше вимірюють за допомогою лінійної регресії [9]. Вибір цього методу був зумовлений простотою обчислення. Також було експериментально визначено, що у розглянутих нами наборах даних значення ФР, підраховані цим методом, мають найбільшу різницю у середніх значеннях для різних класів. Наприклад, для набору даних ISIC2024 (див. «Опис наборів даних») box-counting показав $\Delta Mean = 0.149$, тоді як найближчий за цим показником метод Minkovsky-Bouligand [10] показав різницю всього у 0.084.

Стандартний метод підрахунку N_r вимагає бінаризованого зображення. Це є проблемою для медичних зображень, оскільки діагностично важливою є інформація, що може міститися у відтінках сірого. Для вирішення цієї проблеми у нашій роботі ми використовуємо адаптивну бінаризацію замість фіксованого порогу. Для кожного зображення пороговим значенням буде середнє (mean) по зображенню.

Статистичне обґрунтування фрактальної регуляризації

Основною гіпотезою запропонованого методу є те, що обчислена ФР може слугувати ефективним джерелом «слабкого» сигналу для регуляризації латентного простору мережі. Для цього

потрібно, щоб середні значення ФР різнилися для різних класів. При цьому перевагою використання сигналу саме як регуляризаційного, а не як основного сигналу, для класифікації полягає в тому, що накладання розподілів ФР не є таким критичним для цієї задачі. Щоб підтвердити вищезгадану гіпотезу, ми провели статистичний аналіз на трьох обраних датасетах, щоб перевірити, чи існує статистично значуща різниця між класами. З результатів дослідження, наведених у табл. 1 та 2, можна побачити, що всі три набори даних мають статистично значущу різницю між класами (детальний опис наборів даних та обґрунтування їх вибору викладено у розд. «Матеріали та методологія досліджень»). Наявність різниці між середніми значеннями вимірів ФР ($\Delta Mean$), а також співвідношення сигнал/шум ($\Delta Mean/\max(\sigma)$), що не близькі до нуля, свідчать про релевантність застосування такої ознаки.

Регуляризація за допомогою фрактальної регуляризації

Запропонований метод полягає у структурній регуляризації латентного простору. Ми вводимо регресійний шар f_{fd}, що приєднується до латентного вектора z і навчається прогнозувати ФР зображення, порівнюючи свої прогнози $f_{fd}(z)$ із значеннями d, визначеними апріорним методом (у нашому випадку box-counting). Формулу для обчислення втрат регресії L_{fd} для батчу розміру N описують таким чином:

$$\hat{d}_i = f_{fd}(z_i);$$

$$L_{fd} = \frac{1}{N}\sum_{i=1}^{N}(\hat{d}_i - d_i)^2,$$

де $\hat{d}_i$ та d_i – прогнозоване та апріорне значення ФР для i-го вектора у батчі, а z_i – латентне представлення i-го вхідного зображення.

Оскільки статистичний аналіз підтвердив, що ФР є релевантною ознакою, її явне кодування у латентному просторі може покращувати його структуру у наступній класифікації.

Щоб запобігти втраті іншої цінної інформації під час регресії ФР, ми застосуємо цей метод як модифікацію архітектури АЕ. Головне завдання АЕ – мінімізація функції втрат реконструкції L_{rec}. Вона гарантує, що вектор z зберігатиме максимум інформації для відновлення зображення. Цю регуляризаційну властивість

***Таблиця* 1.** Статистичний аналіз фрактальної розмірності, підрахованої методом box-counting (датасети із двома класами)

Набір даних	Mean FD (class 0)	Mean FD (class 1)	ΔMean	σ (class 0)	σ (class 1)	ΔMean/ max σ
ISIC2024 Challenge	1.375	1.524	0.149	0.498	0.389	0.299
COVID-19 Radiology Database	1.851	1.828	0.023	0.024	0.023	0.941

***Таблиця* 2.** Статистичний аналіз фрактальної розмірності, підрахованої методом box-counting (датасети з чотирма класами)

Набір даних	Mean FD (class 0)	Mean FD (class 1)	Mean FD (class 2)	Mean FD (class 3)
Brain Tumor MRI Dataset	1.88 518	1.88 538	1.8851	1.87 125
	σ (class 0)	σ (class 1)	σ (class 2)	σ (class 3)
	0.0 188 859	0.0 211 904	0.0 318 129	0.0 140 467

Набір даних	Клас	Клас	$\Delta Mean$	max σ	$\Delta Mean/\max\sigma$
Brain Tumor MRI Dataset	0	1	0.0002	0.0 211 904	0.00 943 824
	0	2	0.00 008	0.0 318 129	0.0 025 147
	0	3	0.01 393	0.0 188 859	0.7 375 873
	1	2	0.00 028	0.0 318 129	0.00 880 146
	1	3	0.01 413	0.0 211 904	0.66 681 139
	2	3	0.01 385	0.0 318 129	0.43 535 798

АЕ широко використовують у НН для навчання на нерозмічених даних, наприклад в adversarial autoencoders [13] та ladder network архітектурі [14]. Таким чином, оптимізація двох вищевказаних функцій втрат діє одночасно як регуляризація повноти інформації (L_{rec}) і як структурна регуляризація (L_{fd}) у латентному просторі.

Для порівняння реконструйованого зображення з оригінальним ми використали MSE (mean squared error). Для навчання на розмічених даних було додано класифікаційний шар, що використовує cross-entropy loss функцію (L_{CE}). Загальну функцію втрат можна описати так:

$$L = L_{CE} + \lambda_{rec} L_{rec} + \lambda_{fd} L_{fd}.$$

Гіперпараметри λ_{rec} та λ_{fd} контролюють внесок некерованого навчання. Оптимізація цієї функції втрат змушує енкодер створювати простір z, що є одночасно повним, структурно чутливим та оптимізованим для класифікації. На рис. 1 зображено модель, що реалізує запропонований метод. Стрілками позначено зв'язки між компонентами моделі, а пунктирними лініями – умовні зв'язки, які демонструють, як обчислюються компоненти функції втрат.

Матеріали і методологія дослідження

Опис наборів даних

Для експериментальної демонстрації ефективності запропонованого методу було обрано три відкриті датасети медичних зображень, що різняться за типом діагностичної задачі, візуальними характеристиками, а також статистичними властивостями значень ФР. У табл. 3 надано опис кожного датасету із поясненнями трансформацій та обґрунтування вибору кожного датасету.

Архітектура моделей для експериментів

Експериментальну частину було виконано у середовищі Python за допомогою бібліотеки Pytorch. Для практичної демонстрації результатів дослідження було розроблено й реалізовано три архітектури нейронних мереж, кожна з яких відіграє певну роль у дослідженні.

Базова модель – класична згорткова нейронна мережа Base-CNN, яка слугує еталонною моделлю для керованого навчання. Її архітектура складається із чотирьох послідовних шарів Conv2d→*ReLU*. Після згорткових шарів подання передається послідовно у три повнозв'язні шари Linear. Усі інші моделі у цьому експерименті були побудовані на основі цієї моделі з мінімальними модифікаціями, потрібними для реалізації відповідної архітектури. Цю модель навчали тільки на розміченій частині даних (5 % даних). Порівняння метрик інших моделей із базовою моделлю дають можливість відслідкувати, наскільки використання нерозмічених даних покращує класифікаційні якості моделі на тестовій вибірці, тобто наскільки запропонований метод НН ефективний.

Для порівняння запропонованого методу з уже відомими методами НН було обрано базовий АЕ як найближчу за структурою модель. Автоенкодери довели свою ефективність у цьому класі задач за рахунок їхньої здатності вивчати змістовні ознакові подання (feature representations) з нерозмічених даних [19, 14]. У цій роботі модель напівкерованого АЕ (SSL-AE) включає енкодер, що повністю повторює архітектуру енкодера базової моделі, а також декодер, що дзеркально відтворює його структуру, використовуючи шари ConvTranspose2d→*ReLU* для реконструкції зображення. Слід зазначити, що у відкритому доступі не було знайдено публікацій, присвячених НН на обраних наборах даних з ідентичною експериментальною конфігурацією (зокрема, 5 % розмічених даних). Через це для забезпечення коректного і чесного порівняння

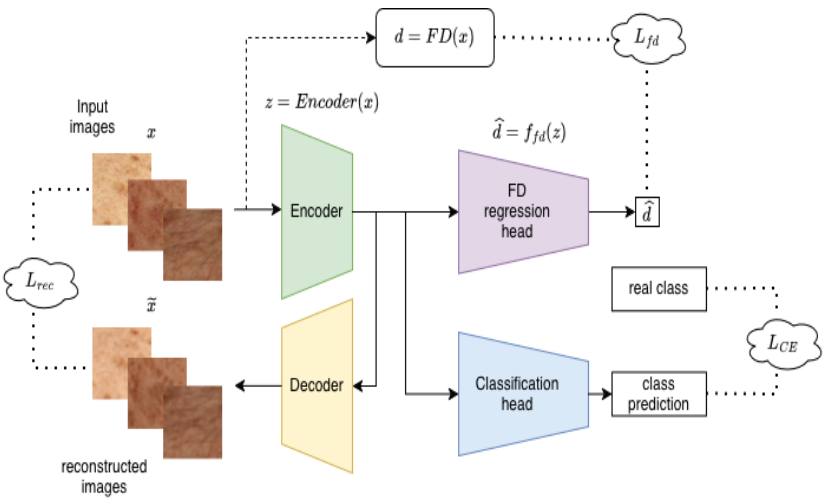

Рис. 1. Модель автоенкодера з фрактальною регуляризацією

базова модель SSL-AE була реалізована нами самостійно з тією ж базовою архітектурою, що й запропонована модель FDR-AE.

Третьою є запропонована модель AE із фрактальною регуляризацією FDR-AE. Вона розширює архітектуру SSL-AE і включає регресійну частину, що намагається на основі вихідного шару енкодера визначити фрактальну розмірність початкового зображення. Регресор складається із двох послідовних повнозв'язних шарів Linear→*ReLU*. Таким чином функція втрат формується як комбінація втрат класифікації, реконструкції та втрат регресійної частини. На рис. 2 зображено внутрішню структуру компонентів моделі, а також яким чином обчислюють різні компоненти функції втрат під час навчання

***Таблиця* 3.** Опис наборів даних, використаних для експериментів

Набір даних	Призначення	Характеристики	Попередня обробка
ISIC2024 Challenge	Бінарна класифікація уражень на шкірі для виявлення раку	Датасет містить 400 000 зображень уражень шкіри, що були отримані з 3d-знімків усього тіла (технологія 3d TBP) [15]	Цей датасет характеризується суттєвим дисбалансом класів. Клас «benign» становить більше 99 % всіх даних, тому для ефективного навчання датасет був збалансований за рахунок видалення із навчальної вибірки більшості екземплярів. Усі зображення були нормалізовані, а також зменшені до розміру 96×96 для зниження витрат ресурсів в експерименті
Містить два класи, що позначають злоякісні та доброякісні утворення – «malignant» та «benign»	Класифікація і сегментація захворювань за радіологічними знімками легень пацієнтів	Набір даних, зібраний дослідниками з Університету Катару та Дакки [16, 17]. Датасет складається із трьох класів: 1) 11 956 знімків пацієнтів із COVID-19, 2) 11 263 знімки вірусної пневмонії (інші інфекції), 3) 10 701 знімок здорових легень. Цей датасет є важливим ресурсом для демонстрації ефективності запропонованого методу, оскільки візуальні ознаки COVID-19 можуть бути менш помітними й вимагати аналізу складних текстурних особливостей знімку	Для спрощення експериментів у межах цього дослідження було використано підмножину, що складається із класів «COVID-19 positive» та «Normal». Таким чином у нашому дослідженні ми розглядали бінарну класифікацію. Усі зображення були нормалізовані, а також зменшені до розміру 96×96 для зниження витрат ресурсів в експерименті
Brain Tumor MRI Dataset	Багатокласова класифікація пухлин мозку за МРТ-зображеннями	Цей набір даних є поєднанням трьох джерел (figshare, SPARTAJ, Br35H) і містить 7023 знімки МРТ людського мозку [18]. Набір даних розподілено на чотири класи: гліома (glioma), менінгіома (meningioma), гіпофізарна пухлина (pituitary) і відсутність пухлини (no tumor). Класи подані у збалансованих пропорціях. Датасет було обрано для демонстрації застосування запропонованого методу на багатокласовому датасеті	Для спрощення експериментів у межах цього дослідження було використано підмножину, що складається із класів «COVID-19 positive» та «Normal». Таким чином у нашому дослідженні ми розглядали бінарну класифікацію. Усі зображення були нормалізовані, а також зменшені до розміру 96×96 для зниження витрат ресурсів в експерименті

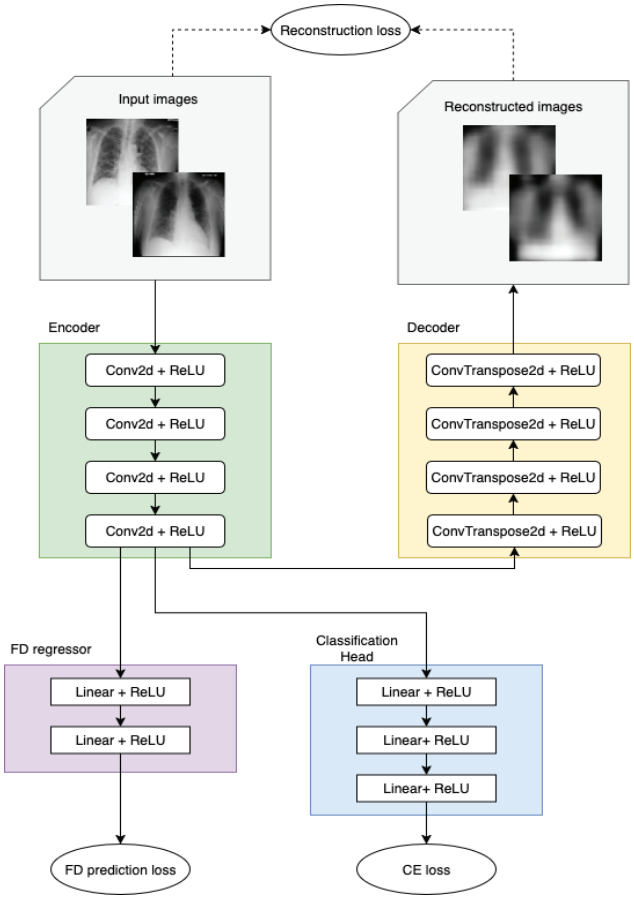

Рис. 2. Модель автоенкодера із фрактальною регуляризацією. Внутрішня структура компонентів моделі

(компоненти функції втрат на рис. 2 обведено еліпсами).

У табл. 4, 5 та 6 наведено метричні показники запропонованих моделей для трьох вищезгаданих датасетів.

Результати експериментів (табл. 4–6) демонструють перевагу запропонованого методу на всіх трьох наборах даних. На датасеті ISIC2024 (табл. 4) FDR-AE модель досягла F1-Score 0.508 для малорепрезентованого класу «malignant», значно перевершивши як Base-CNN (0.304), так і SSL-AE (0.431). Аналогічна ситуація спостерігається також і в датасеті COVID-19 (табл. 5), де FDR-AE покращив якість F1-Score для класу «covid-19» на 0.027 та на 0.112 відносно моделей SSL-AE та Base-CNN. Особливо показовими є результати на багатокласовому датасеті Brain Tumor (табл. 6), де метод суттєво покращив F1-score для всіх класів, причому найбільший приріст відносно SSL-AE отримали класи 0 (0.079) та 3 (0.054), які мали найбільшу взаємну статистичну відмінність у ФР ($\Delta Mean/\max(\sigma) = 0.738$). Таким чином, у всіх трьох сценаріях фрактальна регуляризація виявилася ефективнішою за стандартну реконструкцію (SSL-AE), підтверджуючи, що ФР є цінним сигналом для навчання більш якісних представлень у задачах НН.

Висновки

Наявні рішення для класифікації медичних зображень в умовах дефіциту даних ґрунтуються на НН (SSL), зокрема на АЕ. Утім, стандартна реконструкція не гарантує створення латентного простору, оптимального для класифікації. У цій статті запропоновано новий метод – фрактально-керовану регуляризацію (FDR-AE) – для вирішення цієї проблеми. На відміну від відомих АЕ, наш метод вводить додатковий навчальний сигнал – регресійний шар, який навчається прогнозувати фрактальну розмір-

***Таблиця* 4.** Метричні показники моделей, навчених на 5 % розмічених даних ISIC2024

Модель	Precision (benign)	Precision (malignant)	Recall (benign)	Recall (malignant)	F1 Score (benign)	F1 Score (malignant)
Base-CNN	0.951	0.240	0.897	0.414	0.923	0.304
SSL-AE	0.596	0.524	0.737	0.367	0.659	0.431
FDR-AE	0.615	0.517	0.632	0.500	0.623	0.508

***Таблиця* 5.** Метричні показники моделей, навчених на 5 % розмічених даних COVID-19 Radiology Database

Модель	Precision (normal)	Precision (covid19)	Recall (normal)	Recall (covid19)	F1 Score (normal)	F1 Score (covid19)
Base-CNN	0.799	0.682	0.873	0.552	0.834	0.610
SSL-AE	0.684	0.878	0.920	0.575	0.785	0.695
FDR-AE	0.702	0.896	0.930	0.605	0.800	0.722

***Таблиця* 6.** Метричні показники моделей, навчених на 5 % розмічених даних Brain Tumor MRI Dataset

Модель	Precision (class 0)	Precision (class 1)	Precision (class 2)	Precision (class 3)
Base-CNN	0.683	0.447	0.703	0.598
SSL-AE	0.720	0.500	0.848	0.716
FDR-AE	0.704	0.560	0.848	0.797
Модель	Recall (class 0)	Recall (class 1)	Recall (class 2)	Recall (class 3)
Base-CNN	0.460	0.359	0.773	0.833
SSL-AE	0.447	0.572	0.810	0.927
FDR-AE	0.570	0.549	0.867	0.940
Модель	F1 Score (class 0)	F1 Score (class 1)	F1 Score (class 2)	F1 Score (class 3)
Base-CNN	0.550	0.399	0.736	0.696
SSL-AE	0.551	0.534	0.828	0.808
FDR-AE	0.630	0.554	0.857	0.862

ність зображення з його латентного вектора. Перевага цього методу полягає у примусовому збереженні структурно важливої інформації.

Експерименти з трьома наборами даних (ISIC2024, COVID-19, Brain Tumor) за умови 5 % маркованих даних показали, що FDR-AE стабільно перевершує як базову повністю керовану модель (Base-CNN), так і стандартний AE (SSL-AE). Наприклад, у завданні з чотирма класами Brain Tumor (табл. 6) FDR-AE поліпшив показник F1-Score для всіх класів, причому найбільше зростання (+0,079 і +0,054) було для класів 0 і 3. Сферою застосування методу є системи комп'ютерної діагностики на основі нейронних мереж. Конкретно цей метод може бути застосований як для НН, так і для передннавчання моделей.

Також у процесі дослідження було виявлено суттєве обмеження – метод найбільш ефективний на відносно простих архітектурах та в разі сильного дефіциту даних. На складних моделях з великою кількістю даних ФР може погіршувати кінцеві показники. Це відкриває шляхи для покращення, які стануть предметом наших наступних робіт: використання FDR-AE як методу попереднього навчання (pre-training) і впровадження динамічного коефіцієнта, що автоматично зменшуватиме вплив регуляризації зі зростанням точності моделі. Практична реалізація цих підходів дозволить створити більш стабільні та ефективні моделі НН для підвищення точності автоматизованої діагностики в реальних клінічних умовах.

References

1. C.S. Fortin *et al.*, "Fractal dimension in the analysis of medical images", *IEEE Engineering in Medicine and Biology Magazine*, Vol. 11, no. 2, pp. 65–71, 1992. Retrieved from doi: https://doi.org/10.1109/51.139039
2. S. Kisan *et al.*, "Fractal dimension in medical imaging: a review", *IRJET*, Vol. 5, pp. 1102–1106, 2017. [Online]. Available: https://www.irjet.net/archives/V4/i5/IRJET-V4I5363.pdf. Accessed: Oct. 11, 2025.
3. S. Liu *et al.*, "Relationship between necrotic patterns in glioblastoma and patient survival: fractal dimension and lacunarity analyses using magnetic resonance imaging", *Scientific reports*, Vol. 7, no. 1, p. 8302, 2017. Retrieved from doi: https://doi.org/10.1038/s41598-017-08862-6
4. M.Z.C. Azemin *et al.*, "Robust methodology for fractal analysis of the retinal vasculature", *IEEE Trans Med Imaging*, Vol. 30, no. 2, pp. 243–250, 2011. Retrieved from doi: https://doi.org/10.1109/TMI.2010.2076322
5. R.M. Rangayyan and T. M. Nguyen, "Fractal analysis of contours of breast masses in mammograms", *Journal of digital imaging*, Vol. 20, no. 3, pp. 223–237, 2007. Retrieved from doi: https://doi.org/10.1007/s10278-006-0860-9
6. K. Falconer, "Fractal geometry: mathematical foundations and applications. Chichester: John Wiley", 1990, pp. 38–47. [Online]. Available: www.wiley.com/en-us/Fractal+Geometry%3A+Mathematical+Foundations+and+Applications%2C+3rd+Edition-p-9781119942399#description-section. Accessed: Oct. 11, 2025.

7. S. Buczkowski *et al.*, “Measurements of fractal dimension by box-counting: a critical analysis of data scatter”, *Physica A: Statistical Mechanics and its Applications*, Vol. 252, no. 1–2, pp. 23–34, 1998. Retrieved from doi: https://doi.org/10.1016/S0378-4371(97)00581-5
8. J. Li *et al.*, “An improved box-counting method for image fractal dimension estimation”, *Pattern recognition*, Vol. 42, no. 11, pp. 2460–2469, 2009. Retrieved from doi: https://doi.org/10.1016/j.patcog.2009.03.001
9. C. Panigrahy *et al.*, “Fractal dimension of synthesized and natural color images in lab space”, *Pattern Analysis and Applications*, Vol. 23, no. 2, pp. 819–836, 2020. Retrieved from doi: https://doi.org/10.1007/s10044-019-00839-7
10. R.D.O. Plotze *et al.*, “Leaf shape analysis using the multiscale Minkowski fractal dimension, a new morphometric method: a study with Passiflora (Passifloraceae)”, *Canadian Journal of Botany*, Vol. 83, no. 3, pp. 287−301, 2005. Retrieved from doi: https://doi.org/10.1139/b05-002
11. H. Ahammer, “Higuchi dimension of digital images”, *PLoS One*, Vol. 6, no. 9, p. e24796, 2011. Retrieved from doi: https://doi.org/10.1371/journal.pone.0024796
12. J.B. Florindo and O. Martinez Bruno, “Fractal descriptors in the Fourier domain applied to color texture analysis”, *Chaos: An Interdisciplinary Journal of Nonlinear Science*, Vol. 21, no. 4, 2011. Retrieved from doi: https://doi.org/10.1063/1.3650233
13. A. Makhzani *et al.*, “Adversarial autoencoders”, arXiv preprint arXiv:1511.05644, 2015. Retrieved from doi: https://doi.org/10.48550/arXiv.1511.05644
14. H. Rasmus *et al.*, "Semi-Supervised Learning with Ladder Networks”, in *NIPS'15: Proceedings of the 29th International Conference on Neural Information Processing Systems*, Vol. 2, pp. 3546–3554, 2015. Retrieved from doi: https://doi.org/10.48550/arXiv.1507.02672
15. N.R. Kurtansky *et al.*, “The SLICE-3D dataset: 400,000 skin lesion image crops extracted from 3D TBP for skin cancer detection,” *Scientific Data*, Vol. 11, no. 1, p. 884, 2024. Retrieved from doi: https://doi.org/10.1038/s41597-024-03743-w
16. M.E. Chowdhury *et al.*, “Can AI help in screening viral and COVID-19 pneumonia?”, *IEEE Access*, Vol. 8, pp. 132665–132676, 2020. Retrieved from doi: https://doi.org/10.1109/ACCESS.2020.3010287
17. T. Rahman *et al.*, “Exploring the effect of image enhancement techniques on COVID-19 detection using chest X-ray images”, *Computers in biology and medicine*, Vol. 132, p. 104319, 2021. Retrieved from doi: https://doi.org/10.1016/j.compbiomed.2021.104319
18. M. Nickparvar, “Brain Tumor MRI Dataset”, *Kaggle*, 2023. [Online]. Available: https://www.kaggle.com/datasets/masoudnickparvar/brain-tumor-mri-dataset. Accessed: Oct. 11, 2025.
19. D.P. Kingma *et al.*, “Semi-supervised learning with deep generative models”, in *Advances in neural information processing systems*, Vol. 27, 2014. [Online]. Available: https://papers.nips.cc/paper/5352-semi-supervised-learning-with-deep-generative-models. Accessed: Oct. 11, 2025.

V.Y. Danilov, O.O. Zarytskyi

METHOD FOR FRACTAL-DRIVEN REGULARIZATION OF AUTOENCODERS FOR SEMI-SUPERVISED LEARNING IN MEDICAL IMAGE CLASSIFICATION TASKS

Background. Medical image classification using deep learning is a critical task, yet its effectiveness is constrained by the scarcity of labelled data, which is expensive to acquire. Semi-supervised learning (SSL) methods address this by leveraging unlabelled data. Common autoencoder (AE)-based approaches use reconstruction as a training signal. However, standard reconstruction loss minimisation does not guarantee that the resulting latent space will be optimally structured for the classification task, as the model may focus on diagnostically irrelevant features.

Objective. The paper aims to develop and experimentally validate a novel latent space regularisation method: fractal-driven regularisation (FDR). The goal is to improve classification metrics for medical images under conditions of severe labelled data scarcity (5 %) by integrating fractal dimension (FD) as an additional, a priori training signal.

Methods. The proposed model (FDR-AE) is based on an autoencoder architecture, augmented with two heads attached to the latent space: a classification head and a regression head. The regression head is trained to predict the input image’s FD, which is precalculated using the “box-counting” method. The total loss function is a combination of three components: classification loss (on 5 % labelled data) and both reconstruction and fractal regression losses (on 100 % of data). The method’s efficac was validated on three datasets of different modalities (ISIC2024, COVID-19 Radiology, Brain Tumor MRI), comparing it against a baseline convolutional network (Base-CNN) and a standard semi-supervised autoencoder (SSL-AE).

Results. The experiments demonstrated a consistent advantage for the proposed method. On the ISIC2024 dataset, FDR-AE achieved an F1-Score of 0.508 for the “malignant” class, compared to 0.431 for SSL-AE and 0.304 for Base-CNN. On the COVID-19 dataset, the F1-Score for the “covid19” class was 0.722 for FDR-AE versus 0.695 for SSL-AE. In the 4-class Brain Tumor task, FDR-AE showed improved F1-Scores across all classes, with the most significan gains (+0.079 and +0.054) observed for classes 0 and 3, which also had the greatest mutual statistical difference in their FD values

Conclusions. Fractal-driven regularisation demonstrates that FD is a valuable a priori signal for learning higher-quality, structurally grounded representations in SSL tasks. The method is particularly effective on simple architectures under severe data scarcity. Prospects for future research include utilising FDR as a pre-training method or implementing a dynamic coefficien for the regression component of the loss function.

Keywords: semi-supervised learning; fractal dimension; autoencoder; latent space regularisation; medical images; image classification; box-counting

Рекомендована Радою
Навчально-наукового інституту прикладного системного аналізу
КПІ ім. Ігоря Сікорського

Надійшла до редакції
25 жовтня 2025 року

Прийнята до публікації
8 грудня 2025 року

DOI: https://doi.org/10.20535/kpisn.2025.4.343191
UDC 004.855.5

V.O. Nikitin[1]*, V.Ya. Danilov[1]
[1]Igor Sikorsky Kyiv Polytechnic Institute, Kyiv, Ukraine
*corresponding author: nvo63911@gmail.com

DEEP LEARNING-BASED MELANOMA CLASSIFICATION ENHANCED BY FRACTAL DIMENSION ANALYSIS

Background. Melanoma is a malignant skin lesion that is prone to metastasise aggressively, leading to an almost guaranteed lethal outcome if left unchecked. In contrast, early-stage detection allows for the tumour to be removed via a harmless surgical procedure that may not even leave a scar. However, the availability of competent diagnostics are often limited due to a shortage of healthcare specialists and technologies. Deep Learning models such as Visual Transformer (ViT) have demonstrated strong performance, but researchers continuously seek to improve the results by incorporating new features. Since human skin exhibits fractal-like characteristics, it is theorised that metrics quantifying this complexity can act as valuable supplementary features for DL models, leading to increased classification accuracy.
Objective. We investigated the impact of the integration of fractal dimension (FD) on a Vision Transformer deep learning model used for melanoma classification. A comparison was conducted between the model that was exposed to random noise and the models that were provided with computed FD values.
Methods. Vision Transformer was used as a feature-extracting backbone pre-trained on the ImageNet dataset. Fine-tuning was done on this backbone in combination with a classification head targeted to distinguish melanoma vs. nevus classes. Along with extracted features, the classification head received FD value. An identical model received random noise instead of FD. Statistical testing and FD impact analysis were conducted to validate the significance of the new feature.
Results. Integrating FD into ViT showed noticeable improvement in test metrics. SHAP analysis confirmed the meaningfulness of the new feature. McNemar's test validated that the difference in model predictions was statistically significant.
Conclusions. The results suggest that FD can serve as a valuable supplementary feature for DL models, and the integration of biomarkers such as FD provides a basis for more robust melanoma classification.
Keywords: deep learning; vision transformer; melanoma; fractal dimension; XAI; skin cancer.

Introduction

Malignant skin lesions, such as squamous cell carcinoma and melanoma, can metastasise at advanced stages, significantly reducing the chances of successful treatment. Among those, melanoma is considered the most aggressive skin cancer type. Late-stage melanoma has a low likelihood of a positive outcome. In contrast, early-stage lesions can often be surgically removed with just minimal or no scarring [1]. However, the availability of competent diagnostics is often limited due to a shortage of healthcare specialists and technologies. Consequently, there is ongoing research focused on developing robust computer-aided diagnostic (CAD) systems leveraging deep learning (DL) techniques, which is being undertaken by various teams, including ISIC [2].

Data feature engineering is a significant part of any machine learning (ML) pipeline. Since human skin exhibits fractal-like characteristics, it is hypothesized that Fractal Dimension (FD) may serve as a valuable feature for enhancing DL-based skin lesion classification models [3]. FD is a metric that quantifies the complexity of fractal-like structures.

To investigate this hypothesis, we employed the Vision Transformer (ViT) [4] model as a feature extractor, as it has demonstrated strong performance in skin cancer classification tasks [5].

Пропозиція для цитування цієї статті: В.О. Нікітін, В.Я. Данилов, "Модель глибокого навчання для класифікації меланоми, покращена за допомогою фрактальної розмірності", *Наукові вісті КПІ*, № 4, с. 40–45, 2025. doi: https://doi.org/10.20535/kpisn.2025.4.343191

Offer a citation for this article: V.O. Nikitin, V.Ya. Danilov, "Deep learning-based melanoma classif ication en-hanced by fractal dimension analysis", *KPI Science News*, no. 4, pp. 40–45, 2025. doi: https://doi.org/10.20535/kpisn.2025.4.343191

Contributions

We hypothesise that integrating FD as a feature to DNN Skin Cancer Classifier can improve the results. The main contributions of this study are as follows: We developed a deep neural network (DNN) classifier that combines ViT-extracted features with FD as an additional input. We conducted statistical analysis, including McNemar's test, to confirm the significance of the observed performance improvements after incorporating FD. Evaluation of the FD impact was performed using SHAP (SHapley Additive exPlanations).

Related Work

Fractal Dimension in Skin Lesion Analysis. Fractal Dimension has been explored as a quantitative metric to capture the complexity and irregularity of skin lesion boundaries. Studies have demonstrated that FD can potentially serve as a discriminative feature in differentiating between benign and malignant lesions [3]. For instance, research utilising the Higuchi's method for computing surface FD, combined with colour features, achieved classification accuracy of approximately 80 % [6]. Despite these promising results, the integration of FD into DL architectures for skin lesion classification remains fairly underexplored. We previously made efforts on the integration of FD to DL models such as Vision Transformer. The study showed that FD can positively impact a model's output [7]. Another of our studies explored approximating FD for skin lesions. In this study, the box counting dimension and its modification were compared against the Hausdorff dimension of real fractals [8].

Vision Transformers in Skin Cancer Classification. ViTs leverage self-attention mechanisms to capture global contextual information, which is particularly beneficial in analysing complex skin lesion patterns. Recent studies have demonstrated the efficacy of ViTs in skin cancer classification tasks, achieving high accuracy rates [5]. For example, a study employing a ViT model on the HAM10000 dataset reported an accuracy of 96.15 % [9].

Explainable AI in Medical Image Classification. The integration of explainable AI (XAI) techniques in medical image classification has become increasingly important to enhance model transparency and trustworthiness. SHapley Additive exPlanations (SHAP) is one such technique that provides insights into feature contributions towards model predictions. In the context of skin lesion classification, SHAP has been utilised to interpret model decisions, thereby aiding in the validation and acceptance of AI systems in clinical settings [10].

Methods

Model Selection and Study Design. The Vision Transformer architecture was selected as the base model, building upon our previous investigation into integrating FD in [7], where preliminary results indicated potential benefits. In this study, the methodology was improved through more rigorous data selection and splitting, while hyperparameters were set based on prior research. We also reduced the problem to binary classification, leaving only malignant (melanoma) and benign (nevus) classes. We compared models that receive random noise as an additional feature vs. fractal dimension. The aim was to identify if FD is useful to a DL classifier.

Data. We utilised ISIC 2019 dataset [2]. It is composed of HAM10000 (ViDIR Group, Department of Dermatology, Medical University of Vienna) [11], BCN20000 (Department of Dermatology, Hospital Clнnic de Barcelona) [12], and MSK Dataset (anonymous).

The data was reduced to only two classes: melanoma and nevus. Class imbalance was addressed by taking a number of nevi samples equal to the amount of melanoma samples. All the data was resized to 224Ч224 pixels. In order to achieve more robust training, augmentation was applied: random flipping (horizontal and vertical), random sharpness adjustment, random rotations (0°, 90°, 180°, or 270°), color jitter (brightness, contrast, and saturation varied within [0.9, 1.1]), and random resized cropping (scale: 0.9, 0.9). Training split represents the one from the ISIC 2019 Challenge [2]. Test and validation datasets were taken from ISIC 2019 Test data in a ratio of 4:1.

Fractal Dimension Calculation. We defined two approaches for calculating the fractal dimension (FD) of a lesion.

In the first approach, the FD is calculated from the curve representing the lesion's border, for which we used the box-counting dimension [13]. The lesion was preprocessed as follows (results can be seen on Fig. 1):

1. Hair was removed using the Dull Razor algorithm [14].
2. The image was converted to grayscale.
3. The image was cropped, assuming the lesions are centered.
4. The Canny edge detection algorithm [15] was applied.

5. To remove small artefacts picked up by Canny, we used openCV.findContours [16] selected the largest contour, eroded it, and applied it as a mask to Canny results.

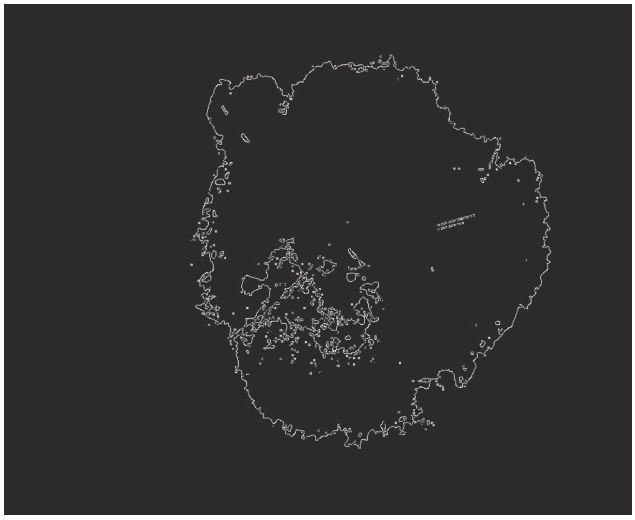

Fig. 1. Borders of a lesion

The second approach assumes the lesion is a 2D plane. We used two methods to assess the FD for this lesion representation here: a modified intensity-based dimension presented in [3], and a 2D version of the Higuchi fractal dimension [17]. Preprocessing for this approach included only cropping and grayscaling.

Model Architecture and Training. The ViT variant vit_b_32 was employed with ImageNet weights. The models were trained using the categorical cross-entropy loss function and optimised with the Adam optimiser, initialised with a learning rate of 1e-5 for classification layers and 1e-6 for fine-tuning pre-trained ViT layers. torch.optim.lr_scheduler. CosineAnnealingLR(eta_min=1e-7) was applied to mitigate overfitting. Each model was trained for a maximum of 30 epochs, with early stopping applied if the validation loss failed to improve for five consecutive epochs. FD was integrated into the model by concatenating it as an additional input to the classifier head. Prior to integration, the FD values underwent a preprocessing pipeline consisting of a linear layer (torch.nn.Linear(1, 16)). The final classifier head was structured as follows: Normalisation, Linear, GELU, Dropout, Normalisation, Linear.

Evaluation Metrics and Statistical Analysis. Model performance was assessed using accuracy, precision, recall, and F1-score. Given that the dataset, after modifications, was balanced, these metrics provided a meaningful basis for comparison. Performance was evaluated across all 3 datasets (train, validation and test). To test the significance of performance differences between the baseline and FD-enhanced models, McNemar's test – a paired chi-square test frequently employed in machine learning studies – was applied to the predictions on the test set. Finally, SHAP values were computed to quantify the contribution of FD to individual model predictions, providing insight into the actual impact of FD as an auxiliary feature.

Experiments and results

The experiment results are presented in Table 1. RN represents a model that received random noise (our control model), BC FD – box counting dimension, IFD – intensity-based box counting dimension and HFD – Higuchi dimension.

Statistical Analysis. To assess whether the performance differences between the baseline model (without FD) and the FD-enhanced model were statistically significant, McNemar's test was applied. We specifically tested BC FD as it showed the best test results. Predictions from both models were compared using predictions on the test dataset. A 2×2 contingency table was constructed, recording the number of samples where both models were correct, both were incorrect, or where one model outperformed the other. McNemar's test was performed using the standard χ^2 approximation with continuity correction applied. A significance level of 0.05 was used to determine whether the performance differences were statistically significant.

McNemar's test revealed a statistically significant difference in the performance of the two models ($\chi^2 > 3.841$, $p < 0.05$). Specifically, the FD-enhanced model made significantly different predictions compared to the baseline model. Given that the FD-enhanced models also achieved higher accuracy, F1-score, recall, and precision, the results support the positive contribution of the FD feature to improved classification performance.

SHAP Analysis. SHAP (SHapley Additive exPlanations) values were computed using GradientExplainer for all samples in the test set. The plots below summarise the impact of random noise and FD in predicting malignant classes (Fig. 2).

As expected, SHAP analysis revealed that the FD feature has a monotonic relationship between the feature value and its impact on the "Malignant" class prediction. This finding is significant as it aligns with the clinical hypothesis that malignant lesions exhibit more complex, irregular boundaries,

***Table* 1.** Performance comparison of the control model (RN) and FD-enhanced models (BC FD, IFD, HFD) across train, validation, and test sets

Dataset	Metric	RN	BC FD	IFD	HFD
Train	Precision	0.901988	0.942235	0.923132	0.876098
Train	Recall	0.859372	0.828839	0.867172	0.844662
Train	Accuracy	0.882995	0.889013	0.897482	0.862603
Train	F1-Score	0.880164	0.881907	0.894277	0.860093
Validation	Precision	0.771875	0.800000	0.810559	0.795597
Validation	Recall	0.953668	0.908367	0.970260	0.958333
Validation	Accuracy	0.838095	0.847619	0.868571	0.855238
Validation	F1-Score	0.853195	0.850746	0.883249	0.869416
Test	Precision	0.772270	0.801292	0.773220	0.768995
Test	Recall	0.947719	0.935849	0.958733	0.957020
Test	Accuracy	0.833572	0.850262	0.839771	0.835002
Test	F1-Score	0.851046	0.863359	0.856041	0.852766

which are captured by a higher fractal dimension. At the same time, analysis from the control model trained on a random noise feature demonstrates a near null impact with SHAP values randomly scattered around zero.

Results of SHAP analysis suggest that the FD feature provides a genuine and interpretable predictive signal, which the model successfully learned to exploit, whereas it correctly ignored the irrelevant control feature.

Discussion

The results of this study demonstrate that incorporating FD into a DL pipeline for skin cancer classification yields consistent improvements across key performance metrics, including accuracy, precision, recall, and F1-score. The FD-enhanced models outperformed the baseline ViT model across all evaluation datasets (train, validation, and test). These findings support the initial hypothesis that FD can serve as a valuable auxiliary feature by capturing the inherent fractal characteristics present in skin lesion morphology.

The application of McNemar's test confirmed that the observed performance improvements were statistically significant, reducing the likelihood that these gains were due to random variation. Furthermore, SHAP analysis provided insight into the role of FD within the model's decision-making process. SHAP values indicated that FD had a direct contribution to individual

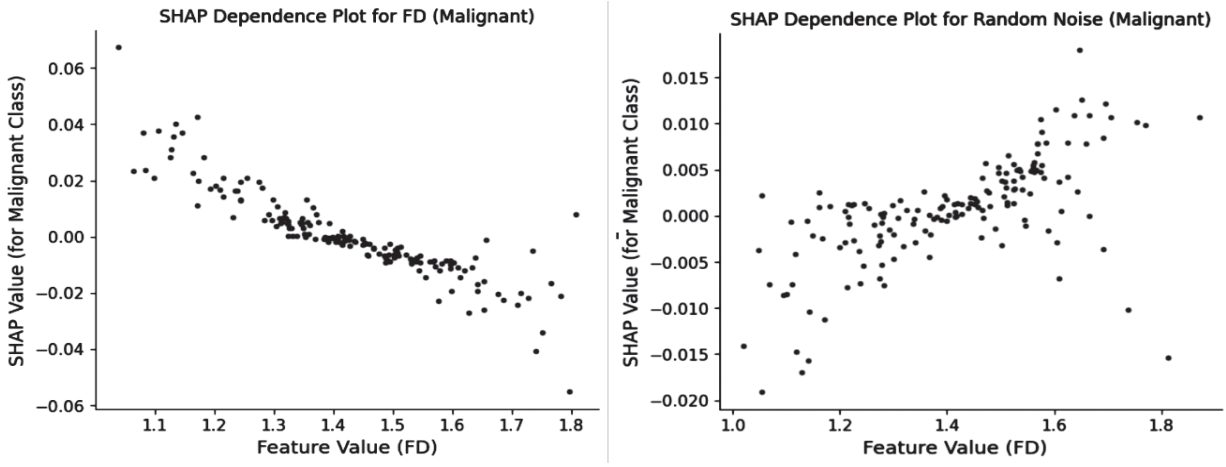

Fig. 2. SHAP Dependence plot for FD and Random Noise

predictions. This effect may promote better model generalisation.

However, limitations must be acknowledged. The study focused exclusively on the ISIC 2019dataset, which, while comprehensive, consists primarily of dermoscopic images. This reliance does not guarantee generalizability to real-world clinical settings, where images may be captured by non-dermoscopic tools. Furthermore, the task was simplified to a binary classification between melanoma and nevus, which are often visually distinct. The contribution of FD may differ in a more complex, multi-class scenario involving other, more similar-looking lesion types, especially ones in intermediate stages between benign and malignant.

Regarding the feature itself, the SHAP analysis revealed that though the absolute magnitude of the FD's contribution is often subtle, it confirmed a clear correlation. This suggests its impact could be secondary to the primary features extracted by the ViT. Our approach to calculating 2D FD on a simple crop instead of a lesion bounding box or segmentation mask impacted the accuracy of the value. It would be valuable to investigate the fusion of FD with other state-of-the-art architectures, such as traditional CNNs or Hybrid Attention CNN models. It would potentially depend on whether the received results are specific to Transformers or a more universal feature.

Nevertheless, this contribution remains significant, as we not only improved the ViT's classification metrics but also used SHAP to confirm that the fractal dimension feature was responsible for this improvement in a clinically coherent manner.

Conclusions

This study introduced and evaluated the integration of FD as an auxiliary feature in a ViT-based skin cancer classification model. Empirical results demonstrated that FD-enhanced models consistently outperformed baseline models across multiple performance metrics. Statistical testing confirmed the significance of these improvements, while explainable AI techniques (SHAP) provided additional interpretability regarding FD's role in model predictions.

The findings underscore the potential of incorporating geometric complexity measures, such as FD, to enhance DL models in medical image analysis. This approach contributes to the growing body of research on explainable and reliable AI for healthcare applications. Future work will focus on expanding the methodology to diverse datasets, exploring alternative fractal metrics, and investigating the potential of FD in other medical imaging tasks beyond skin cancer classification.

References

[1] World Cancer Research Fund International, "Skin cancer statistics," 2022. [Online]. Retrieved from: https://www.wcrf.org/cancer-trends/skin-cancer-statistics/. [Accessed: Nov. 7, 2025].

[2] International Skin Imaging Collaboration (ISIC), "ISIC Archive." [Online]. Retrieved from: https://www.isic-archive.com/. [Accessed: Nov. 7, 2025].

[3] P. Popecki *et al.*, "Fractal dimension analysis of melanocytic nevi and melanomas in normal and polarised light-A preliminary report," Life, Vol. 12, no. 7, p. 1008, 2022. doi: 10.3390/life12071008

[4] A. Dosovitskiy *et al.*, "An image is worth 16×16 words: Transformers for image recognition at scale," arXiv preprint arXiv:2010.11929, 2021. [Online]. Retrieved from: https://doi.org/10.48550/arXiv.2010.11929

[5] S. Khan *et al.*, "Identifying the role of vision transformer for skin cancer – A scoping review," *Frontiers in Artificial Intelligence*, Vol. 6, Jul. 2023, doi: 10.3389/frai.2023.1202990

[6] S. Moldovanu *et al.*, "Skin lesion classification based on surface fractal dimensions and statistical colour cluster features using an ensemble of Machine Learning Techniques," Cancers, Vol. 13, no. 21, p. 5256, 2021. doi: 10.3390/cancers13215256

[7] V. Nikitin and V. Danilov, "Integration of fractal dimension in vision transformer for skin cancer classification," *Electronics and Control Systems*, no. 76, 2023. doi: 10.18372/1990-5548.76.17662

[8] V. Nikitin and V. Danilov, "Fractal dimension calculation techniques for skin lesion characterisation," in *Матеріали конференцій МЦНД*, 2024. doi: 10.62731/mcnd-26.07.2024.005

[9] G.M. S. Himel *et al.*, "Skin cancer segmentation and classification using vision transformer for automatic analysis in dermatoscopy-based non-invasive digital system," arXiv preprint arXiv:2401.04746, 2024. [Online]. Retrieved from: https://doi.org/10.48550/arXiv.2401.04746.

[10] T. Khater *et al.*, "Skin cancer classification using explainable artificial intelligence on pre-extracted image features," *Intelligent Systems with Applications*, Vol. 21, p. 200275, Feb. 2024. doi: 10.1016/j.iswa.2023.200275

[11] P. Tschandl *et al.*, "The HAM10000 dataset, a large collection of multi-source dermatoscopic images of common pigmented skin lesions," *Scientific Data*, Vol. 5, p. 180161, 2018. doi: 10.1038/sdata.2018.161

[12] M. Combalia *et al.*, "BCN20000: Dermoscopic lesions in the wild," arXiv preprint arXiv:1908.02288, 2019. [Online]. Retrieved from: https://doi.org/10.48550/arXiv.1908.02288. [Accessed: Nov. 8, 2025].

[13] J. Wu *et al.*, "An effective method to compute the box-counting dimension based on the mathematical definition and intervals," *Results in Engineering*, Vol. 6, p. 100106, 2020. doi: 10.1016/j.rineng.2020.100106

[14] T. Lee *et al.*, "Dullrazor®: A software approach to hair removal from images," *Computers in Biology and Medicine*, Vol. 27, no. 6, pp. 533–543, Nov. 1997. doi: 10.1016/s0010-4825(97)00020-6

[15] J. Canny, "A Computational Approach to Edge Detection," *IEEE Trans. Pattern Anal. Mach. Intell.*, Vol. 8, no. 6, pp. 679–698, Nov. 1986.

[16] S. Suzuki and K. Abe, "Topological structural analysis of digitised binary images by border following," *Computer Vision, Graphics, and Image Processing*, Vol. 30, no. 1, pp. 32–46, Apr. 1985.

[17] S. Spasić, "On 2D generalisation of Higuchi's fractal dimension," *Chaos, Solitons & Fractals*, Vol. 69, pp. 179–187, Dec. 2014. doi: 10.1016/j.chaos.2014.09.015

В.О. Нікітін, В.Я. Данилов

МОДЕЛЬ ГЛИБОКОГО НАВЧАННЯ ДЛЯ КЛАСИФІКАЦІЇ МЕЛАНОМИ, ПОКРАЩЕНА ЗА ДОПОМОГОЮ ФРАКТАЛЬНОЇ РОЗМІРНОСТІ

Проблематика. Меланома – це злоякісне ураження шкіри, схильне до агресивного метастазування, що призводить до майже гарантованого летального наслідку, якщо його не лікувати. На противагу цьому, виявлення на ранній стадії дозволяє видалити пухлину, застосувавши безпечну хірургічну процедуру, яка може навіть не залишити шраму. Утім, доступність компетентної діагностики часто обмежена через нестачу медичних фахівців і технологій. Моделі глибокого навчання (ГН), такі як Visual Transformer (ViT), продемонстрували високу ефективність, але дослідники постійно прагнуть покращити результати, включаючи нові ознаки. Оскільки шкіра людини має фракталоподібні характеристики є гіпотеза, що метрики, які кількісно оцінюють цю складність, можуть слугувати цінними додатковими ознаками для моделей ГН, що підвищує точність класифікації.

Мета дослідження. Ми дослідили вплив інтеграції фрактальної розмірності (ФР) у модель глибокого навчання ViT, яку використовують для класифікації меланоми. Було проведено порівняння між моделлю, які отримувала випадковий шум, і моделями, що отримували розраховані значення ФР.

Методика реалізації. Модель ViT використовували як основу для визначення ознак для класифікації, наперед навчивши на наборі даних ImageNet. Цю основу доналаштовували (fine-tuning) в поєднанні із класифікатором (head), призначеним для розрізнення класів меланоми та невуса. Разом із вилученими ознаками класифікаційний модуль отримував значення ФР. Ідентична модель отримувала випадковий шум замість ФР. Для підтвердження значущості нової ознаки було проведено статистичне тестування та аналіз впливу ФР.

Результати дослідження. Інтеграція ФР у ViT показала помітне покращення тестових метрик. Аналіз SHAP підтвердив змістовність нової ознаки. Тест МакНемара підтвердив, що різниця у прогнозах моделі була статистично значущою.

Висновки. Результати свідчать, що ФР може слугувати цінною додатковою ознакою для моделей ГН, а інтеграція біомаркерів, таких як ФР, забезпечує основу для більш надійної класифікації меланоми.

Ключові слова: глибоке навчання; візуальний трансформер; меланома; фрактальна розмірність; пояснювальний штучний інтелект; рак шкіри.

Рекомендована Радою
Навчально-наукового інституту
прикладного системного аналізу
КПІ ім. Ігоря Сікорського

Надійшла до редакції
25 жовтня 2025 року

Прийнята до публікації
19 грудня 2025 року

DOI: https://doi.org/10.20535/kpisn.2025.4.343329
UDC 004:85

D.V. Androsov[1]*, N.I. Nedashkovskaya[1]
[1]Igor Sikorsky Kyiv Polytechnic Institute, Kyiv, Ukraine
*corresponding author: androsov.dmytro@lll.kpi.ua

SYSTEM APPROACH TO MULTICRITERIA EVALUATION OF SESSION-BASED AND SEQUENTIAL RECOMMENDATION SYSTEMS

Background. Recommendation systems have become indispensable components of modern digital platforms, enabling personalised content delivery across diverse domains. Traditional collaborative filtering and content-based approaches often fail to capture temporal dynamics and contextual dependencies inherent in user behaviour patterns. Sequential recommendation systems (SRSs) and session-based recommendation systems (SBRSs) have emerged as new paradigms to capture users' short-term but dynamic preferences for enabling more timely and accurate recommendations.
Objective. The paper aims to propose a system approach for multicriteria evaluation of various SRS and SBRS models – a unified framework for understanding these models, selecting the best recommendation model, and guiding future research directions in temporal-aware recommendation systems, as well as to provide a systematic overview and comprehensive analysis of session-based and sequential recommendation systems, to examine their theoretical foundations, evolution, empirical performance characteristics, and practical deployment considerations.
Methods. A comprehensive analysis of foundational approaches from Markov chain models to modern neural architectures, including attention-based methods, graph neural networks, and state-space models, is conducted. The approaches are systematically categorised based on architectural principles, temporal modelling strategies, and knowledge integration methods. The Analytic Hierarchy Process is applied for the calculation of relative importance of benefits, costs, opportunities and risks in a problem of session-based and sequential recommendation systems synthesis. An experimental study of various SRS and SBRS models was performed on benchmark datasets.
Results. Empirical studies on the temporal benchmark dataset show that combining SASRec and ReCODE improves the Recall@K metric by 9 % over the baseline SASRec model, and combining GRU4Rec with ReCODE improves the metric by 17 % over the baseline GRU4Rec. The SASRec model, which adapts transformer architectures to the sequential recommendation problem, achieved the highest baseline performance in terms of Recall@K and NDCG@K criteria on the benchmark dataset compared to the other examined models, demonstrating the effectiveness of self-attention mechanisms for sequence modelling. ReCODE is a model-independent neural ordinary differential equation framework for recommender systems and an effective framework for studying consumer demand dynamics, has improved the metrics of existing baseline approaches, and has acceptable computational complexity for practical recommender system deployment scenarios.
Conclusions. Session-based and sequential recommendation systems have evolved through several paradigmatic shifts with significant scientific achievements, including establishment of session-based recommendation model as distinct from traditional collaborative filtering, development of attention mechanisms for sequence modelling, and introduction of continuous-time formulations. Future research directions include unified architectures, scalability solutions, improved evaluation methodologies, and extensions to multi-stakeholder scenarios.
Keywords: sequential recommendation; session-based recommendation; temporal modelling; attention mechanisms; graph neural networks; state-space models; deep learning; system analysis; decision making.

Пропозиція для цитування цієї статті: Д.В. Андросов, Н.І. Недашківська, "Системний підхід до багатокритеріального оцінювання сеансових і послідовних рекомендаційних систем", *Наукові вісті КПІ*, № 4, с. 46–54, 2025. doi: https://doi.org/10.20535/kpisn.2025.4.343329

Offer a citation for this article: D.V. Androsov1*, N.I. Nedashkovskaya1, "System approach to multicriteria evaluation of session-based and sequential recommendation systems", *KPI Science News*, no. 4, pp. 46–54, 2025. doi: https://doi.org/10.20535/kpisn.2025.4.343329

Introduction

Recommendation systems have revolutionised digital content consumption by enabling personalised experiences across e-commerce platforms, streaming services, social media, and news aggregators [1–3]. These systems address the fundamental challenge of information overload by filtering vast content catalogs to present users with relevant items tailored to their preferences and contextual needs.

Traditional recommendation approaches, primarily collaborative filtering and content-based methods, treat user-item interactions as static snapshots, failing to account for the temporal dynamics that characterise real-world user behaviour [2]. However, user preferences evolve continuously over time, influenced by seasonal patterns, trending topics, life events and changing interests. Static models cannot capture preference drift, limiting their ability to provide timely and relevant recommendations [4, 5].

User interactions demonstrate complex sequential patterns where the order, timing and context of actions significantly influence future preferences. For instance, purchasing a camera may increase the likelihood of buying related accessories, but this dependency weakens over time [6, 7].

Also, many modern applications operate with anonymous users or scenarios where long-term user profiles are unavailable due to privacy constraints, cookie limitations or new user cold-start problems. These situations require systems to make accurate recommendations based solely on current session interactions without historical context [4–7].

These challenges have motivated the development of sequential recommendation systems and session-based recommendation systems, representing a paradigmatic shift toward temporal-aware personalisation that adapts to dynamic user contexts and behavioural patterns [8, 9].

The evolution of sequential recommendation systems has been marked by several technological breakthroughs that have progressively addressed the limitations of static approaches:

1. Foundational period (2001–2014). Early work established theoretical foundations through Markov chain models [9, 10] and matrix factorisation extensions [4, 6]. The factorised personalised Markov chain [6] represented a crucial advancement by combining collaborative filtering with Markovian temporal modelling.

2. Deep learning emergence (2015–2017). The introduction of deep learning marked a transformative period. GRU4Rec [11] pioneered neural session-based recommendation, demonstrating superior performance over traditional methods.

3. Attention era (2018–2020). Transformer architectures revolutionised sequential recommendation through SASRec [12], which adapted self-attention for next-item prediction, and BERT4Rec [13], which employed bidirectional attention with masked language modelling training.

4. Post-attention period (2019-present). Graph neural networks enhanced recommendation through SR-GNN [14], which modelled sessions as directed graphs, and knowledge-aware approaches like KGAT [15] that integrated external knowledge graphs. The recent advances in modelling ordinary differential equations as hidden layers functions within deep neural networks enabled the sensitivity of these models to irregularly-sampled data, which became suitable for estimating the consumption trends of goods [16, 17].

However, comprehensive empirical studies [18] have revealed significant methodological concerns and demonstrated that many sophisticated neural approaches fail to consistently outperform simple baselines when evaluated under rigorous conditions with standardised datasets and fair comparison protocols.

Problem Statement

The primary objective is to establish a comprehensive understanding of session-based and sequential recommendation systems through a systematic overview of their theoretical foundations, architectural innovations, empirical performance characteristics, and practical deployment considerations.

The system analysis aims to provide a unified conceptual framework that enables researchers and practitioners to navigate the complex landscape of temporal-aware recommendation approaches and make informed decisions about methodology selection and future research directions.

A system approach

We propose a system approach (Fig. 1) aimed at the evaluation of scenarios for practical deployment of session-based and sequential recommendation systems using the following decision criteria:

1. Performance metrics such as Recall@K – the proportion of model outcomes marked as relevant in the set of ground-truth relevant items; Precision@K – the proportion of relevant elements (items) for user in the set of items, generated by the

model; MAP@K, NDCG@K, MRR@K, which are aimed at assessing the quality of recommendation system to rank items based on their relevance for user.

2. Computational efficiency criteria and metrics, which include:

• model training time;

• computational scalability;

• average time per K inferences (ATI@K) – average computation time for generating top-K item recommendations across user session batches;

• memory usage – peak memory consumption during model inference to assess scalability for production deployment scenarios.

The following opportunities and risks are also taken into account in the process of evaluation of scenarios for the practical deployment of session-based and sequential recommendation systems:

• temporal modelling;

• long-range dependencies;

• knowledge integration complexity;

• discovery of user behavioural patterns (collaborative signals);

• usability of the model that expresses the complexity of the model for the developer, reflecting the number of "change axes" of the algorithm;

• theoretical foundations.

These decision criteria, metrics, opportunities and risks enable comprehensive evaluation of both recommendation quality and computational efficiency, crucial factors for practical deployment of sequential recommendation systems in large-scale e-commerce environments.

Scenarios could, for example, be formed based on hybrid technologies: recurrent neural networks or attention-based models equipped with neural ordinary differential equations framework and other.

Let us consider traditional and modern models and methods for session-based and sequential recommendation systems synthesis.

Markov chain models for sequential recommendations

The theoretical foundations of sequential recommendation were established through probabilistic modelling using Markov chains, which represent user behaviour as stochastic processes over discrete state spaces [9, 10].

The basic first-order Markov assumption posits that the probability of the next interaction depends solely on the current state:

$$P\left(s_{t+1} \mid s_1, s_2, ..., s_t\right) = P\left(s_{t+1} \mid s_t\right)$$

While conceptually appealing for modelling sequential dependencies, these models suffered from severe data sparsity issues due to the exponential growth of transition parameters with vocabulary size, limiting their practical applicability to large-scale systems.

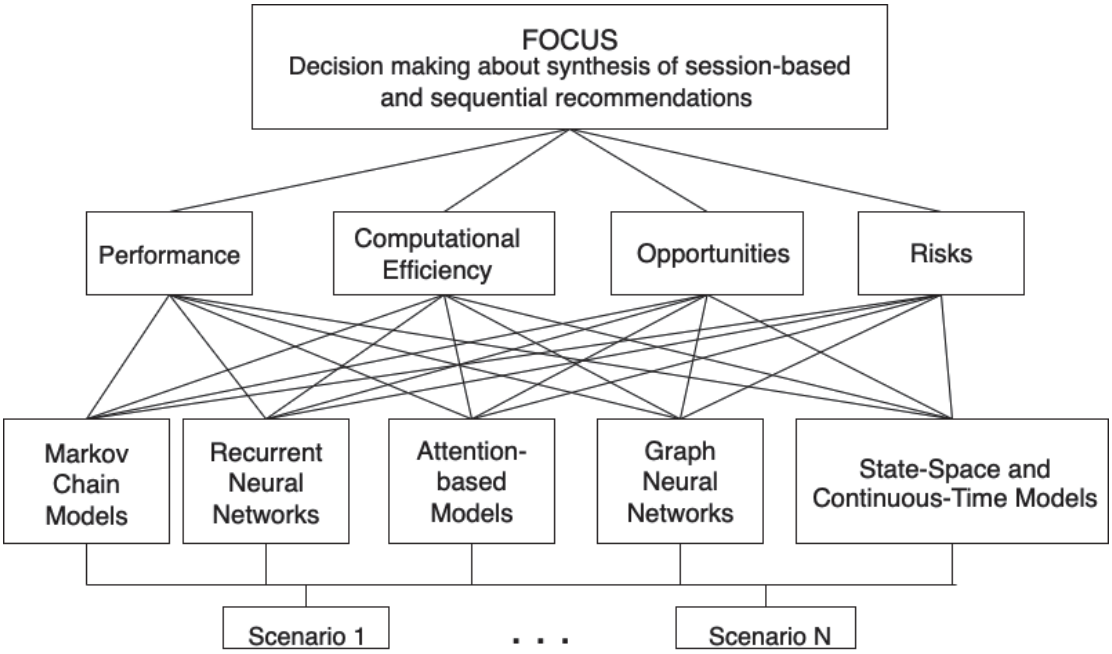

Fig. 1. Scheme of a system approach

The factorized personalized Markov chain addressed sparsity through low-rank matrix factorisation, decomposing the three-way user-item-item tensor into personalised transition matrices [6]:

$$\hat{x}_{uij} = \left\langle u_u + u_i, v_j \right\rangle + \left\langle l_i, r_j \right\rangle,$$

where u_u, u_i represent user and current item factors, v_j represents the target item factor, and l_i, r_j encompass model item-to-item transitions.

Recurrent neural networks for sequential recommendations

The introduction of recurrent neural networks marked a paradigmatic shift toward end-to-end learning of sequential patterns without explicit state space assumptions.

GRU4Rec model pioneered neural session-based recommendation through gated recurrent units, demonstrating superior performance over traditional collaborative filtering methods [11]:

$$r_t = \sigma\left(W_r x_t + U_r h_{t-1}\right);$$

$$z_t = \sigma\left(W_z x_t + U_z h_{t-1}\right);$$

$$\tilde{h}_t = \tanh\left(W_h x_t + U_h (r_t \otimes h_{t-1})\right);$$

$$h_t = \left(1 - z_t\right) \otimes h_{t-1} + z_t \otimes \tilde{h}_t.$$

Attention-based models for sequential and session-based recommendations

The transformer revolution in natural language processing motivated its adaptation to sequential recommendation systems through self-attention mechanisms that enable parallel computation and direct modelling of arbitrary-length dependencies.

SASRec model adapted transformer architectures for sequential recommendation through unidirectional self-attention with causal masking [12]:

$$\text{Attention}\left(Q, K, V\right) =$$

$$= \text{softmax}\left(\frac{QK^T}{\sqrt{d_k}} \otimes M\right)V,$$

where Q, K, V are linear projections of input embeddings, and $M \in \{0,1\}^{n \times n}$ is a lower triangular mask also known as casual mask preventing future information leakage.

BERT4Rec model extended this approach through bidirectional attention with masked language modelling training [13]:

$$L_{MLM} = -\sum_{i \in M} \log P\left(s_i^* \mid s_i\right),$$

where M denotes masked positions and s_i represents the sequence with position i masked.

Recent developments address attention mechanism limitations through computational efficiency improvements and temporal awareness enhancements.

LightSANs reduces computational requirements through simplified attention mechanisms, while TiSASRec incorporates temporal information through time-aware positional encodings:

$$\text{Attention}_{\text{time}}\left(Q, K, V, T\right) =$$

$$= \text{softmax}\left(\frac{Q\left(K + T_K\right)^T}{\sqrt{d_k}}\right)\left(V + T_V\right),$$

where T_V, T_K encode temporal intervals between interactions.

Graph neural network models

Graph neural networks (GNNs) provide a natural framework for modelling structural relationships within user sessions and between items in recommendation scenarios.

SR-GNN [14] represents sessions as directed graphs where nodes correspond to items and edges capture transition relationships. The gated graph neural network updates node representations through iterative message passing:

$$a_v^{(t)} = A_v \left[h_1^{(t-1)}, \ldots, h_n^{(t-1)} \right]^T W + b;$$

$$z_v^{(t)} = \sigma\left(W_z a_v^{(t)} + U_z h_v^{(t-1)}\right);$$

$$h_v^{(t)} = \left(1 - z_v^{(t)}\right) \otimes h_v^{(t-1)} + z_v^{(t)} \otimes \tilde{h}_v^{(t)},$$

where A is the adjacency matrix encoding session graph structure.

Knowledge graph integration enhances recommendation through external structured information incorporation.

KGAT model employs attention-based information propagation over collaborative knowledge graphs [15]:

$$e_u^{(l+1)} = \text{LeakyReLU} \times$$

$$\times \left(W^{(l)} \sum_{(h,r,t) \in N_u} \pi\left(h, r, t\right) m_{h,r,t}^{(l)} \right),$$

where $\pi(h, r, t)$ represents attention weights for relation-specific message aggregation.

State-space and continuous-time models

Neural ordinary differential equations (Neural ODEs) formulate hidden state evolution as a continuous-time dynamical system rather than a discrete layer-wise transformation [16]:

$$\frac{dh(t)}{dt} = f_\theta\left(h(t), t\right);$$

$$h(t_1) = h(t_0) + \int_{t_0}^{t_1} f_\theta\left(h(t), t\right) dt,$$

where f_θ is a neural network parameterisation. Solutions are computed with numerical ODE solvers; gradients are obtained via the adjoint method. Core advantages for recommendation systems based on Neural ODEs include natural handling of irregular time intervals between interactions, continuous preference evolution, principled temporal modelling, and interpretability through explicit dynamics.

Among the applications of Neural ODEs for recommendation systems, ReCODE model stands out and proves to be an efficient framework for studying users' consumption dynamics [17]. ReCODE is a model-agnostic framework that decomposes recommendation into:

$$\text{Score}(u, i, t) = \alpha \times$$

$$\times \text{Static}\ (u, i) + (1 - \alpha) \cdot \text{Dynamic}\ (u, i, t),$$

where the dynamic component is a Neural ODE capturing repeat-intent over time.

The initial state $h(t_0)$ is encoded from user-item interaction history; the ODE

$$\frac{dh(t)}{dt} = f_\theta\left(h(t), t, c\right)$$

evolves the latent state given context c; a decoder yields the repeat probability $p(u, i, t)$. ReCODE model integrates with matrix factorisation, neural collaborative filtering, GRU4Rec and SASRec models as the static branch.

Recent work applies Neural ODEs to recommendation by modelling repeat consumption and time-aware intensities with continuous dynamics.

A decision support tool in a problem of making session-based and sequential recommendations

The Analytic Hierarchy Process (AHP) is a decision-making method based on a system approach of structuring a complex problem in the form of a hierarchy creating pairwise comparison matrices of decision criteria, checking and increasing the consistency of judgments. AHP includes calculation of local priorities (weights), aggregation of priorities, and sensitive analysis of results. AHP combines mathematical and psychological principles for multi-criteria decision-making involving both quantitative and qualitative factors.

We propose to apply AHP for calculation of relative importance of benefits, costs, opportunities and risks (hereinafter decision criteria) in a problem of evaluation of scenarios for practical deployment of session-based and sequential recommendation systems.

Hierarchy of decision criteria is presented on Fig. 2. Let us consider the criteria in more detail. Recommendation system quality is assessed by using a special class of metrics – ranking quality metrics. Let $R_u@K$ denote the top-K recommendations for user/session u; G_u is the set or graded vector of relevant items.

1. Recall@K or HitRatio@K metric reflects the coverage of relevant items found in the first K positions (not rank-aware) and is defined as follows:

$$\text{Recall@}K = \frac{1}{|U|}\sum_u \frac{|R_u@K \cap G_u|}{|G_u|}.$$

The metric is good for measuring how many of the truly relevant items are retrieved when G_u is known.

2. Precision@K metric denotes how many of the top-K are relevant:

$$\text{Precision@}K = \frac{1}{|U|}\sum_u \frac{|R_u@K \cap G_u|}{\min\left(K, |G_u|\right)}.$$

3. MRR@K (mean reciprocal rank) metric emphasizes placing the first relevant item as high as possible and is defined as:

$$\text{MRR@}K = \frac{1}{|U|} \times$$

$$\times \sum_u \frac{1}{\min\left(r \le K \mid \text{item at rank } r \in G_u\right)}.$$

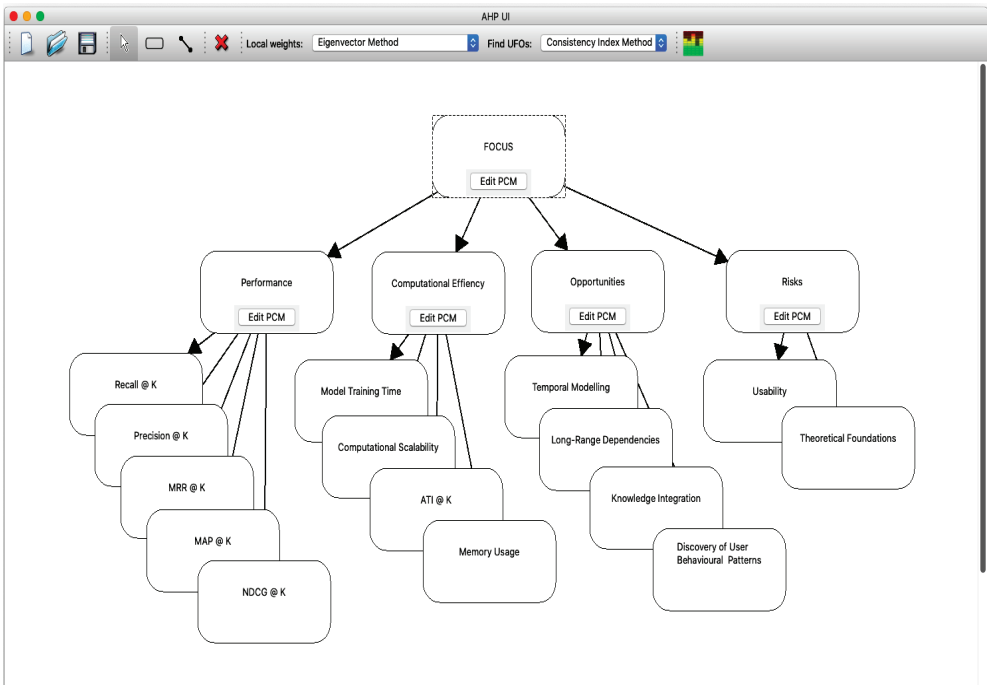

Fig. 2. Hierarchy of the criteria in a problem of evaluation of scenarios for practical deployment of session-based and sequential recommendation models

4. MAP@K (mean average precision) averages precision at every relevant hit, rewarding both finding many relevant items and ranking them early:

$$\mathrm{MAP@}K = \frac{1}{|U|}\sum_{u} \mathrm{AP@}K(u),$$

where

$$\mathrm{AP@}K = \frac{1}{\min\left(K, |G_u|\right)} \times$$

$$\times \sum_{r \le K} \mathrm{Precision@}r(u) \cdot 1\left(r \le K \mid \text{item at rank } r \in G_u\right).$$

5. NDCG@K (normalised discounted cumulative gain) is a rank-aware metric, it penalties putting elements lower or higher their true relevance score (rating):

$$\mathrm{NDCG@}K(u) = \frac{1}{|U|}\sum_{u} \frac{\mathrm{DCG@}K(u)}{\mathrm{IDCG@}K(u)},$$

where $\mathrm{DCG@}K(u) = \sum_{r \le K} \frac{g_{u,r}}{\log_2(r+1)}$; $g_{u,r}$ is graded relevance at rank r, and IDCG is the maximum achievable DCG for u.

Pairwise comparisons between decision criteria and sub-criteria are usually performed by an expert (Fig. 3) in a special fundamental scale. Priorities (weights) of decision criteria and sub-criteria are than calculated based on pairwise comparison matrices using the eigenvector method and other [19]. In a case of strong inconsistency of expert judgements, the most inconsistent elements of pairwise comparison matrices are found automatically [20] without participation of an expert (Fig. 4).

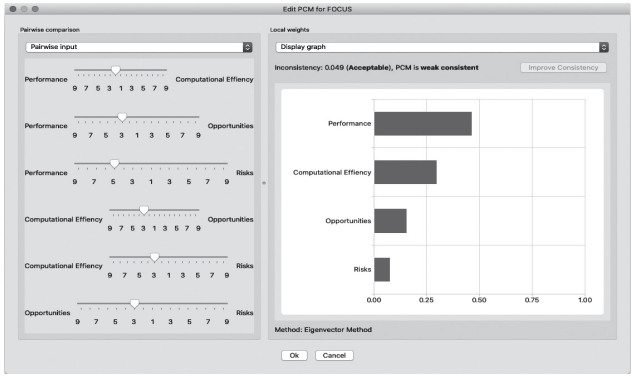

Fig. 3. Pairwise comparisons between criteria (left) and resulting local priorities (right)

Experimental evaluation and benchmarking analysis

Sequential recommendation systems, presented in this research, were evaluated on Million Musical Tweets Dataset (MMTD) – an established bench-

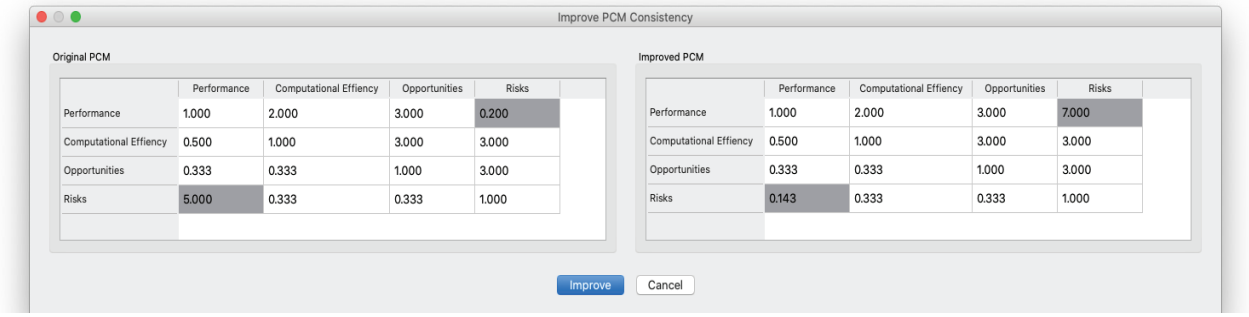

Fig. 4. The most inconsistent elements of a pairwise comparison matrix (left) and suggested automatic adjustment (right)

mark dataset. Million Musical Tweets Dataset [21] is a music listening history dataset with high-frequency interactions suitable for evaluating fine-grained temporal modelling approaches.

Results of evaluation of KGAT, GRU4Rec and SASRec models, as well as the proposed GRU4Rec&ReCODE and SASRec&ReCODE, equipped with ReCODE framework are displayed in Table 1 for $K = 50$.

The experimental results demonstrate that SASRec model achieves the strongest baseline performance, showing the effectiveness of self-attention mechanisms for sequential modelling, while Neural ODE-based ReCODE framework demonstrates consistent improvements when integrated with sequential baseline model. However, the impact of knowledge graph modelling on NDCG metric suggests the hypothesis that models equipped with this data structure learns to rank relevant models more efficiently.

The overall evidence supports the value of Neural ODE-based continuous-time modelling for sequential recommendation, with ReCODE providing meaningful enhancements to established baseline approaches while maintaining computational feasibility for practical deployment scenarios.

Table 1. Models' evaluation results on MMTD dataset

Model	Metric	
	Recall@K	NDCG@K
KGAT	0.1489	0.1006
GRU4Rec	0.1974	0.0841
SASRec	0.2274	0.1043
Proposed GRU4Rec&ReCODE	0.2307	0.0926
Proposed SASRec&ReCODE	0.2486	0.0994

Conclusions

A comprehensive system analysis of session-based and sequential recommendation systems has been provided, examining their evolution from foundational probabilistic approaches to modern neural architectures, with particular emphasis on emerging Neural ODE-based continuous-time modelling approaches. Our analysis reveals several fundamental achievements in sequential recommendation research. The field has progressed through distinct paradigmatic phases from Markov chain foundations establishing probabilistic frameworks, through neural recurrent approaches, which demonstrate deep learning effectiveness, to attention-based methods, which achieve state-of-the-art performance, and finally to emerging continuous-time formulations, which offer both theoretical rigor and computational efficiency.

The experimental evidence demonstrates that Neural Ordinary Differential Equations provide principled continuous-time modelling capabilities for sequential recommendation. The ReCODE framework achieves consistent performance improvements with respect to Recall@K metric across the considered base models GRU4Rec and SASRec, and validates the model-agnostic effectiveness of continuous-time approaches for capturing temporal dynamics in user behaviour.

The empirical analysis of benchmark datasets LastFM and Nowplaying-RS in terms of evaluation metrics reveals critical methodological considerations. The rich contextual features and temporal precision of datasets like Nowplaying-RS prove particularly valuable for evaluating sophisticated continuous-time models, while standardized evaluation protocols remain essential for reliable comparison across approaches.

Neural ODE-based approaches excel in scenarios with irregular temporal intervals and significant repeat consumption patterns, making them particularly suitable for music streaming, e-commerce, and content platforms where temporal dynamics significantly influence user preferences. While Neural ODEs introduce computational overhead through ODE solvers and adjoint gradient computation, the consistent performance gains and linear complexity advantages for long sequences justify their deployment in scenarios requiring sophisticated temporal modelling.

References

[1] F. Ricci *et al.*, "Introduction to recommender systems handbook," in *Recommender Systems Handbook*, New York, NY, USA: Springer, 2011, pp. 1–35. Retrieved from doi: 10.1007/978-0-387-85820-3_1

[2] J. Lu *et al.*, "Recommender system application developments: a survey," *Decision Support Systems*, Vol. 74, pp. 12–32, 2015. Retrieved from doi: 10.1016/j.dss.2015.03.008

[3] S. Zhang *et al.*, "Deep learning based recommender system: A survey and new perspectives," *ACM Computing Surveys*, Vol. 52, no. 1, pp. 1–38, 2019. Retrieved from doi: 10.1145/3285029

[4] Y. Koren, "Collaborative filtering with temporal dynamics," in *Proc. 15th ACM SIGKDD International Conference on Knowledge Discovery and Data Mining*, Paris, France, 2009. pp. 447–456. Retrieved from doi: 10.1145/1557019.1557072

[5] Y. Ding and X. Li, "Time weight collaborative filtering," in *Proc. 14th ACM International Conference on Information and Knowledge Management*, Bremen, Germany, 2005. pp. 485–492. Retrieved from doi: 10.1145/1099554.1099689

[6] S. Rendle *et al.*, "Factorizing personalized markov chains for next-basket recommendation," in *Proc. 19th International Conference on World Wide Web*, Raleigh, NC, USA, 2010. pp. 811–820. Retrieved from doi: 10.1145/1772690.1772773

[7] R. He and J. McAuley, "Fusing similarity models with markov chains for sparse sequential recommendation," in *Proc. IEEE 16th International Conference on Data Mining*, Barcelona, Spain, 2016. pp. 191–200. Retrieved from doi: 10.1109/ICDM.2016.0030

[8] S. Wang *et al.*, "Sequential/session-based recommendations: Challenges, approaches, applications and opportunities," in *Proc. 45th International ACM SIGIR Conference on Research and Development in Information Retrieval*, Madrid, Spain, 2022, pp. 3425–3428. Retrieved from doi: 10.1145/3477495.3532685

[9] S. Wang *et al.*, "A survey on session-based recommender systems," *ACM Computing Surveys*, Vol. 54, no. 7, pp. 1–38, 2022. Retrieved from doi: 10.1145/3465401

[10] A. Zimdars *et al.*, "Using temporal data for making recommendations," in *Proc. 17th Conference on Uncertainty in Artificial Intelligence*, Seattle, WA, USA, 2001, pp. 580–588.

[11] B. Hidasi *et al.*, "Session-based recommendations with recurrent neural networks," in *Proc. 4th International Conference on Learning Representations*, San Juan, Puerto Rico, 2016. Retrieved from arXiv: 1511.06939.

[12] W.C. Kang and J. McAuley, "Self-attentive sequential recommendation," in *Proc. IEEE International Conference on Data Mining*, Singapore, 2018, pp. 197–206. Retrieved from doi: 10.1109/ICDM.2018.00035

[13] F. Sun *et al.*, "BERT4Rec: Sequential recommendation with bidirectional encoder representations from transformer," in *Proc. 28th ACM International Conference on Information and Knowledge Management*, Beijing, China, 2019, pp. 1441–1450. Retrieved from doi: 10.1145/3357384.3357895

[14] S. Wu *et al.*, "Session-based recommendation with graph neural networks," in *Proc. AAAI Conference on Artificial Intelligence*, Honolulu, HI, USA, 2019, Vol. 33, pp. 346–353. Retrieved from doi: 10.1609/aaai.v33i01.3301346

[15] X. Wang *et al.*, "KGAT: Knowledge graph attention network for recommendation," in *Proc. 25th ACM SIGKDD International Conference on Knowledge Discovery and Data Mining*, Anchorage, AK, USA, 2019, pp. 950–958. Retrieved from doi: 10.1145/3292500.3330989

[16] R. T. Q. Chen *et al.*, "Neural ordinary differential equations," in *Advances in Neural Information Processing Systems 31*, Montrйal, Canada, 2018, pp. 6571–6583. Retrieved from arXiv: 1806.07366

[17] S. Dai *et al.*, "ReCODE: Modeling repeat consumption with neural ODE," in *Proc. 47th International ACM SIGIR Conference on Research and Development in Information Retrieval*, Washington, DC, USA, 2024, pp. 1742–1752. Retrieved from doi: 10.1145/3626772.3657936

[18] M. Ludewig and D. Jannach, "Are we really making much progress? A worrying analysis of recent neural recommendation approaches," in *Proc. 12th ACM Conference on Recommender Systems*, Vancouver, BC, Canada, 2018, pp. 101–109. Retrieved from doi: 10.1145/3298689.3347058

[19] N.I. Nedashkovskaya, "Method for weights calculation based on interval multiplicative pairwise comparison matrix in decision-making models," *Radio Electronics, Computer Science, Control*, no. 3, pp. 155–167, 2022. Retrieved from doi: 10.15588/1607-3274-2022-3-15

[20] N.I. Nedashkovskaya, "Investigation of methods for improving consistency of a pairwise comparison matrix," J*ournal of the Operational Research Society*, Vol. 69, no.12, pp. 1947–1956, 2018. Retrieved from doi: 10.1080/01605682.2017.1415640

[21] D. Hauger *et al.*, 2013. “The million musical tweet dataset: what we can learn from microblogs.” *International Society for Music Information Retrieval*, pp.189–194.

Д.В. Андросов, Н.І. Недашківська

СИСТЕМНИЙ ПІДХІД ДО БАГАТОКРИТЕРІАЛЬНОГО ОЦІНЮВАННЯ СЕАНСОВИХ І ПОСЛІДОВНИХ РЕКОМЕНДАЦІЙНИХ СИСТЕМ

Проблематика. Рекомендаційні системи стали незамінними компонентами сучасних цифрових платформ, забезпечуючи персоналізацію контенту в різних сферах. Традиційна колаборативна фільтрація та підходи на основі вмісту часто не в змозі охопити часову динаміку та контекстні залежності властиві моделям поведінки користувачів. Системи послідовних рекомендацій (sequential recommendation systems, SRSs) і системи рекомендацій на основі сеансів (session-based recommendation systems, SBRSs) з’явилися як нові парадигми для охоплення короткострокових динамічних уподобань користувачів для надання більш своєчасних і точних рекомендацій.

Мета дослідження. Запропонувати системний підхід до багатокритеріального оцінювання різних моделей SRS і SBRS – уніфіковану структуру для розуміння цих моделей, вибору найкращої моделі та спрямування майбутніх напрямів досліджень у системах рекомендацій з урахуванням часу. Виконати систематичний огляд і всебічний аналіз сеансових і послідовних систем рекомендацій, їх теоретичних основ, еволюції, емпіричних характеристик продуктивності й аспектів практичного розгортання.

Методика реалізації. Проаналізовано фундаментальні підходи від моделей ланцюгів Маркова до сучасних нейронних архітектур, включаючи методи на основі уваги, графові нейронні мережі і моделі простору станів. Систематично класифіковано підходи, ґрунтуючись на архітектурних принципах, стратегіях часового моделювання та методах інтеграції знань. Метод аналізу ієрархій застосовано для розрахунку відносної важливості доходів, витрат, можливостей і ризиків у задачі синтезу сеансових і послідовних систем рекомендацій. Проведено експериментальне дослідження різних моделей SRS і SBRS на контрольних наборах даних.

Результати дослідження. Емпіричні дослідження на еталонному для часового моделювання наборі даних показали, що поєднання SASRec та ReCODE покращило значення метрики Recall@K на 9 % порівняно з базовою моделлю SASRec, а поєднання GRU4Rec з ReCODE покращило цю метрику на 17 % порівняно з базовою GRU4Rec. Модель SASRec, яка адаптує архітектуру трансформера до задачі надання послідовних рекомендацій, досягла найвищої базової продуктивності за критеріями Recall@K і NDCG@K на еталонному наборі даних порівняно з іншими розглянутими моделями, демонструючи ефективність механізмів самоуваги для моделювання послідовностей. Незалежна від моделі структура ReCODE нейронних звичайних диференціальних рівнянь для рекомендаційних систем – ефективна основа для вивчення динаміки споживчого попиту, покращила метрики наявних базових підходів і має прийнятну обчислювальну складність для практичних сценаріїв розгортання рекомендаційних систем.

Висновки. Рекомендаційні системи на основі сеансів і послідовностей еволюціонували через зміну кількох парадигм із значними науковими досягненнями, включаючи становлення рекомендаційних моделей на основі сеансів відмінних від традиційної колаборативної фільтрації, розробку механізмів уваги для моделювання послідовностей і впровадження моделей неперервного часу. Майбутні напрями досліджень включають уніфіковані архітектури, рішення для масштабування, вдосконалені методології оцінювання та розширення для сценаріїв з багатьма зацікавленими сторонами.

Ключові слова: послідовна рекомендація; сеансова рекомендація; часове моделювання; механізми уваги; графові нейронні мережі; моделі простору станів; глибоке навчання; системний аналіз; прийняття рішень.

Рекомендована Радою
Навчально-наукового інституту
прикладного системного аналізу
КПІ ім. Ігоря Сікорського

Надійшла до редакції
21 жовтня 2025 року

Прийнята до публікації
15 грудня 2025 року

DOI: https://doi.org/10.20535/kpisn.2025.4.344357
UDC 004.032.26:004.93

M.P. Havrylovych
Igor Sikorsky Kyiv Polytechnic Institute, Kyiv, Ukraine
*Corresponding author: mariia.havrylovych@gmail.com

ARCHITECTURE OF HYBRID CNN-TRANSFORMER WITH MASKED TIME SERIES AUTO-CODING FOR BEHAVIOURAL BIOMETRICS ON MOBILE DEVICES

Background. Continuous behavioural authentication (keystroke dynamics, touch/swipe, motion sensors) verifies identity without extra actions. However, models degrade under device, session and activity shifts, are sensitive to noise and often require significant labelling. As passwordless logins spread, demand rises for post-login risk control and for models that are robust, compute-efficient and stable in real-world conditions.
Objective. The paper aims to develop and empirically study a compact CNN-Transformer hybrid with lightweight self-supervised masked time-series autoencoding (MAE-style) for mobile behavioural biometrics on the HMOG and WISDM datasets.
Methods. A 1D-CNN front end extracts local cues from smartphone motion signals, while a Transformer encoder captures longer-range dependencies. We use masked reconstruction on unlabelled HMOG sessions for self-supervised pretraining under a limited computational budget and then fine-tune the same hybrid architecture for user identification. We evaluate three hybrid variants on HMOG (trained from scratch, with masked pretraining, and with masked pretraining plus CORAL domain adaptation) and three models on WISDM (a Transformer baseline, a hybrid trained from scratch and a hybrid initialised from the HMOG-pretrained weights). Performance is measured using user-level mean and median Equal Error Rate (EER) and AUC at the individual user level.
Results. On HMOG, the hybrid model trained from scratch achieves the best user-level metrics (EER 21.51 % mean, 18.63 % median; AUC 0.854 mean, 0.905 median), while the lightweight MAE and CORAL variants do not yet surpass this baseline. On WISDM, the hybrid model substantially outperforms a pure Transformer baseline (EER 9.41 % vs 51.25 % mean; AUC 0.902 vs 0.488 mean), and cross-dataset initialisation from the HMOG MAE-pretrained weights provides an additional improvement (EER 8.42 % mean, 2.07 % median; AUC 0.907 mean, 0.959 median).
Conclusions. The results indicate that a compact CNN-Transformer hybrid is effective for sensor-based mobile behavioural biometrics and that even lightweight masked pretraining can be helpful for cross-dataset transfer. At the same time, the benefits of MAE and CORAL on HMOG depend strongly on the pretraining budget and masking configuration, suggesting that further tuning is needed to fully exploit self-supervised pretraining in this setting.
Keywords: behavioural biometrics; continuous authentication; smartphone sensors; CNN-Transformer hybrid; masked autoencoding; self-supervised pretraining; domain adaptation.

Introduction

The widespread use of smartphones and wearables has turned them into primary access points for services, including systems that explicitly explore behavioural biometrics on everyday activities [1] and continuous sensing on smartphones [2, 3], which in turn creates stricter requirements for the underlying information security mechanisms. Traditional one-shot authentication methods such as passwords, PIN codes and fingerprint scans verify the user only at login time. Once a device is unlocked, anyone who physically gains access to it can continue to work under the legitimate user's identity. This is particularly critical when smartphones are used to access financial services, corporate resources and personal communications, as demonstrated both in general-purpose smartphone biometrics [1, 2, 3] and in our earlier work on continuous authentication for security-critical services [4].

Continuous behavioural authentication offers an alternative paradigm: the user's identity is verified

Пропозиція для цитування цієї статті: М.П. Гаврилович, «Архітектура гібридного CNN-transformer з маскованим автокодуванням часових рядів для поведінкової біометрії на мобільних пристроях», *Наукові вісті КПІ*, № 4, с. 55–62, 2025. doi: https://doi.org/10.20535/kpisn.2025.4.344357

Offer a citation for this article: M.P. Havrylovych, "Architecture of hybrid CNN-transformer with masked time series auto-coding for behavioural biometrics on mobile devices", *KPI Science News*, No. 4, pp. 55–62, 2025. doi: https://doi.org/10.20535/kpisn.2025.4.344357

in the background throughout device usage, based on behavioural signals [1, 2, 3]. These signals include keystroke dynamics on the virtual keyboard, which have been extensively reviewed for both fixed-text and free-text scenarios [8, 9], deep keystroke models on desktop and mobile platforms [10, 11], as well as touch/swipe patterns and inertial sensor data such as accelerometer and gyroscope signals that underpin smartphone and smartwatch biometrics [1, 2, 3]. Together, they form a behavioural "fingerprint" that can be used to distinguish one user from others without requiring explicit re-authentication. This class of methods is closely related to behavioural biometrics and continuous authentication frameworks used for post-login risk control in high-stakes applications [1, 4].

However, building robust behavioural biometric models is challenging. Unlike static biometrics, behavioural patterns are highly context-dependent. They vary with posture (sitting, standing, walking), activity, device model and UI layout, and can also drift over time. Sensor data is noisy and often contains missing values. Changes in hardware, operating system version or user habits can cause domain shifts that degrade the performance of models trained on earlier data. Collecting large labelled datasets per user is expensive and often impractical, especially at scale, a limitation repeatedly highlighted in smartphone and sensor-based continuous authentication studies [1, 2, 3] and confirmed in our own experiments on motion-based verification and wearable sensing [4].

Recent advances in deep learning, particularly convolutional and recurrent architectures in continuous authentication [4, 6] and Transformer-based models for keystroke and time-series data [10, 11, 13, 14], have significantly improved the state of the art in signal and sequence modelling. CNNs are effective at capturing local patterns and invariances, while Transformers use self-attention to model long-range dependencies. In parallel, self-supervised learning methods such as masked autoencoders (MAE) have demonstrated that useful representations can be learned from large unlabelled datasets by reconstructing masked parts of the input [13, 14].

Despite these advances, many mobile behavioural biometric systems still rely on purely convolutional or recurrent architectures [1, 2, 11] or on traditional keystroke pipelines surveyed in [8, 9], are trained from scratch on relatively small labelled datasets and only partially address domain shifts between sessions and conditions. There is still a need for models that can exploit unlabelled behavioural data, maintain robustness under cross-session and cross-condition scenarios and remain efficient enough for deployment on mobile devices.

This work addresses these challenges by exploring a hybrid CNN-Transformer architecture with masked time-series autoencoding for mobile behavioural biometrics. The proposed model targets continuous authentication scenarios, where decisions about user identity must be made based on short sliding windows of behavioural data, similar to the window-based protocols used in HMOG, WISDM and related continuous authentication work [2, 3, 12]. The architecture is designed to leverage unlabelled sessions for lightweight self-supervised pretraining and to support efficient inference on mobile devices while remaining robust to domain shifts, building on ideas from prior deep continuous authentication systems [4, 6], Transformer-based keystroke and time-series models [10, 11, 14] and masked autoencoding for temporal data [13].

Problem Statement

Let $U = \{u\_1, ..., u\_K\}$ be a set of users. For each user u_k, we have a collection of interaction sessions recorded from a smartphone. Each session consists of one or more time-series channels derived from sensors (e.g., accelerometer, gyroscope) and/or interaction events (such as touch coordinates). A session can be represented as a sequence $x^(i) = = \{x\_t^(i)\}\_t$, where $x\_t^(i) \in R^C$, is the feature vector at time t and C is the number of channels.

For continuous authentication, the data stream is segmented into overlapping windows of fixed length T, producing fragments $X\_j \in R^(T \times C)$, each labelled with the corresponding user ID y_j in $\{1, ..., K\}$. The primary task considered in this work is user identification: given a window X, predict the user label y. Formally, we seek a model f_θ: $R^(T \times C)$ to $\{1, ..., K\}$ that maps each window to a distribution over user classes and minimises identification and verification errors under realistic cross-session and cross-condition settings.

In this work, we focus on Equal Error Rate (EER) and the area under the ROC curve (AUC), computed at the user level, as the primary evaluation metrics for continuous authentication. For each user, we compute individual EER and AUC values and then aggregate them across users by taking the mean and median. Beyond these verification metrics, the model should also satisfy practical constraints such as robustness to domain shifts and efficient inference on resource-constrained mobile hardware, and remain compatible with model compression and quantisation in future deployments.

Presentation of the Main Research Results

1. Related Work

Research on behavioural biometrics for mobile devices can be broadly divided into three directions: keystroke dynamics on virtual keyboards, sensor-based activity and movement analysis, and multimodal fusion of interaction and sensor signals [1, 2, 3].

Keystroke-based authentication methods analyse timing information associated with keypress events: inter-keystroke intervals, key hold times and editing patterns. Early works focused on fixed-text scenarios, whereas more recent approaches consider free-text typing where the user enters arbitrary content [8, 9]. It has been shown that even in free-text conditions, typing patterns remain sufficiently stable to support user identification and verification when combined with appropriate sequence models, including modern deep learning architectures [9, 10, 11].

In sensor-based continuous authentication, datasets such as HMOG and WISDM have become standard benchmarks. HMOG provides inertial sensor readings, device orientation and touch events from smartphones in sitting and walking scenarios, enabling evaluation under motion-induced variability and fine-grained hand movement patterns [2]. WISDM includes accelerometer and gyroscope time series from smartphones and smartwatches collected during daily activities and has been used both for activity recognition [1] and for biometric identification when users are treated as classes, including in our earlier work on motion-based verification [4]. Deep learning models for these datasets range from convolutional and recurrent networks to architectures specifically designed for continuous smartphone authentication [1, 3], with our previous studies exploring autoencoder-based and hybrid transformer architectures for user verification on motion and wearable signals [4, 6].

Transformer-based models have recently been proposed in mobile behavioural biometrics to operate directly on sequences of interaction and sensor events [10, 11, 14]. On large-scale typing datasets, Transformer architectures have been shown to outperform classical recurrent networks by effectively modelling long sequences of interactions and their contextual dependencies; TypeFormer is one example of a mobile keystroke Transformer achieving state-of-the-art results [10]. Hybrid CNN-Transformer architectures and attention-based sequence models more generally have also been explored in time-series processing, where convolutional layers serve as a front end for local pattern extraction and sequence length reduction, while Transformer encoders model global dependencies [11, 14].

Self-supervised methods, in particular masked autoencoders, allow learning robust representations from unlabelled data by reconstructing masked parts of the input. For time series, TS-MAE demonstrates that masked reconstruction can significantly improve representation quality under limited labels and domain shifts [13], while broader surveys of Transformers in time series highlight both the strengths and open issues of such models for temporal data [14]. Domain adaptation techniques such as Deep CORAL achieve additional robustness by aligning feature distributions across domains [15]. In our previous work we have investigated autoencoder-based and recurrent models for biometric verification using motion and sensor signals, as well as hybrid Transformer-autoencoder architectures for continuous authentication on wearable devices, demonstrating competitive Equal Error Rates and flexibility across signal types [5, 6, 7]. The present work extends these ideas to a CNN-Transformer hybrid with self-supervised pretraining and domain adaptation tailored to mobile behavioural biometrics.

2. Proposed CNN-Transformer Architecture with Masked Autoencoding

2.1. Input Preprocessing

Raw time-series data from sensors and, where available, interaction logs are first normalised per channel by subtracting the mean and dividing by the standard deviation computed on the training set. Each session is then segmented into overlapping windows of fixed length T with a chosen stride. Windows with insufficient valid samples are discarded. Each window $X \in R\hat{}(C \times T)$ is treated as a multi-channel time-series fragment. For implementation convenience, tensors can be rearranged to shape (C, T) for compatibility with one-dimensional convolutions. In the experiments reported in this paper, we focus on inertial sensor channels from HMOG and WISDM.

2.2. Convolutional Front End

The convolutional front end is a stack of 1D convolutional layers applied along the temporal dimension. Each layer consists of a convolution with a small kernel, batch normalisation and a non-linear activation such as GELU. Channel dimensionality is gradually increased across layers, allowing the network to capture increasingly complex local patterns while suppressing noise. A multi-scale design can be achieved by combining kernels of different sizes or using dilated convolutions. The result is a sequence of feature vectors of shape $T \times C\_out$ that summarise local behavioural patterns such as

micro-movements and short-term dynamics in the motion signals.

2.3. Transformer Encoder

The CNN features are linearly projected into a d-dimensional space to form a sequence of embeddings. Positional encodings, such as sinusoidal or relative positional encodings, are added to represent temporal order. The resulting sequence is processed by a stack of Transformer encoder layers, each comprising multi-head self-attention and position-wise feed-forward networks with residual connections and layer normalisation. Self-attention allows the model to focus on the most informative events within the window and to capture long-range dependencies and interactions between channels. This is particularly important for behavioural biometrics, where discriminative patterns may be scattered across the window rather than localised.

2.4. Masked Time-Series Autoencoding

To exploit unlabelled sessions, a masked time-series autoencoding task is used for self-supervised pretraining. For each window, a binary mask over time steps is sampled, masking a fixed fraction of positions. The corresponding inputs are zeroed out, and the masked sequence is fed through the CNN front end and Transformer encoder. A reconstruction head maps the hidden representations back to the CNN feature space, and the mean squared error is computed between the reconstructed and original CNN features, but only on masked time steps.

This masked reconstruction objective encourages the model to infer missing local patterns from temporal context and to build representations that are robust to noise and missing data. Because no user labels are required, large volumes of unlabelled behavioural data can be used for pretraining. In practice, a lightweight pretraining regime is adopted: a compact model with modest dimensionality and a short window length is trained for a limited number of epochs and gradient steps, which is sufficient to provide a useful initialisation for subsequent supervised training.

2.5. Classification and Loss Functions

After the Transformer encoder, the sequence of hidden vectors is aggregated into a fixed-dimensional representation via global average pooling over time. The pooled vector is passed through a small multi-layer classification head consisting of layer normalisation, a hidden linear layer with non-linearity and an output linear layer mapping to K user classes.

In this work, the supervised loss is the standard cross-entropy loss. The architecture is compatible with angular-margin softmax losses and additional metric-learning losses such as triplet loss or center loss, as well as with domain adaptation regularizers such as CORAL, which we explicitly use in one of the HMOG variants. A more extensive exploration of alternative loss functions is left for future work.

3. Experimental Setup

3.1. Datasets

We consider two public datasets that are widely used in mobile behavioural biometrics and activity recognition.

The **HMOG** dataset provides multimodal recordings for continuous authentication, including accelerometer, gyroscope, magnetometer, device orientation and touch events from smartphones [2]. Users perform text-entry and other tasks in sitting and walking conditions, which enables evaluation under motion-induced variability. From HMOG we derive multimodal windows that may include multiple inertial sensor channels.

The **WISDM Smartphone and Smartwatch Activity and Biometrics** dataset contains accelerometer and gyroscope time series collected from multiple subjects during daily activities [1, 12]. While it is often used for activity recognition, we treat users as classes and extract fixed-length windows of motion data for biometric identification.

For both datasets, raw recordings are converted into fixed-length windows X in $R\hat{}(T\times C)$ with user labels. We keep the same windowing strategy across baselines and our model.

3.2. Evaluation Protocols

We use cross-session protocols in which training and testing data for each user come from different recording sessions. Where the dataset structure allows it, we additionally simulate cross-condition or cross-device scenarios by training and testing on disjoint subsets corresponding to different recording conditions or device types (for example, sitting versus walking conditions in HMOG).

Performance is reported in terms of user-level mean and median Equal Error Rate (EER) and the area under the ROC curve (AUC). For each user, we compute individual EER and AUC values and then aggregate them across users by taking the mean and median.

3.3. Model Variants and Baselines

To quantify the benefits of the proposed CNN-Transformer architecture, masked pretraining and domain adaptation, we evaluate a family of models on both datasets. Each model variant corresponds to a specific configuration in the codebase and is identified by a short experiment name.

On the **HMOG** dataset, we consider three variants:

– **HMOG_HYBRID_NO_MAE** – the proposed CNN-Transformer hybrid architecture trained from scratch in a purely supervised way, without masked pretraining or domain adaptation. This variant isolates the architectural contribution of the hybrid model.

– **HMOG_HYBRID_MAE_LIGHT** – the same hybrid architecture, but initialised using a lightweight masked autoencoding pretraining stage on HMOG. This experiment tests whether even modest self-supervised pretraining improves downstream identification and verification metrics.

– **HMOG_HYBRID_MAE_LIGHT_CORAL** – the hybrid model with lightweight MAE pretraining and an additional CORAL-based domain adaptation term that aligns feature distributions between two HMOG conditions (e.g., sitting vs walking) during supervised training. This variant is used to evaluate the impact of explicit domain adaptation on cross-condition performance.

On the **WISDM** dataset, we evaluate three analogous variants:

– **WISDM_TRANSFORMER** – a pure Transformer baseline trained on WISDM windows with no CNN front end.

– **WISDM_HYBRID_NO_MAE** – the CNN-Transformer hybrid architecture trained from scratch on WISDM without masked pretraining.

– **WISDM_HYBRID_FROM_HMOG_MAE** – the hybrid model initialised from the HMOG lightweight MAE-pretrained checkpoint and subsequently fine-tuned on WISDM. In this setting, no separate MAE pretraining is performed on WISDM; instead, HMOG serves as a source domain for cross-dataset pretraining.

Together, these experiments allow us to disentangle the effects of architecture (Transformer-only vs hybrid), masked pretraining (with vs without MAE) and domain adaptation (with vs without CORAL on HMOG), as well as to study the usefulness of cross-dataset pretraining when transferring from HMOG to WISDM.

3.4. Training Procedure and Ablation Studies

All models are trained using the same windowing strategy and train/validation splits within each dataset. The hybrid architecture is evaluated under different training regimes that correspond directly to the experiment list described above.

For hybrid models with masked pretraining, we adopt a lightweight MAE regime. In the HMOG_HYBRID_MAE_LIGHT and HMOG_HYBRID_MAE_LIGHT_CORAL experiments, a compact hybrid model (with a moderate embedding dimension and a short window length) is pretrained on the HMOG training split using a masked reconstruction objective. A fixed fraction of time steps is randomly masked in each window, and the model is trained to reconstruct convolutional features at the masked positions. The number of pretraining epochs and gradient steps per epoch is deliberately limited to keep computational cost modest while still providing a beneficial initialisation for supervised training.

In the subsequent fine-tuning stage, all models are optimised for user identification using cross-entropy. For the HMOG_HYBRID_MAE_LIGHT_CORAL variant, a CORAL term is included to align feature covariances between HMOG conditions (for example, sitting versus walking sessions), thereby mitigating domain shift.

On WISDM, the MAE pretraining is not repeated. Instead, the WISDM_HYBRID_FROM_HMOG_MAE experiment reuses the HMOG MAE-pretrained checkpoint as an initialisation and fine-tunes the hybrid model on WISDM in a supervised manner. This cross-dataset transfer setting allows us to test whether representations learned from HMOG generalise to a different sensor dataset without additional self-supervised pretraining.

The remaining variants, HMOG_HYBRID_NO_MAE and WISDM_HYBRID_NO_MAE, are trained from randomly initialised weights without any masked pretraining or domain adaptation and serve as ablations that isolate the architectural effect of the hybrid model. The WISDM_TRANSFORMER baseline enables a direct comparison between a purely attention-based model and the hybrid design.

For each experiment, we report user-level mean and median Equal Error Rate (EER) and AUC, computed by first evaluating EER and AUC per user and then aggregating across users.

4. Results

Tables 1 and 2 summarise the user-level verification performance of all model variants on the HMOG and WISDM datasets, respectively. For each model, we report the mean and median Equal Error Rate (EER) and the mean and median AUC across users.

On HMOG (Table 1), the hybrid model trained from scratch (H-HYB) achieves a mean EER of 21.51 % and a median EER of 18.63 %, with a mean AUC of 0.854 and a median AUC of 0.905. Lightweight masked pretraining (H-HYB-MAE) leads to substantially lower global EER before averaging, but when evaluated in terms of user-level mean and median EER it results in a higher EER (29.40 % mean, 27.41 % median) and a lower AUC (0.762 mean, 0.800 median) than H-HYB. The CORAL-enhanced hybrid (H-HYB-MAE-CORAL) improves

***Table* 1.** Verification performance of hybrid models on the HMOG dataset (user-level mean and median EER and AUC)

Model	EER mean, %	EER median, %	AUC mean	AUC median
H-HYB	21.51	18.63	0.854	0.905
H-HYB-MAE	29.40	27.41	0.762	0.800
H-HYB-MAE-CORAL	23.37	20.61	0.832	0.892

***Table* 2.** Verification performance of hybrid and Transformer models on the WISDM dataset (user-level mean and median EER and AUC)

Model	EER mean, %	EER median, %	AUC mean	AUC median
H-HYB	21.51	18.63	0.854	0.905
H-HYB-MAE	29.40	27.41	0.762	0.800
H-HYB-MAE-CORAL	23.37	20.61	0.832	0.892

over H-HYB-MAE, reducing the mean and median EER to 23.37 % and 20.61 %, respectively, and increasing the mean and median AUC to 0.832 and 0.892. Nevertheless, in this lightweight training regime, the best user-level EER and AUC on HMOG are still obtained by the hybrid model trained from scratch without MAE, suggesting that the current pretraining budget and masking configuration are not yet optimal for this dataset.

On WISDM (Table 2), the situation is markedly different. The pure Transformer baseline (W-TRF) exhibits very poor user-level EER (51.25 % mean, 48.62 % median) and low AUC (0.488 mean, 0.513 median), indicating that it fails to provide a good operating point for verification on a per-user basis. In contrast, the hybrid models significantly improve user-level performance. The hybrid trained from scratch on WISDM (W-HYB) achieves a mean EER of 9.41 % and a median EER of 2.40 %, with a mean AUC of 0.902 and a median AUC of 0.956. Initialising the hybrid from the HMOG MAE-pretrained checkpoint (W-HYB-HMOG-MAE) further reduces the mean and median EER to 8.42 % and 2.07 %, respectively, and slightly increases the mean and median AUC to 0.907 and 0.959. These results indicate that, even under a lightweight pretraining regime, cross-dataset initialisation from HMOG is beneficial for WISDM.

Overall, the experiments show that the CNN-Transformer hybrid clearly outperforms the pure Transformer baseline on WISDM in terms of user-level EER and AUC, and that cross-dataset masked pretraining provides a small but consistent improvement there. On HMOG, however, the same lightweight MAE configuration does not yet improve user-level metrics over training from scratch, although CORAL-based domain adaptation partially recovers performance relative to the MAE-only variant. This suggests that the effectiveness of masked pretraining in mobile behavioural biometrics is sensitive to the choice of dataset, pretraining budget and masking strategy, and highlights the need for further tuning and ablation studies.

5. Discussion

The proposed CNN-Transformer hybrid with masked time-series autoencoding combines several complementary ideas. The convolutional front end acts as a robust local feature extractor that smooths noise and emphasises characteristic micro-movements and interaction patterns. The Transformer encoder provides a flexible mechanism for modelling long-range dependencies and interactions between modalities within the window. Masked autoencoding enables effective use of large pools of unlabelled behavioural data and encourages representations that are robust to missing values and domain shifts. The structured set of experiments on HMOG and WISDM, covering a Transformer baseline on WISDM and hybrid models trained from scratch, with lightweight MAE pretraining and with CORAL-enhanced training, provides a basis for attributing gains to specific architectural and training choices rather than to a single monolithic model.

At the same time, the architecture has limitations. Its performance can be sensitive to design choices such as window length, mask ratio, number of Transformer layers and attention heads. The Transformer component is more computationally demanding than purely convolutional or recurrent alternatives, which constrains model depth on mobile devices. Domain adaptation techniques such as CORAL mitigate some cross-condition shifts but may not fully address all forms of domain mismatch, especially when device hardware or user populations differ substantially.

Despite these challenges, the CNN-Transformer MAE hybrid represents a promising direction for robust mobile behavioural biometrics and continuous authentication. It allows combining heterogeneous behavioural signals within a unified model and naturally exploits unlabelled data that arise in real-world deployments.

Conclusions

This paper has presented a CNN-Transformer hybrid architecture with masked time-series autoencoding for mobile behavioural biometrics and continuous authentication. The model combines a convolutional front end for local pattern extraction, a Transformer encoder for global sequence modelling and a masked reconstruction task for self-supervised pretraining on unlabelled sessions under a lightweight training budget.

The approach is motivated by the practical challenges of behavioural biometric modelling on smartphones: noisy and context-dependent data, domain shifts over time and limited labelled data per user. By leveraging self-supervised pretraining, domain adaptation and flexible sequence modelling, the proposed architecture aims to improve robustness and accuracy under realistic conditions while remaining compatible with mobile deployment. The comparison with a Transformer-only baseline on WISDM, as well as ablation studies on masked pretraining and domain adaptation on HMOG, are intended to clarify the contribution of each architectural component.

Future work includes comprehensive experiments on additional public datasets, more detailed ablation studies of architectural and training choices and investigation of on-device optimisation techniques such as quantisation and pruning, as well as more advanced domain adaptation methods for cross-device and cross-population scenarios.

References

[1] G.M. Weiss *et. al.*, "Smartphone and smartwatch-based biometrics using activities of daily living," *IEEE Access*, Vol. 7, pp. 133190–133202, 2019. Retrieved from doi: https:///doi.org/10.1109/ACCESS.2019.2940729

[2] Z. Sitová *et. al.*, "HMOG: New behavioral biometric features for continuous authentication of smartphone users," *IEEE Transactions on Information Forensics and Security*, Vol. 11, no. 5, pp. 877–892, 2016. Retrieved from doi: https:///doi.org/10.1109/TIFS.2015.2506542

[3] M. Abuhamad *et. al.*, "AUToSen: Deep-learning-based implicit continuous authentication using smartphone sensors," *IEEE Internet of Things Journal*, Vol. 7, no. 6, pp. 5008–5020, 2020. Retrieved from doi: https:///doi.org/10.1109/JIOT.2020.2975779

[4] M. Havrylovych and V. Danylov, "Deep learning application in continuous authentication," in *Digital Ecosystems: Interconnecting Advanced Networks with AI Applications*, A. Luntovskyy, Ed. Cham: Springer, 2024, pp. 644–667, Lecture Notes in Electrical Engineering, Vol. 1198. Retrieved from doi: https:///doi.org/10.1007/978-3-031-61221-3_31

[5] M.P. Havrylovych and V.Y. Danylov, "Research of autoencoder-based user biometric verification with motion patterns," *System Research and Information Technologies*, no. 2, pp. 128–136, 2022. Retrieved from doi: https:///doi.org/10.20535/SRIT.2308-8893.2022.2.10

[6] M.P. Havrylovych and V.Y. Danylov, "Research on hybrid transformer-based autoencoders for user biometric verification," *System Research and Information Technologies*, no. 3, pp. 42–53, 2023. Retrieved from doi: https:///doi.org/10.20535/SRIT.2308-8893.2023.3.03

[7] M. Havrylovych *et. al.*, "Comparative analysis of using recurrent autoencoders for user biometric verification with wearable accelerometer," in *Proceedings of the 9th International Conference "Information Control Systems & Technologies"* (ICST 2020), CEUR-WS, Vol. 2711, pp. 358–370, 2020.

[8] A. Alsultan and K. Warwick, "Keystroke dynamics authentication: A survey of free-text methods," *International Journal of Computer Science Issues*, Vol. 10, no. 4, pp. 1–10, 2013.

[9] R.S. Ahmed *et. al.*, "Keystroke dynamics: Concepts, techniques, and applications," *ACM Computing Surveys*, Vol. 57, no. 11, pp. 283:1–283:35, 2025. Retrieved from doi: https:///doi.org/10.1145/3675583

[10] G. Stragapede *et. al.*, "TypeFormer: Transformers for mobile keystroke biometrics," *Neural Computing and Applications*, 2024, early access, doi: https:///doi.org/10.1007/s00521-024-10140-2

[11] J. Kim *et. al.*, "Keystroke dynamics-based user authentication using freely typed text based on user-adaptive feature extraction and novelty detection," *Applied Soft Computing*, Vol. 62, pp. 1077–1087, 2018. Retrieved from doi: https:///doi.org/10.1016/j.asoc.2017.09.045

[12] G.M. Weiss, "WISDM smartphone and smartwatch activity and biometrics dataset," WISDM Lab, Fordham University, technical report, 2019. [Online]. Available: https://archive.ics.uci.edu/

[13] Q. Liu *et. al.*, “TS-MAE: A masked autoencoder for time series representation learning,” *Information Sciences*, Vol. 690, art. 121576, 2025. Retrieved from doi: https:///doi.org/10.1016/j.ins.2024.121576

[14] Q. Wen *et. al.*, “Transformers in time series: A survey,” in *Proceedings of the 32nd International Joint Conference on Artificial Intelligence* (IJCAI 2023), pp. 6778−6786, 2023. Retrieved from doi: https:///doi.org/10.24963/ijcai.2023/759

[15] B. Sun and K. Saenko, “Deep CORAL: Correlation alignment for deep domain adaptation,” in *Computer Vision − ECCV 2016 Workshops*, pp. 443−450, 2016. Retrieved from doi: https:///doi.org/10.1007/978-3-319-49409-8_35

М.П. Гаврилович

АРХІТЕКТУРА ГІБРИДНОГО CNN-TRANSFORMER З МАСКОВАНИМ АВТОКОДУВАННЯМ ЧАСОВИХ РЯДІВ ДЛЯ ПОВЕДІНКОВОЇ БІОМЕТРІЇ НА МОБІЛЬНИХ ПРИСТРОЯХ

Проблематика. Безперервна поведінкова автентифікація (динаміка натискань клавіш, жести торкання/свайпи, датчики руху) дає змогу перевіряти особу користувача без додаткових дій з його боку. Водночас моделі деградують у разі зміни пристрою, сесії чи виду активності, є чутливими до шуму та часто потребують значних обсягів розмічених даних. З поширенням безпарольних методів входу зростає потреба в механізмах постлогін-контролю ризиків та у моделях, які є стійкими, обчислювально ефективними й стабільними в реальних умовах експлуатації.

Мета дослідження. Розробити та емпірично дослідити компактний гібрид CNN-Transformer із легковаговим самонавчальним маскованим автокодуванням часових рядів (MAE-підхід) для мобільної поведінкової біометрії на наборах даних HMOG та WISDM.

Методика реалізації. Попередній 1D-CNN-блок виділяє локальні ознаки із сигналів руху смартфона, тоді як енкодер Transformer моделює довгострокові залежності. Для самонавчального претрейнінгу за обмеженого обчислювального бюджету використовують масковану реконструкцію на немаркованих сесіях HMOG, після чого та сама гібридна архітектура продовжує навчатися в режимі класифікації користувачів. Оцінено три гібридні варіанти на HMOG (навчання з нуля, навчання з маскованим претрейнінгом, а також з маскованим претрейнінгом і адаптацією CORAL) і три моделі на WISDM (базовий Transformer, гібрид без претрейнінгу та гібрид, ініціалізований вагами після MAE-претрейнінгу на HMOG). Якість вимірюють за середніми та медіанними значеннями Equal Error Rate (EER) та AUC на рівні окремих користувачів.

Результати дослідження. На наборі HMOG найкращих користувацьких показників досягає гібридна модель, навчена з нуля (EER: 21,51 % у середньому та 18,63 % за медіаною; AUC: 0,854 у середньому та 0,905 за медіаною), тоді як легковагові варіанти з MAE та CORAL поки що не перевершують цю базову конфігурацію. На WISDM гібридна модель суттєво переважає чистий Transformer-базлайн (EER: 9,41 % проти 51,25 % у середньому; AUC: 0,902 проти 0,488 у середньому), а ініціалізація вагами після MAE-претрейнінгу на HMOG дає додаткове покращення (EER: 8,42 % у середньому та 2,07 % за медіаною; AUC: 0,907 у середньому та 0,959 за медіаною).

Висновки. Отримані результати свідчать, що компактний гібрид CNN-Transformer є ефективним для сенсорної мобільної поведінкової біометрії та що навіть легковаговий маскований претрейнінг може бути корисним для перенесення між наборами даних. Водночас користь MAE та CORAL на HMOG істотно залежить від бюджету претрейнінгу та конфігурації маскування, що вказує на необхідність подальшого налаштування, аби повністю використати потенціал самонавчального претрейнінгу в цій постановці.

Ключові слова: поведінкова біометрія; безперервна автентифікація; давачі смартфона; гібрид CNN-Transformer; масковане автокодування; самонавчальний претрейнінг; адаптація домену.

Рекомендована Радою
Навчально-наукового інституту прикладного системного аналізу
КПІ ім. Ігоря Сікорського

Надійшла до редакції
17 серпня 2025 року

Прийнята до публікації
15 грудня 2025 року

АВТОРИ НОМЕРА

Андросов Дмитро Васильович
ORCID: 0009-0001-1330-1473

Гаврилович Марія Павлівна
ORCID: 0000-0002-9797-2863

Городецький Дмитро Сергійович
ORCID: 0009-0009-7535-9724

Данилов Валерій Якович
ORCID: 0000-0003-3389-3661

Зарицький Олексій Олексійович
ORCID: 0009-0003-1243-5845

Недашківська Надія Іванівна
ORCID: 0000-0002-8277-3095

Нікітін Владислав Олегович
ORCID: 0009-0001-9921-0213

Романюк Вадим Васильович
ORCID: 0000-0003-3543-3087

Сметюх Михайло Петрович
ORCID: 0000-0002-3817-6162

Соловйов Сергій Олександрович
ORCID: 0000-0003-2681-7417